UNIVERSITY OF CALIFORNIA

Santa Barbara

Subject-Oriented Finite Fault Inversions and their Applications

A dissertation submitted in partial satisfaction of the

requirements for the degree Doctor of Philosophy

in Geological Sciences

by

Mareike N. Adams

Committee in charge:

Professor Chen Ji, Co-Chair

Professor Ralph Archuleta, Co-Chair

Professor Toshiro Tanimoto

December 2018

The dissertation of Mareike N. Adams is approved.

_____

Toshiro Tanimoto

_____

Ralph Archuleta, Committee Co-Chair

_____

Chen Ji, Committee Co-Chair

December 2018

Subject-Oriented Finite Fault Inversions and their Applications

by

Mareike N. Adams

ACKNOWLEDGEMENTS

First, none of this would be possible without the support of my advisors Professors Ralph Archuleta and Chen Ji, and my other committee member Professor Toshiro Tanimoto. They pushed the boundaries of my knowledge farther than I ever thought possible. Their patience has enabled me to muddle through countless problems and allowed me to grow as a scientist.

Graduate school is a tumultuous time. Luckily, we have navigation systems such as our friends and family. I could never have completed my degree without the incredible encouragement of many wonderful people in my life. Every busy day was made a little sweeter by the laughter of my friends sitting next to me in the office, or just down the hall, or sending me warmth from across the country. Near or far, whenever that ugly monster named depression reared its ugly head, I could always count on them for much needed support, kindness, humor, energy, and love. In particular, I want to thank the incomparable Annie who sat next to me in our dusty office for 5 long years. She celebrated all the best moments with me and kept me company for all the worst. I could never have done this without her.

Five years ago I decided to move to California from Québec. This, somewhat crazy, idea ended up changing my life in many ways. The one constant through all of it was my beloved family. Despite being so far away they always made time to come visit my new home, call me when I was excited or feeling down…

In short, this great event in my life belongs to many people. And I could not be more thankful.

VITA OF MAREIKE N. ADAMS - December 2018

EDUCATION

Doctor of Philosophy in Geological Sciences (expected) — December 2018
University of California, Santa Barbara
Advisor: Professors Chen Ji & Ralph Archuleta
Dissertation: "Subject-Oriented Finite Fault Inversions and their Applications"

Bachelor of Science, Honors Applied Mathematics — December 2012
McGill University, Montreal, Qc, Canada
Advisor: Prof. Jean-Christophe Nave

PROFESSIONAL EMPLOYMENT

09/13-Present	Graduate Student Researcher, Dept. of Earth Science, UCSB
Fall 2017	Teaching Associate, Dept. of Earth Science, UCSB
09/13-09/18	Teaching Assistant, Dept. of Earth Science, UCSB
09/12-06/13	Undergraduate Researcher, McGill University

PUBLICATIONS

Adams, M., Ji, C., & Hao, J. (2018). Energy based stress drop and its uncertainty during the 2015 Mw 7.8 Gorkha earthquake constrained by geodetic data and its implications to earthquake dynamics. In press.

Adams, M., Twardzik, C., & Ji, C. (2017). Exploring the uncertainty range of coseismic stress drop estimations of large earthquakes using finite fault inversions. *Geophysical Journal International*, ***208***(1), 86-100.

Ranalli, G., and **Adams**, M. (2013). Rheological contrast at the continental Moho: effects of composition, temperature, deformation mechanism, and tectonic regime. *Tectonophysics* **609**, 480-490. DOI: 10.1016/j.tecto.2012.10.037

AWARDS

- UCSB Graduate Dissertation Fellowship (2017)
- Archuleta Family Fellowship in Earth Science, UCSB (2017)
- Departmental Geophysics Award, UCSB (2016)
- Alumni Graduate Award for Research Excellence, UCSB (2015)
- Edward W. Beatty Entrance Scholarship to McGill University (2009)

FIELDS OF STUDY

Major Field: Seismology.
Studies in the development of numerical methods and their applications to earthquake source physics.

ABSTRACT

Subject-Oriented Finite Fault Inversions and their Applications

by

Mareike N. Adams

Accurate images of the growth of slip and faulting are critical in understanding the physics of earthquakes, and subsequently aid in the prediction of the ground motion that could be expected from future rupture events. Many methods, namely finite fault inversions, have been developed that use observed seismic waveforms and static deformations to constrain the spatiotemporal rupture evolutions of great earthquakes. This work explores the development of novel inversion methods to further the investigation into properties of earthquake physics.

Earthquakes lead to the overall reduction of stress across the ruptured fault plane, and stress drop is a key parameter in accurately estimating the strong ground motion. Thus, we have developed a new procedure to determine if it is possible to robustly constrain an uncertainty range for the co-seismic stress drop of large earthquakes. For a given earthquake, we loop through a series of target stress drops, and for each case we conduct a modified finite fault inversion to find the solution that matches the seismic and/or geodetic data, and also matches a prescribed stress drop value. From this, we can determine a relationship between the resulting misfit between our synthetic model and the

observations, and the pre-assigned target stress drop value.

This new inversion technique is applied to several rupture events with varying datasets in order to test its robustness. First, we examine the 2014 Mw 7.9 Rat Islands earthquake using far-field data and discovered that only the lower bound of the average stress drop could be well constrained. To investigate whether such a conclusion also holds for near field data, the slip distribution and the stress drop of the 2015 Mw 7.8 Gorkha, Nepal earthquake was studied using GPS and InSAR data. Our results revealed similar patterns: that even a comprehensive geodetic dataset could also only constrain the lower bound of stress drop. Furthermore, one of the important uses of stress drop for earthquake physics is in the study of energy partitioning. The average stress drop is equivalent to twice the ratio of apparent available energy to the total seismic potency, and so our result has a direct impact on the study of the earthquake energy budget. As stress drop is proportional to the available seismic energy, our results imply that only the lower bound of the available energy can be constrained.

The November 14th 2016 M_W 7.8 Kaikoura, New Zealand earthquake occurred along the northern part of the South Island. Available information indicates that this earthquake involved multiple fault segments of the Marlborough fault system (MFS). Additionally, slip might also have occured on the subduction interface of the Pacific Plate under the Australian Plate, beneath the MFS. The exact number of involved fault segments as well as the temporal co-seismic rupture sequence has not been fully determined. We propose two inversion strategies to determine the fault geometry and spatiotemporal rupture history: first we use teleseismic and strong motion waveforms to determine point-source

focal mechanisms for all of the faults that participated in the rupture; second, we use seismic and geodetic data to invert for the kinematic rupture parameters on a limited number of fault segments. The first approach allows us to determine a rupture timing sequence for different fault segments. Once we have the timing among fault segments, we invert the seismic and geodetic data for the spatial and temporal kinematic parameters. Both of these methods allow us to evaluate the potential of slip on the Hikurangi subduction interface.

TABLE OF CONTENTS

1. Introduction

Detailed mapping of the spatial and temporal slip distribution of large earthquakes is one of the principal goals of seismology. In the last few decades, many methods have been developed that use observed seismic waveforms and static deformations, such as GPS and InSAR data, to constrain the spatiotemporal rupture evolution of large events. The results have led to theoretical breakthroughs in earthquake physics and have been used to predict the damage of future large earthquakes.

These methods, which are classified as finite-fault inversions, involve finding the values of fault parameters, such as displacement and rupture velocity, which can minimize a misfit or objective function. This function characterizes the differences between observed and synthetic data calculated using a user-designed fault model and the propagation effects produced by an assumed Earth model. Despite the principal goal of retrieving the slip history of a particular rupture event, the strength of the finite fault inversion method is its flexibility and versatility. Analogous to subject-oriented programming (e.g., Harrison & Ossher, 1993), this method can be molded slightly differently based on the data types available and the types of operations applied to these data structures. My research involves the development of novel approaches or modifications of this particular inversion approach to further investigate certain properties of earthquake ruptures.

The modern scientific method is becoming increasingly intertwined with technology and relies more and more on our ability to include the ever-growing computational power into our approaches. In computing, subject-oriented programming is a software paradigm in which the state and behavior of objects are not seen as intrinsic

to the objects themselves, but are described by various subjective perceptions of the objects (e.g., Harrison & Ossher, 1993). For example, a tree to a passerby may have a measurable height or leaf-type, but for a bird this same tree may have a relative value for food or as a potential nesting location.

In classic finite fault inversions one investigates the temporal and spatial history of fault slip. One does not directly invert for other physical properties, such as on-fault stress change. Our goal is to manipulate established inversion methods to query the data about particular properties of the rupture. For example, what can our understanding of the rupture process tell us about the physical processes leading to varying amounts of ground shaking? Consequently, how can we relate our knowledge of subsurface fault physics to other problems such as surface seismic hazard analysis? What other physical properties of the dynamic Earth can be appraised just with a different perception and implementation of these methods? Thus, subject-oriented programming organizes classes that describe objects into "subjects", which can be combined to form larger subjects. Hence, we combine our tested finite fault inversion methods with hypothesized physical relationships and with growing computational power to push the boundaries of our geophysical knowledge.

In particular, earthquakes lead to the overall reduction of stress across the ruptured fault plane. Stress drop is an important physical parameter that has been long studied in seismology (e.g., Aki, 1967; Brune, 1970; Kikuchi & Fukao, 1988; Madariaga, 1979; Noda et al., 2013). Though the stress drop due to the rupture of a large earthquake is not spatially uniform, most often just its average value, $\overline{\Delta\tau}$, can be constrained with the limited seismic observations. Stress drop is a key parameter in accurately estimating the

strong ground motion (e.g., Brune, 1970; Hanks, 1979; Aki, 1984). Uncertainties in stress drop estimates lead to uncertainties in predicting seismic hazards (e.g., Cotton et al., 2013). Thus, one focus of my research has been to develop a new procedure to determine if it is possible to robustly constrain an uncertainty range for the co-seismic stress drop of large earthquakes. In particular, we use the energy based average stress drop ($\overline{\Delta\tau}_E$) (e.g., Kanamori & Allen 1986; Shao et al. 2012; Noda et al. 2013). In chapters two and three of my dissertation I will describe this novel inversion method and apply it to data from two major earthquakes: 2014 M_w 7.9 Rat Islands earthquake and 2015 M_w 7.8 Gorkha, Nepal earthquake.

The procedure is simple in concept. For each earthquake we consider a series of target stress drops; for each target we compute a modified finite fault inversion to find the solution that matches not only the seismic and/or geodetic data, but also matches the target stress drop. From this series of target stress drops we plot the overall misfit (the difference between synthetic seismograms and geodetic values and the observations) against the pre-assigned target stress drop.

In order to test the robustness of this subject-oriented finite fault inversion we consider several recent rupture events with varying datasets. First, we examine the 2014 M_w 7.9 Rat Islands earthquake using far-field data. Here we found that only the lower bound of the average stress drop could be well constrained. We then applied the same technique to the 2015 M_w 7.8 Gorkha, Nepal earthquake using only geodetic data, GPS and InSAR. Our results revealed a similar pattern to that found for the Rat Islands earthquake. Namely, we could only constrain a lower bound for the average stress drop.

One of the important uses of stress drop for earthquake physics is in the study of energy partitioning. The average stress drop is equivalent to twice the ratio of apparent available energy to the total seismic potency. Our result has a direct impact on the study of the earthquake energy budget (Heaton & Heaton, 1989). Apparent available energy can be divided into fracture energy, energy expended as the increased dissipation at the rupture front, and the rest as radiated seismic energy (Kanamori & Rivera, 2006). With stress drop proportional to the available seismic energy; our results imply that only the lower bound of the available energy can be constrained. Following this and strictly mathematically speaking, the inferred fracture energy then also has no detectable upper bound. However, because infinite stress and infinite fracture energy are not physically plausible, we must modify our finite fault inversion method to incorporate more physical constraints to constrain the important physical properties of large earthquakes. This will be explored in chapter 3.

The 2014 Rat Islands earthquake occurred below the central segment of the Aleutian Arc; it is the largest intermediate-depth earthquake recorded by modern instrumentation (Ye et al., 2014). It is a normal faulting event with a significant strike-slip component. In chapter 2 we use 30 P- and 31 SH-velocity waveforms recorded at teleseismic distances to study the slip history of this event and to test our inversion method with the added goal of determining an uncertainty range for the average static stress drop. We found that the waveform misfit associated with the inverted model decreases quickly as the average stress drop, $\overline{\Delta\tau}_E$, increases from 0.5 to 5.0 MPa, but varies negligibly as $\overline{\Delta\tau}_E$ increases from 10 to 50 MPa. Thus, the lower bound of this physical property is discernable, but its upper bound is unconstrained. We attribute this to

the limited resolution of the fine-scale roughness of the fault slip. As a consequence of not constraining the upper bound of the average stress drop, we cannot determine the upper bound of the available energy. However, we find that $\overline{\Delta\tau}_E$ correlates with the roughness of fault slip. This allows us to replace traditional arbitrary smoothing constraints on slip with a new physical constraint on smoothing that is based on the ability to determine a lower bound for $\overline{\Delta\tau}_E$.

In chapter 3 we study the slip and static stress drop of the 2015 M_w 7.8 Gorkha, Nepal earthquake. We use excellent near-source static observations in our finite fault inversion algorithm with the constraint on its average stress drop. Similarly, we find that with an appropriate subfault size, the misfit reduces as $\overline{\Delta\tau}_E$ increases to 7-8 MPa. The misfit then remains essentially constant, albeit with small fluctuations, as $\overline{\Delta\tau}_E$ increases. Our results reveal that only the lower bound of the average stress drop of the Gorkha earthquake (~7MPa) can be constrained with near fault geodetic measurements. This conclusion is consistent with the results in chapter 2 where we used far field seismic data in the inversion.

As the lower bound of $\overline{\Delta\tau}_E$ leads to a lower bound of the apparent available energy and an upper bound of the seismic radiation efficiency, this approach improves our understanding of the earthquake energy budget. We find that for an elongated rupture similar to the Gorkha earthquake, rupture could propagate fast but still dissipate most of the available energy in fracturing of the fault. We strongly support using the lower bound of the energy-based stress drop to replace arbitrary slip-smoothing constraints to stabilize finite fault inversions.

Additionally, finite fault inversion methods involve large assumptions about the fault geometry over which the rupture propagates. Generally, one large fault plane constitutes the rupture area, extending for several hundred kilometers. However, many earthquakes are made up of a multitude of connecting faults that may slip during a single earthquake. Consequently, knowledge of the kinematics of these complex fault interactions has important implications for our understanding of global seismic hazards.

The 2016 M_w 7.8 Kaikoura, New Zealand earthquake occurred along the east coast of the northern part of the South Island. The local tectonic setting is complicated with the central South Island being dominated by oblique continental convergence while the southern part of this island experiences eastward subduction (Kaiser et al., 2012). Available information (e.g., Hamling et al. 2017; Holden et al. 2017) indicate that this earthquake involved multiple fault segments of the Marlborough fault system (MFS) as the rupture propagated northwards for more than 150 km. Additional slip might also occur on the subduction interface of the Pacific Plate and the Australian Plate, beneath the MFS. However, the exact number of fault segments as well as the temporal co-seismic rupture sequence is uncertain despite the abundance of geodetic and geological observations. Thus, understanding the Kaikoura earthquake will hopefully provide insight into how one incorporates multi-fault ruptures into seismic-hazard models. In this final chapter, we will discuss the application of two different methods to study this rupture event: a multiple double-couple inversion to determine the spatiotemporal sequence of various fault planes involved (Shao et al., 2012), and a finite fault inversion using multiple datasets such as teleseismic, strong motion and purely static GPS offsets to produce a more detailed slip history of the complex event. We find that a combination of ten crustal faults, including offshore faults, can model the strong motion and static data.

1.1 References

Aki, K. (1984). Asperities, barries, characteristic earthquakes and strong motion prediction. *J. Geophys. Res.*, 89(B7), pp.5867–5872.

Aki, K. (1967). Scaling law of seismic spectrum. *Journal of Geophysical Research*, 72(4), pp.1217–1231. Available at: http://doi.wiley.com/10.1029/JZ072i004p01217.

Brune, J.N. (1970). Tectonic stress and the spectra of seismic shear waves from earthquakes. *Journal of Geophysical Research*, 75(26), pp.4997–5009.

Cotton, F., Archuleta, R. & Causse, M. (2013). What is Sigma of the Stress Drop ? *Seismological Research Letters*, 84(1), pp.42–48.

Hamling, I.J. et al. (2017). Complex multifault rupture during the 2016 Mw7.8 Kaikōura earthquake, New Zealand. *Science*, 356(6334).

Hank, T.C. (1979). b values and ω-ϒ seismic source models: Implication for tectonic stress variations along active crustal fault zones and the estimation of high-frequency strong ground motion. *J. Geophys. Res*, *84*, pp.2235-2242.

Harrison, W., & Ossher, H. (1993). *Subject-oriented programming: a critique of pure objects* (Vol. 28, No. 10, pp. 411-428). ACM.

Heaton, T.H. & Heaton, R.E. (1989). Static deformations from point forces and force couples located in welded elastic {Poissonian} half-spaces: Implications for seismic moment tensors. *Bulletin of the Seismological Society of America*, 79(3), pp.813–841. Available at: http://www.bssaonline.org/cgi/content/abstract/79/3/813.

Holden, C. et al. (2017). The 2016 Kaikōura Earthquake Revealed by Kinematic Source Inversion and Seismic Wavefield Simulations: Slow Rupture Propagation on a Geometrically Complex Crustal Fault Network. *Geophysical Research Letters*, 44(22), p.11,320-11,328. Available at:

http://doi.wiley.com/10.1002/2017GL075301.

Kaiser, A. et al. (2012). The Mw 6.2 Christchurch earthquake of February 2011: preliminary report. *New Zealand Journal of Geology and Geophysics*, 55(1), pp.67–90.

Kanamori, H. & Allen, C.R. (1986). Earthquake repeat time and average stress drop. *Earthquake source mechanics*. pp. 227–235.

Kanamori, H. & Rivera, L. (2006). Energy Partitioning During an Earthquake. *Earthquakes: Radiated Energy and the Physics of Faulting*, pp.3–13.

Kikuchi, M. & Fukao, Y. (1988). Seismic wave energy inferred from long-period body wave inversion. *Bulletin of the Seismological Society of America*, 78(5), pp.1707–1724.

Madariaga, R. (1979). On the Relation Between Seismic Moment and Stress Drop in the Presence of Stress and Strength Heterogeneity. *Journal of Geophysical Research*, 84(B5), pp.2243–2250.

Noda, H., Lapusta, N. & Kanamori, H. (2013). Comparison of average stress drop measures for ruptures with heterogeneous stress change and implications for earthquake physics. *Geophysical Journal International*, 193(3), pp.1691–1712.

Shao, G., Ji, C. & Hauksson, E. (2012). Rupture process and energy budget of the 29 July 2008 Mw 5.4 Chino Hills, California, earthquake. *Journal of Geophysical Research: Solid Earth*, 117(7), pp.2–13.

Ye, L., Lay, T. & Kanamori, H. (2014). The 23 June 2014 Mw 7.9 Rat Islands archipelago, Alaska, intermediate depth earthquake. *Geophysical Research Letters*, 41(18), pp.6389–6395.

and oceans.

2. Exploring the uncertainty range of co-seismic stress drop estimations of large earthquakes using finite fault inversions

This chapter appeared in this form in:

Adams, M., Twardzik, C., & Ji, C. (2017). Exploring the uncertainty range of coseismic stress drop estimations of large earthquakes using finite fault inversions. *Geophysical Journal International*, *208*(1), 86-100, https://doi.org/10.1093/gji/ggw374

2.1 Abstract

A new finite fault inversion strategy is developed to explore the uncertainty range for the energy based average co-seismic stress drop ($\overline{\Delta\tau_E}$) of large earthquakes. For a given earthquake, we conduct a modified finite fault inversion to find a solution that not only matches seismic and geodetic data but also has a $\overline{\Delta\tau_E}$ matching a specified value. We do the inversions for a wide range of stress drops. These results produce a trade-off curve between the misfit to the observations and $\overline{\Delta\tau_E}$, which allows one to define the range of $\overline{\Delta\tau_E}$ that will produce an acceptable misfit. The study of the 2014 Rat Islands Mw 7.9 earthquake reveals an unexpected result: when using only teleseismic waveforms as data, the lower bound of $\overline{\Delta\tau_E}$ (5-10 MPa) for this earthquake is successfully constrained. However, the same dataset exhibits no sensitivity to its upper bound of $\overline{\Delta\tau_E}$ because there is limited resolution to the fine scale roughness of fault slip. Given that the spatial resolution of all seismic or geodetic data is limited, we can speculate that the upper bound of $\overline{\Delta\tau_E}$ cannot be constrained with them. This has consequences for the earthquake energy budget. Failing to constrain the upper bound of $\overline{\Delta\tau_E}$ leads to the conclusions that 1) the seismic radiation efficiency determined from the inverted model might be significantly overestimated; 2) the upper bound of the average fracture energy E_G cannot be constrained by seismic or geodetic data. Thus, caution must be taken when investigating the characteristics of large earthquakes using the energy budget approach. Finally, searching for the lower bound of $\overline{\Delta\tau_E}$ can be used as an energy-based smoothing scheme during finite fault inversions.

2.2 Introduction

Seismologists use static stress drop ($\Delta\tau$) to denote the difference between the state of stress before and after the earthquake. In reality $\Delta\tau$ varies locally over the fault surface, and in most circumstances only its average ($\overline{\Delta\tau}$) can be retrieved using seismic (Brune, 1970) and/or geodetic observations. In the literature, this stress drop is generally defined as the stress drop averaged over an area on the fault surface ($\overline{\Delta\tau_A}$), i.e., $\overline{\Delta\tau_A} = \frac{1}{A}\int_A \Delta\tau dA$, here A is the area of the fault plane where slip has occurred. Previous studies based mainly on seismic data indicated that the median of earthquakes' average stress drop is roughly constant (3-4 MPa) over a large range of seismic moment (e.g., Kanamori & Anderson, 1975; Allmann & Shearer, 2009). However, it is of interest to point out that the stress drop estimates of individual earthquakes can deviate from this median value by a factor of 4 (Allmann & Shearer 2009; Cotton et al., 2013). As the strong ground motion parameters are often related with the stress drop, large uncertainties in stress estimation suggest large uncertainties in predicting seismic hazard (Cotton et al., 2013).

Such a large deviation in estimates of stress drop might reflect the intrinsic uncertainty introduced by the methods to estimate them; though the local tectonics (e.g., Scholz, 2000; Allmann & Shearer, 2007) and source physics (e.g., Candela et al., 2011) can also be the cause. Most available stress measurements, particularly for M_w<5 earthquakes, were made using Brune-type methods (e.g., Brune, 1970; Madariaga, 1976; Kaneko & Shearer, 2014) which assumes that earthquake rupture occurs on a circular fault plane with uniform stress drop and constant rupture velocity. Although there are some variations, the Brune-type stress drop of an earthquake (hereafter referred to as $\overline{\Delta\tau_B}$) can

be represented as $cM_0 f_c^3$, where M_0 and f_c are the seismic moment and the corner frequency of this event, respectively. Often, c is treated as a constant in practice (e.g., Allmann & Shearer, 2007) but it strongly depends on the pre-assumed rupture velocity (v_r) since $c \propto v_r^{-3}$. Regardless of the difficulty to estimate precisely the corner frequency and rupture velocity of an earthquake using seismic data, the rupture event often has heterogeneous slip on a noncircular fault area as suggested by the studies of large earthquakes (see the collection of slip models in http://equake-rc.info/SRCMOD, Mai & Thingbaijam (2014)). Significant discrepancy between $\overline{\Delta\tau_A}$ and $\overline{\Delta\tau_B}$ can also be produced if the difference in the shape of the slip distribution is ignored (Madariaga, 1979, Kaneko & Shearer, 2015). Unfortunately, because of the limited resolution of seismic observations, except in some unique observational conditions (e.g., Dreger et al., 2007; Kim et al, 2016) the shape of the slip distribution for small earthquakes cannot be precisely constrained.

For the relatively large earthquakes (M_w>5.5), researchers often have the luxury of directly estimating $\overline{\Delta\tau_A}$ using already published slip models (e.g., Somerville et al., 1999). Causse et al. (2013) recently estimated the average stress drop of 31 slip models of 21 crustal earthquakes (M_w 5.7-7.7). They concluded that finite-source rupture models could provide important information regarding the distribution of stress drop as their uncertainty analysis for the static stress drop yielded an aleatory variability (stemming from the natural randomness of the rupture) of 0.3, which is equivalent to deviating from the mean by a factor of ~2. This deviation is still significant but is considerably smaller than the average deviation in stress drop mentioned above.

On the other hand, the peak strong ground motion of large earthquakes is more closely related to the slip heterogeneity rather than the average slip over the entire rupture area. For example, Miyake et al. (2003) found that the strong ground motions were often generated in areas where the stress being released was the largest. These areas approximately coincided with the asperities, i.e., regions on the fault that have large slip relative to the average slip of the rupture area (e.g. Mai et al., 2005). The methods to estimate $\overline{\Delta\tau_B}$ and $\overline{\Delta\tau_A}$ either ignore or reduce the impact of such heterogeneity.

Shao et al. (2012a) recently introduced the weighted average stress drop ($\overline{\Delta\tau_W}$) to avoid the ambiguity in choosing the "effective" fault area (Somerville et al., 1999) when estimating the average stress drop. It is defined as:

$$\overline{\Delta\tau_W} = \frac{\int_A \Delta\tau D dA}{\int_A D dA} \qquad (1)$$

where D denotes the slip. When the rupture has uniform slip, $\overline{\Delta\tau_W}$ is the same as $\overline{\Delta\tau_A}$. In more natural heterogeneous cases, because the stress and slip distributions are correlated, i.e., fault patches with high co-seismic slip are often associated with high stress drop; $\overline{\Delta\tau_W}$ is larger than $\overline{\Delta\tau_A}$ (Shao et al., 2012). A careful theoretical analysis for this argument can be found in Noda et al. (2013). Using the 2008 M_w 5.4 Chino Hills earthquake as an example, $\overline{\Delta\tau_A}$ estimated by Shao et al. (2012) is 22 MPa, while $\overline{\Delta\tau_W}$ is 38 MPa, 72% larger. Two reasons motivate us to estimate $\overline{\Delta\tau_W}$ rather than $\overline{\Delta\tau_A}$. First, as the fault slip D is used to weight the local stress drop, $\overline{\Delta\tau_W}$ is more sensitive to the stress within asperities, which are often the regions that produce larger ground motion (e.g., Miyake et al, 2003). Second, Shao et al. (2012a) and Noda et al. (2013) noticed that $\overline{\Delta\tau_W}$ is

equivalent to twice the ratio of the "apparent" available energy ($\frac{1}{2}\int_A \Delta\tau \mathrm{DdA}$, Kanamori & Rivera, 2006) to the total seismic potency ($\int_A DdA$, Heaton & Heaton, 1989). It led Noda et al. (2013) to name it as the energy based average stress drop ($\overline{\Delta\tau_E}$), which we will also use during the rest of the discussion. Therefore, systematically studying the scaling relation of $\overline{\Delta\tau_E}$ is important for understanding the earthquake energy budget (Shao et al., 2012a; Noda et al., 2013).

The uncertainty of the estimate of the average stress drop caused by the non-uniqueness of slip inversions has not been fully explored despite this uncertainty affecting both the approximations of $\overline{\Delta\tau_A}$ and $\overline{\Delta\tau_E}$. Conventional finite fault inversion methods do not directly invert for on-fault stress change. Given the fact that slip models with different peak slip could fit the observations roughly equally well (e.g., Shao & Ji, 2012b), the variation of average stress drop could be significant. This contradicts somewhat the result of Causse et al. (2013). They studied the variation of average stress drop among published models of the same earthquakes and found that the epistemic variability is only 0.06, equivalent to deviating from the mean by a factor of ~1.15. However, the uncertainties of the average stress drop caused by widely used inversion regulations could be largely overlooked.

Here we develop a nonlinear finite fault inversion procedure to directly link the uncertainty of the energy based average stress drop with the misfit between synthetic and observed seismic waveforms. This algorithm allows us to search for the solution matching the observed seismic and/or geodetic data under the condition that the average

stress drop is close to a pre-assigned value, i.e. the target stress drop. We perform inversions with different target stress drops to obtain the relationship between the average stress drop of the inverted slip model and the minimum waveform misfit. As an example, we use P and SH displacement waveforms recorded at teleseismic distances from the 2014 Mw 7.9 Rat Island intermediate depth earthquake to determine its average stress drop, $\overline{\Delta\tau_E}$. An unexpected large uncertainty in the estimation is found. Our discussion will further reveal that such a large uncertainty will be associated with all finite fault inversions using surface observations.

2.3 Method

Assume that the rupture of an earthquake occurs on a rectangular fault plane, which is further divided into L_x (along-strike) by L_y (down-dip) cells or subfaults. We use (j, k) to denote the position of one subfault, i.e., $j=1, 2,..., L_x$ and $k=1, 2,..., L_y$. The hypocenter is at subfault (j_0, k_0). The displacement $u(t,\vec{x})$ at site $\vec{x}$ could be approximated as the summation of the contributions of a regular grid of subfaults (e.g., Olsen & Apsel, 1982, Hartzell & Heaton, 1983; Ji et al., 2002):

$$u(t,x) = \sum_{j=1}^{L_x}\sum_{k=1}^{L_y} D_{jk}[\cos(\lambda_{jk})\, Y_{jk}^1(t-\Delta t_{jk}) + \sin(\lambda_{jk})\, Y_{jk}^2(t-\Delta t_{jk})] * \dot{s}_{jk}(t) \quad (2)$$

Here, D_{jk} λ_{jk}, and $\dot{s}_{jk}(t)$ are the dislocation amplitude, rake angle, and rise-time function, respectively. The terms $Y_{jk}^1(t)$ and $Y_{jk}^2(t)$ are the subfault Green's functions for a unit slip in the strike direction and down-dip direction, respectively, and Δt_{jk} denotes the rupture initiation of the subfault. During conventional finite fault inversions, we constrain

the fault model $\boldsymbol{m}$ in terms of D_{jk}, λ_{jk}, and $\dot{s}_{jk}(t)$ by matching the synthetic seismograms and/or static displacements with the surface observations.

The slip on the fault surface will also lead to the stress change across the fault. The static shear stress drop at the center of subfault (*i, j*) can be estimated as

$$\tau_{ij}^{n}(m) = \sum_{k=1}^{L_x}\sum_{l=1}^{L_x}\left[D_{kl}^{1}(m)\sigma_{ij,kl}^{n,1} + D_{kl}^{2}(m)\sigma_{ij,kl}^{n,2}\right] \qquad (3)$$

where $\tau_{ij}^{n}\ (m);\ for\ n = 1,2$ denotes the left-lateral (n=1) or thrust shear (n=2) stress at this location, respectively for a given model $\boldsymbol{m}$, and $D_{kl}^{p}(m); for\ p = 1,2$ is the corresponding left-lateral (p=1) or thrust (p=2) displacements of the subfault (*k, l*). $\sigma_{ij,kl}^{n,p}$ is a kernel function, which states the shear stress response τ_{ij}^{n} caused by the unit D_{kl}^{p} and can be pre-calculated using various synthetic algorithms (e.g., Okada, 1992; Cotton et al., 1998). Therefore, the static stress drop at the center of each subfault can be estimated simultaneously with the slip distribution. An alternative approach that resamples the inverted slip distribution (e.g., Ripperger & Mai, 2004) will be considered in future efforts.

Following Shao et al. (2012a) and Noda et al. (2013), we calculate the energy based average stress of a model $\boldsymbol{m}$ as

$$\overline{\Delta\tau_E}(m) = \frac{\sum_{i=1}^{L_x}\sum_{j=1}^{L_y}\tau_{ij}(m)\cdot D_{ij}(m)}{\sum_{i=1}^{L_x}\sum_{j=1}^{L_y}D_{ij}(m)} \qquad (4)$$

where $\tau_{ij}(m)$ denotes the stress drop at the center of subfault (i,j) caused by the fault slip

of model $\boldsymbol{m}$.

During a conventional nonlinear finite fault inversion, we look for the solution that minimizes the following error function:

$$E(m) = E_{wf} + \lambda_1 E_{moment} + \lambda_2 E_{smooth} + \lambda_3 E_{time} \quad (5)$$

where $E_{wf}(m)$ denotes the cumulative misfit between the observed and synthetic seismograms (and/or static displacements). To stabilize the inversion, three additional types of regularizations are chosen: E_{moment} minimizes the difference between the inverted seismic moment and the value based on long period seismic data, such as the GlobalCMT solution (Ji et al., 2002); E_{smooth} minimizes the difference between the slip on adjacent subfaults using a Laplacian operator (Ji et al., 2002), and E_{time} compresses the irregularity of the rupture front (Shao et al., 2011). The weights λ_1, λ_2 and λ_3 have a default value of 0.1.

Since the average stress drop and slip distribution can now be determined concurrently, we can force the average stress drop of the inverted slip model to be close to a target value. This can be achieved by introducing a stress constraint, $E_{stress}(m)$, defined as $\left|\ln\left(\frac{\overline{\Delta\tau_E}(m)}{\tau_{target}}\right)\right|$. The logarithmic function is used to limit the range of variation and impact of this function. When $\overline{\Delta\tau_E}(m)$ is close to τ_{target}, $\left|\ln\left(\frac{\overline{\Delta\tau_E}(m)}{\tau_{target}}\right)\right|$ converges linearly to zero as $\frac{\left|\overline{\Delta\tau_E}(m)-\tau_{target}\right|}{\tau_{target}}$. The new error function then becomes,

$$E(m) = E_{wf} + \lambda_1 E_{moment} + \lambda_2 E_{smooth} + \lambda_3 E_{time} + \lambda_\tau E_{stress} \quad (6)$$

where λ_τ is the weight of the stress constraint. The weighting coefficient λ_τ is introduced to monitor the effect of minimizing the difference between the calculated stress drop and the target during the inversion. Our preliminary tests indicate that compared to the tradeoff between E_{wf} and E_{stress}, the interference between E_{stress} and E_{time} can be ignored. However, the interference between E_{stress} and E_{smooth} is significant. So in all subsequent inversions, we let λ_1 and λ_3 remain the default values of 0.1, choose a negligible λ_2 value of 10^{-4}, and carefully select λ_τ. On one hand, if there is conflict between E_{wf} and E_{stress}, the inversion using a small λ_τ might not be able to find a model matching τ_{target}. However, using a very large λ_τ and a small τ_{target} together, the simulated annealing inversion can freeze and fail to find the global optimal solution. In our study, for each pre-assigned stress drop, we conduct multiple finite fault inversions with gradually increasing λ_τ until the relative difference between τ_{target} and the stress drop of the inverted model becomes acceptable, i.e. <10%.

2.4 Applications

The 2014 M_w7.9 Rat Islands earthquake, which occurred below the central segment of the Aleutian Arc on June 23rd, 2014 at 20:53:09 UTC, is the largest intermediate-depth earthquake recorded by modern instrument (Ye et al., 2014). As shown in Figure 1, it is a normal faulting event but with a significant strike-slip component. Ye et al. (2014) and Twardzik & Ji (2015) have studied the slip history of this earthquake using teleseismic data. Although their inverted slip distributions are generally consistent, the inferred stress drop is significantly different. Ye et al. (2014) reported a stress drop of 11 MPa, while Twardzik & Ji (2015) estimated a range of 3.2-5.0 MPa using three representative slip

models. This discrepancy likely derives from the differences in estimating the shape and size of the rupture area, as both studies use $\overline{\Delta\tau_A}$ to determine the stress drop. Because we use the energy based stress drop in our study, we are not biased by the estimation of the rupture area. Thus, our approach might be able to shed some light on this discrepancy.

We adopt the same high angle rectangular fault plane as Twardzik and Ji (2015). It is oriented 308.40°N and dips 84.36° to the north-northeast, inferred from the GCMT solution (http://www.globalcmt.org). The fault plane is 178.5 km along-strike and extends 112.5 km down-dip. The fault plane spans a depth range of 51.5 to 163.5 km, with the hypocenter at a depth of 107.5 km. The fault plane is further divided into 315 subfaults measuring 8.5 km (along-strike) by 7.5 km (down-dip). As the fault slip, rake angle, rupture initiation time, and the shape of the asymmetric cosine function of each subfault are constrained simultaneously, there are a total of 1575 free parameters without considering the target stress drop. We use 30 P and 31 SH waveforms recorded at teleseismic distances. The station distribution is shown in Figure 1. We use velocity waveforms because they are, in principle, more sensitive to the finer details of the rupture process. The analysis using displacement waveforms has been conducted as well and can be found in the supplementary material (Figures S2-S6). The total number of wavelet coefficients used in this study is 12526. We use the Preliminary Reference Earth Model (PREM, Dziewonski and Anderson, 1981) without the water layer to approximate the earth structure and have pre-calculated a Green's function table, which has a frequency range from DC to 2 Hz, using the FK algorithm (Zhu and Rivera, 2002). The PREM Q model is included during the synthetic calculation. We interpolate the teleseismic responses at selected stations using this table.

Over the depth extent of the source, the rigidity of the PREM model changes from 6.64×10^4 to 6.76×10^4 MPa. Thus, a half-space model with constant rigidity of 6.7×10^4 MPa is a sufficient approximation to the source region of this earthquake. It allows us to quickly pre-calculate $\sigma_{ij,kl}^{n,1}$ and $\sigma_{ij,kl}^{n,2}$ using the program DC3D written by Okada (1992).

2.5 Results

We have tested sixteen different target stress drops ranging from 0.5 to 50 MPa. For each target stress drop, we let the weight of the stress constraint λ_τ change from a negligible value of 1.0×10^{-4} to 0.1, and select the model with the smallest λ_τ value under the condition that the difference between the average stress drop $\overline{\Delta\tau_E}$ and the target is less than 10%. Figure 2 shows the relationship between $\overline{\Delta\tau_E}$ of selected models and their waveform misfits. Readers can also find a visual representation of the relationship between the stress-coefficient λ_τ and $\overline{\Delta\tau_E}$, i.e. the waveform misfits for all 176 models, in Figure S1.

As shown in the upper-inset of Figure 2, the waveform misfit decreases quickly as $\overline{\Delta\tau_E}$ increases from 0.5 MPa to 4-5 MPa, and becomes essentially constant when $\overline{\Delta\tau_E}$ increases from 10 MPa to 50 MPa. It clearly illustrates the fact that seismic waveform data used here allows us to define the lower bound of the average static stress drop of an earthquake but fails to constrain its upper bound. The same relationship can be seen when displacement data is used (Figure S2). This result is counterintuitive. Seismologists are aware that the distribution of co-seismic stress drop inferred from source inversions is

often heterogeneous, and that local stress drop can be very large (e.g., Dreger et al., 2007; Shao et al., 2012; Causse et al., 2013). However, it is generally believed that the average stress drop of large earthquakes will be more stable, with an uncertainty less than a factor of two (e.g., Venkataraman & Kanamori, 2004; Causse et al., 2013).

To establish the lower bound of $\overline{\Delta\tau_E}$ for the Rat Islands earthquake, we examine models with a $\overline{\Delta\tau_E}$ of 2 to 15 MPa in closer detail (Figure 2). It can be seen that the value of the misfit function generally decreases with an increase in $\overline{\Delta\tau_E}$; it reaches the global minimum around $\overline{\Delta\tau_E}$ =10 MPa and then is nearly constant with small fluctuations (Figure 2). The misfit value of the model with a $\overline{\Delta\tau_E}$ of 8 MPa is slightly larger than that of the model with a $\overline{\Delta\tau_E}$ of 7 MPa. However, such a difference may also be caused by random variations in the initiation of the inversions. We have conducted 10 inversions with fixed target stress drops and stress constraint λ_τ but with different random seeds, which yield slightly different values for the misfit function. The standard deviation among these 10 models is $2.8\text{x}10^{-4}$ (Figure 2), which is compatible with the aforementioned difference between models with $\overline{\Delta\tau_E}$ of 7 and 8 MPa.

Figure 2 only illustrates the possibility of defining the lower bound of $\overline{\Delta\tau_E}$ using seismic data, its exact value is still model dependent and can vary within a small range. For example, as the fluctuations of the misfit function become much smaller beyond 10 MPa, it could be defined as the lower bound of $\overline{\Delta\tau_E}$. The mean misfit value of the models with $\overline{\Delta\tau_E}$ larger than 10 MPa is 0.2694 (black dashed line, Figure 2). If only considering the error caused by random seeds, we might argue that, with 95% confidence, the average

stress drop ($\overline{\Delta\tau_E}$) of this earthquake cannot be smaller than 5 MPa (red dashed line, Figure 2). The lower bound of $\overline{\Delta\tau_E}$ then falls in the range of 5-10 MPa. The estimate of the lower bound also slightly depends on using velocity waveforms or displacement waveforms. As shown in the Appendix (Figure S2), using the same procedure, the lower bound of $\overline{\Delta\tau_E}$ using displacement waveforms falls in the range of 7-10 MPa. During the following discussions, we choose the more conservative estimate of 5 MPa as the lower bound of $\overline{\Delta\tau_E}$.

To investigate the reason why seismic waveform fits are insensitive to the model with large $\overline{\Delta\tau_E}$, we first compare the synthetic seismograms predicted by these selected models. As a reference, Figure 3 shows the comparison of observations and synthetic seismograms predicted using the model with a $\overline{\Delta\tau_E}$ of 5 MPa. The synthetic seismograms visually match the velocity waveforms reasonably well, except at nodal stations such as OBN and KURK for P waves and KWAJ and KNTN for SH waves. To highlight the sensitivity to the average static stress drop of seismic data, we further compare the observations at four selected stations with the synthetic seismograms predicted using slip models with $\overline{\Delta\tau_E}$ from 0.5 to 4 MPa (Figure 4). The observations are depicted in dashed black lines while the red area represents the range of synthetic seismograms at any given time. It can be seen that the stress constraint indeed produces visible impacts to the synthetic seismograms. Relatively, the SH synthetic seismograms have a greater spread in values than P wave synthetic seismograms, indicating the inversion is more sensitive to SH waves than to the P waves. Furthermore, this range in synthetic waveforms is even more prominent in the displacement data (Figure S3-S4) as there exists larger variability

in the individual displacement waveforms. Figure 5 shows the same P wave and SH wave observations, but the red area now represents the range of synthetic waveforms predicted using the models with $\overline{\Delta\tau_E}$ from 5 to 50 MPa. These plots clearly show a much narrower range for the synthetics, particularly for the SH waves, than those for the low 0.5-4 MPa stress drops. This is unsurprising in view of the "flattening" of the misfit curve when $\overline{\Delta\tau_E}$ varies from 5 to 50 MPa (Figure 2).

Figure 5 also demonstrates that, with the current source representation and Green's functions, we have reached a certain point where our inversions are unable to improve the fit to the higher frequency signals. This can be taken as evidence that the true average stress drop of this earthquake is higher than the lower bound defined above. However, far field radiation can be represented as the spatial and temporal integration of the local moment rate functions. Then, if these functions lack high frequencies, the far field radiation will also lack the higher frequencies, regardless of whether local roughness of final slip on the fault is large or small. Hence, readers should be aware that, in principle, the difference between this lower bound of $\overline{\Delta\tau_E}$ and its true value is not correlated with the fit to the data. Improving the fit to the higher frequencies would very possibly, but not necessarily, lead to a closer estimate of $\overline{\Delta\tau_E}$.

Second, we explore the variations in slip and static stress drop distributions among these selected slip models with $\overline{\Delta\tau_E} \geq$ 5MPa. In Figures 6a and 6b the slip distributions of the models with $\overline{\Delta\tau_E}$ of 5 and 30 MPa are compared. Their moment rate functions are shown in Figure 7. For the convenience of further discussion, we refer to them as "Model-

5MPa" and "Model-30MPa", respectively. We find that as the $\overline{\Delta\tau_E}$ increases, the fine scale roughness of the slip distribution does change dramatically, but the centroid locations of the major asperities are approximately in the same places on the fault despite the increased fine-scale heterogeneity. As shown in Figure 6a, the Model-5MPa includes three major asperities. Asperity A has a dimension of 25 km (along strike) and 45 km (down-dip). The peak slip is approximately 1.9 m, and the hypocenter is located at its western edge. Most of the seismic slip occurs in asperity B, which roughly extends 60 km along strike from 20 km to 80 km, and spans from 90 km to 140 km in depth. The peak slip is 4.2 m. Asperity C is located at the east of asperity A, and has a dimension of 25 km along-strike and 30 km down-dip with a peak slip of ~2.8 m. The rupture initiates at asperity A and triggered the rupture of Asperity B at 12-13 s (Figure 7), and that of asperity C at 15 s. The effective rupture duration (the smallest time over which 95% of the total moment is released, Ekstrom and Engdahl (1989)) is 37 s, which is the same as previous analyses by Ye et al. (2014) and Twardzik and Ji (2015). In the slip distribution of Model-30MPa (Figure 6c), the centroids of asperities A and C are still in the same locations, but the asperity B splits into two parts, B1 and B2, along strike. It is of interest to note that asperity B1 is located at the east edge of asperity B in Model-5MPa, while asperity B2 is located at its western edge. This might suggest that the seismic waves are more sensitive to the edge of asperities, which are considered to be the regions radiating higher frequency seismic waves (Madariaga, 1977, 1983). The peak slip increases by about a factor of three from the low stress drop model to the higher one. Finally, the down-dip extensions of these asperities are generally consistent.

Figure 6c and 6d show the static stress drop distributions of Model-5MPa and Model-30MPa, respectively. Given that earthquakes have spatially variable slip, the stress drop is consequently highly variable on the fault plane. The more heterogeneous slip distribution of Model-30MPa leads to a more heterogeneous stress distribution (Figure 6d). The peak stress drop of Model-30MPa is about four times greater than Model-5MPa, compatible with the increase in the peak slip. The subfaults with large slip are also the subfaults with large stress drop, and negative stress drop (i.e. stress increase) appears in the vicinities of high slip patches. The high correlation between slip and stress distributions is the reason that $\overline{\Delta\tau_E}$ is always larger than $\overline{\Delta\tau_A}$.

Figure 7a compares the cumulative moment rate functions of three models: $\overline{\Delta\tau_E}$ of 2, 5 and 30 MPa, respectively. Regardless of the significant differences in $\overline{\Delta\tau_E}$, these moment rate functions are remarkably similar. Their effective rupture durations vary from 36 to 37 sec. They have similar energy concentrations, with the main pulses within the time window between 20 and 35 sec. The similarity of the moment rate functions to some extent explains why the teleseismic data alone cannot distinguish the selected models with $\overline{\Delta\tau_E}$ >5 MPa. This conclusion also can be seen in the spectra of these moment rate functions (Figure 7b). Similar rupture durations lead to similar corner frequency values, and then these models will have a similar $\overline{\Delta\tau_B}$ regardless of their big difference in $\overline{\Delta\tau_E}$.

Forcing the inverted model to have a given average stress drop can be viewed as a perturbation/constraint on the inversion process. It is of interest to investigate whether other kinematic parameters of the 2014 Rat Islands earthquake, such as average slip,

average rise time, average slip rate, and average rupture velocity of these models are affected by these average stress perturbations. Again, the fault slip is used as a weighting function because first, the kinematic parameters of the subfaults with larger slip are generally better constrained (e.g., Ji et al., 2002) and second, it can avoid the ambiguity of defining the "effective" fault plane. These parameters are calculated by:

$$\overline{D} = \frac{\sum_j \sum_k D_{jk}^2}{\sum_j \sum_k D_{jk}} \qquad (7a)$$

$$\overline{T} = \frac{\sum_j \sum_k D_{jk} T_{jk}}{\sum_j \sum_k D_{jk}} \qquad (7b)$$

$$\overline{\dot{D}} = \frac{\sum_j \sum_k D_{jk} \frac{D_{jk}}{T_{jk}}}{\sum_j \sum_k \boldsymbol{D_{jk}}} \qquad (7c)$$

$$\overline{v_r} = \frac{\sum_j \sum_k D_{jk} \frac{L_{jk}}{t_{jk}}}{\sum_j \sum_k D_{jk}} \qquad (7d)$$

where for the jk^{th} subfault T_{jk}, L_{jk} and t_{jk} denote its rise time, on-fault hypocenter distance, and rupture initiation time. $\overline{D}$, $\overline{T}$, $\overline{\dot{D}}$, and $\overline{v_r}$ are the weighted average slip, rise time, slip rate, and rupture velocity, respectively. Figure 8 shows their relationships with average static stress drop. As mentioned earlier, using the current dataset, the models with stress drop larger than 5 MPa are indistinguishable. Thus we will limit our attention to models with $\overline{\Delta\tau_E} \geq 5$ MPa. As $\overline{\Delta\tau_E}$ was forced to increase from 5 MPa to 50 MPa, the average slip changed from 2 m to 7 m, a factor of 3.5. Given that this change does not significantly affect the waveform fits, it is safe to conclude that the weighted average slip $\overline{D}$ is poorly constrained by the teleseismic data used in this study (Figure 8a). Figure 8b shows the variation in average rise time. There exists a tradeoff between spatial and

temporal resolution. The large rise times can smooth out high frequency radiation produced by a heterogeneous slip distribution. Thus, we might expect the average rise time to also increase with $\overline{\Delta\tau_E}$. However, Figure 8b exhibits a different trend. In fact, $\bar{T}$ stays nearly constant (3.94 $\pm$ 0.12 s) when $\overline{\Delta\tau_E}$ is less than 25 MPa but increases by 30% when $\overline{\Delta\tau_E}$ further increases by a factor of two to 50 MPa. Hence, the rise time estimate is robust to the perturbation in $\overline{\Delta\tau_E}$. Figure 8c shows the impact of the average rupture velocity from the hypocenter. We can see that this parameter is also very stable (~2.4$\pm$0.03 km/s), though we do see some notable variation when $\overline{\Delta\tau_E}$<5MPa. Finally, we estimate the weighted average slip rate, $\bar{\dot{D}}$ (Figure 8d), and again, we see that $\bar{\dot{D}}$ increases with the $\overline{\Delta\tau_E}$. However, the variation is much smaller compared to the variations of $\bar{D}$. Among the models with $\overline{\Delta\tau_E} \geq$ 5MPa, $\bar{\dot{D}}$ changes by a factor of 2 from 0.7 m/s to 1.4 m/s. For steady state dynamic rupture, the dynamic stress drop ($\overline{\Delta\tau_d}$) can be approximated as $\frac{\mu}{\pi v_r}\bar{\dot{D}}$ (Kanamori, 1994). The corresponding average dynamic stress drop varies from 7.7 MPa to 14.3 MPa. Unlike the nearly linear increase in $\bar{D}$, the increase of $\bar{\dot{D}}$ and $\overline{\Delta\tau_d}$ becomes much less when $\overline{\Delta\tau_E}$ is larger than 10 MPa.

2.6 Discussion

Before further discussion, it is worthwhile emphasizing that here we are studying the average source parameters of an earthquake. We suspect that the uncertainty of results should be related to the relative spatial resolution, i.e., the resolution relative to the entire fault length. In this perspective, the resolution issues we encounter during this study of the Mw 7.9 Rat Islands earthquake using teleseismic data are similar to what would be faced during the study of a M_w 6-7 earthquake using strong motion data. A teleseismic

study is also chosen to introduce this method because, in our experience, the azimuthal coverage of teleseismic data is often much better than a strong motion dataset for finite fault studies of large earthquakes. Furthermore, we admit that in the above analysis, several factors that can lead to significant uncertainties, such as station distribution, fault geometry, velocity structure, have been ignored. These factors can affect our estimates of the lower bound of $\overline{\Delta\tau_E}$ but will not affect our argument regarding the upper bound of $\overline{\Delta\tau_E}$.

The difficulty in constraining the upper bound of $\overline{\Delta\tau_E}$ leads us to question its practicality. While an earthquake has its respective $\overline{\Delta\tau_E}$, we cannot constrain its upper bound using far-field data. This can be explained intuitively using the two models (A and B) shown in Figure 9. The model A has unit slip (D=1) on a square fault patch with unit area (S=1). In model B, all slip uniformly concentrates in a small square patch with S=1/9, and at the center the slip is 9. Hence, the two models have the same potency as well as the same average slip within the solid gray box (S=1). Because the static stress drop of the uniform slip on a square patch can be represented as $c\mu D/S^{1/2}$, c is a constant, the peak static stress drop of model B is 27 times that of model A. The average stress drop $\overline{\Delta\tau_A}$ of models A and B over the solid gray box (S=1) are different by about 3 times. In fact, this ratio will be smaller if one considers the stress increase in the vicinity of the high stress drop/high slip patch. The $\overline{\Delta\tau_E}$ of the two models averaged over the same area changes by a factor of 27, which is the same as the difference in peak static stress drop. We could view model B as the true rupture scenario and model A as its approximation. They can represent the entire fault or a single subfault. When the seismic data is band-limited, it is

possible that both models will predict indistinguishable synthetic seismograms at surface stations. The simplest way to achieve this is to reduce the size of the solid gray box (Figure 9), i.e., reduce the size of the subfaults. Hence, for a given dataset, no matter whether one uses seismic or geodetic data, the upper bound of $\overline{\Delta\tau_E}$ cannot be fully constrained, as the subfault size can be reduced indefinitely. Note that this argument also holds for $\overline{\Delta\tau_A}$.

In this study, the finite fault inversion using seismic data matches the broadband seismic waveforms. It is well known that the spatial resolution of seismic data is proportional to the wavelength of the seismic signal (e.g., Spudich and Archuleta, 1987; Guatteri and Spudich, 2000; Shao and Ji, 2012). The long period signals can constrain the centroid location of the entire rupture (e.g., GlobalCMT), or individual asperities, depending on their wavelengths. Then, the images of small-scale heterogeneities of slip distributions rely on the high frequency signals. As far field high frequency observations are dominated by the signals excited along the edge of asperities (e.g., Madariaga, 1977), the locations of these asperity edges are often better imaged. However, the amplitude of final static slip at asperity edges are less well constrained because of the intrinsic trade-off between the rise time duration and slip in exciting high frequency signals. In other words, the rupture scenario with high total slip and long rise time can produce similar high frequency radiation as a rupture scenario with small total slip but short rise time. The difference between Figure 6a and Figure 6b illustrates the power and limitations of finite fault inversions using teleseismic data. This is different with the inversions using distant geodetic data, which are often poorer in constraining the edge of the asperities. The failure to constrain the small-scale roughness of fault slip with available seismic data is

the reason why the $\overline{\Delta\tau_E}$ of inverted slip models of the 2014 Rat Islands earthquake has no detectable upper bound.

Large small-scale roughness in fault slip leads to large local stress drops. The question is then whether it is possible to have very high local stress drops during one earthquake. Finite fault studies using some of the best available datasets have revealed that abnormally high stress drops at small spatial scales can indeed occur (e.g., Dreger et al., 2007; Shao et al., 2012; Beroza & Spudich, 1988; Ripperger & Mai, 2004). Dreger et al. (2007) indicated that the peak stress drop can be one order of magnitude larger than the frictional strength estimated using hydrostatic pore pressure and is consistent with shear strength determined from fresh rock fracture experiments (Ohnaka, 2003). If local stress drops can be very high, then high average stress drops cannot be completely ruled out.

2.6.1 Implications to the earthquake energy budget

As the average stress drop ($\overline{\Delta\tau_E}$) is equivalent to twice the ratio of the "apparent" available energy to the total seismic potency (Shao et al, 2012; Noda et al, 2013), our result has a direct impact on the study of the earthquake energy budget. From equation (1), the "apparent" available energy (ΔW_0) (Venkataraman & Kanamori, 2004; Kanamori & Rivera, 2006) can be approximated as

$$\Delta W_0 = \frac{1}{2}\int_A \Delta\tau \mathrm{D}\mathrm{d}\mathrm{A} = \frac{\overline{\Delta\tau_E} M_0}{2\mu} \qquad (8)$$

Here M_0 is the seismic moment and μ denotes the rigidity of the source region. Generally the seismic moment is well constrained for large earthquakes. As we showed above, we can give only a lower bound for $\overline{\Delta\tau_E}$. Consequently, we can only determine a lower

bound for the available energy of an earthquake. However, as pointed out by Noda et al. (2013), for a heterogeneous slip distribution $\overline{\Delta\tau_E}$ is always larger than either $\overline{\Delta\tau_A}$ or $\overline{\Delta\tau_B}$. In other words, the lower bound of ΔW_0 estimated using $\overline{\Delta\tau_E}$ would be larger than that estimated using $\overline{\Delta\tau_A}$ or $\overline{\Delta\tau_B}$.

The "apparent" available energy, ΔW_0, can be further divided into fracture energy (E_G), the energy that is expended as the increased dissipation at the rupture front, and the rest as radiated seismic waves (E_R) (e.g., Kanamori and Heaton, 2000; Abercrombie and Rice, 2005). Subsequently, we can define the seismic radiation efficiency (η_R) (e.g., Venkataraman & Kanamori, 2004) as:

$$\eta_R = \frac{E_R}{\Delta W_0} = \frac{E_R}{E_R + E_G} \qquad (9)$$

where E_R can be estimated using observed seismic data. In principle, the seismic radiation efficiency will be less than one. Venkataraman & Kanamori (2004) reported that for most crustal earthquakes they studied, η_R is larger than 0.25. However, for some well-studied earthquakes, such as the 1992 Landers earthquake, the estimate of η_R actually exceeds 1. Venkataraman & Kanamori (2004) suggested that it might imply that the rupture has a more complicated energy release scenario, e.g., one that allows undershoot, and so more energy than ΔW_0 can be released. Noda et al. (2013) noticed that the ΔW_0 estimated using $\overline{\Delta\tau_A}$ or $\overline{\Delta\tau_B}$ is smaller than that using $\overline{\Delta\tau_E}$, and then suggested that an underestimated ΔW_0 might be an alternative interpretation. Here, we further illustrate that ΔW_0 inferred from the slip model is only the lower bound of the "true" available energy, and subsequently the seismic radiation efficiency (η_R) might be overestimated. Ye et al. (2014) calculated the radiated energy of the 2014 Rat Islands earthquake and yielded an

estimate of 1.1-2.7x10^{16} J, dependent on the assumption of the Earth's attenuation. Using 5MPa as the lower bound for $\overline{\Delta\tau_E}$, the upper bound of η_R then ranges from 0.29 to 0.72. If we use 10MPa instead, the upper bound will be a factor of two smaller.

Even with considerable uncertainty, E_R can be estimated using seismic observations (e.g., Choy & Boatwright, 1995; Venkataraman & Kanamori, 2004). Then in a purely observational perspective, the estimate of E_G using distant data has no upper bound. Here fracture energy is defined in a slip-weakening constitutive friction law. For the rupture of natural earthquakes, it includes the energy losses due to all the processes other than the constant interface friction. These energies include those due to plastic yielding near the advancing fault tip, off-fault cracking, and thermal energies involved in fluid pressurization and melting (e.g., Kanamori & Rivera, 2006; Mai et al., 2006).

As mentioned above, the failure to constrain the small-scale roughness of fault slip with seismic data is the reason why an upper bound for $\overline{\Delta\tau_E}$ and the weighted average slip cannot be constrained; consequently the inferred fracture energy E_G also has no detectable upper bound. This result is consistent with previous observations. Analyzing the slip distributions of previous earthquakes suggested that E_G is not a constant. It scales with the average fault slip by ($log_{10}(E_G) \sim (1.28 - 1.35) log_{10}(\overline{D})$ (Abercrombie & Rice, 2005; Causse et al., 2013), and the degree of slip heterogeneity (Causse et al., 2013). The former might be caused by thermal lubrication (e.g., Kanamori & Heaton, 2000; Abercrombie & Rice, 2005; Di Toro et al., 2011). Causse et al., 2013 pointed out that if the degree of roughness of slip asperities reflects the fault surface irregularities, the latter can be explained with the laboratory result of Ohnaka & Shen (1999). They noticed that

E_G is correlated with irregularities on the fault surface. Hence, the models with higher $\overline{\Delta\tau_E}$ and $\overline{D}$ cannot be ruled out simply because of the consequent abnormally high fracture energy E_G.

However, physically speaking, the values of $\overline{\Delta\tau_E}$ and E_G of an earthquake cannot be infinite. Our above analysis basically rules out the possibility of constraining the upper bound of $\overline{\Delta\tau_E}$ of an earthquake using band-limited seismic and/or geodetic data. This argument might even hold for $\overline{\Delta\tau_A}$. Thus, new conditions/constraints have to be introduced to explore the upper limit. For instance, we might use the shear strength obtained from fresh rock fracture experiments (Ohnaka, 2003) to constrain the maximum local stress drop. Another plausible way is to assume that the heterogeneous stress can be modeled as a stochastic process (e.g., Smith and Heaton, 2011). Then one either inverts for the stochastic parameters using available data or directly adopts the results of previous studies. For example, assuming the degree of slip roughness reflects the fault surface irregularities, we might be able to constrain the inverted slip model with the scaling laws of fault roughness found in previous field or laboratory studies (e.g., Brodsky et al., 2016). However, this is beyond the scope of this article.

2.6.2 Implications to the study of intermediate depth earthquakes

A classic axiom in seismology is that the average stress drop of earthquakes is constant over all magnitudes (e.g., Aki, 1967,1972; Kanamori & Anderson, 1975). These studies and others indicate that shallow earthquakes have similar average stress drops. The median stress drop is nearly constant though there is significant scatter (e.g., Allmann & Shearer, 2009) with earthquakes over a wide range of magnitudes. It is noteworthy that in

these studies, the slip of rupture is assumed to be uniform and the small-scale heterogeneities are ignored. Intermediate depth and deep focus earthquakes (depth 70-670 km) have been shown to have higher stress drops, despite how the relationship of stress drop versus depth changes (e.g., Wyss & Molnar, 1972; Kikuchi & Fukao, 1987). Vallée (2013) recently systematically studied the durations and peaks of the moment rate functions of 1700 $6<M_w<9$ earthquakes estimated with teleseismic data. He found that the data is consistent with the hypothesis that the average strain drops of earthquakes are constant over depth. Then, the increase in stress drop with depth is due to the increase in shear modulus with depth. For the depth range of just intermediate depth earthquakes (70 km to 300 km), the shear modulus is about 2.6 times that of the upper crust. The result of Vallée (2013) suggests that the median of the average stress drop of intermediate depth earthquakes is in the order of 8 MPa. This is consistent with the lower bound of $\overline{\Delta\tau_E}$ for the 2014 Rat Islands earthquake found in this study.

However, as shown in Figure 7, the moment rate functions of the models with very different $\overline{\Delta\tau_E}$ (from 2 to 30 MPa) can have similar durations and peak amplitudes. In other words, the average stress/strain estimate based only on the duration and peak amplitude of an earthquake's moment rate function is not unique. Previous waveform analyses revealed that the along-strike extensions of large intermediate depth earthquakes are often much larger than the extensions in the down-dip direction (e.g., Tibi et al., 2002). The approach Vallée (2013) used considers, to some extent, the rupture heterogeneity of these intermediate depth earthquakes in the along-strike direction but still suffers from the uncertainty in the down-dip extensions. Note that when the duration and peak of a moment rate function are fixed, the width of the fault reduces by a factor of

two, and the stress drop will increase by a factor of four. In fact, evidence suggests that the stress drop estimate using near-epicenter records, which better constrains the rupture area, can be several times larger. For example, Takeo et al. (1993) estimated a stress drop of 42 MPa for the M_w7.6 1993 Kushiro-Oki, Japan earthquake using near- and far-field data and the aftershock distribution. Essentially, more work needs to be done to further constrain the lower bound of the average stress drop for intermediate depth and deep focus earthquakes.

2.6.3 Energy based smoothing constraint during the finite fault slip inversion

Finite fault source inversion is one of the most well known ill-posed geophysical inverse problems (e.g. Mai et al., 2016). Researchers often have to use hundreds to thousands of free parameters to represent the spatiotemporal earthquake rupture history, regardless of the fact that only a portion of them could be well constrained by the observations (e.g., Shao and Ji, 2012). Various regularizations are then used to stabilize the solution. A smoothing constraint applied to the fault slip is one that is used by most conventional inversion algorithms (e.g., Hartzell & Heaton, 1983). When several different models fit the data equally well, common in ill-posed situations, this regularization ensures that the solution with the smoothest slip distribution is chosen. As we discussed above, the inverted models with stress drop larger than 5 MPa are essentially indistinguishable using only teleseismic data. Because the models with higher $\overline{\Delta\tau_E}$ have more heterogeneous slip distributions (e.g., Figure 6), they will not be the final solution of the conventional inversion algorithms. We suspect this is the reason why the deviations of the average stress drop of earthquakes in previous studies are often limited (e.g., Causse et al., 2013).

The definition of slip roughness, which is minimized during the finite fault inversion, is not unique. For example, Hartzell & Heaton (1983) favored a simple smoothing scheme, i.e., $D_i - D_j \cong 0$, where D_i and D_j are the slip of adjacent subfaults. Because the slip difference between adjacent subfaults is related to the local stress drop, this constraint achieves a smoothing model by minimizing the local stress drop. Du et al. (1992) defined the fault roughness as the Laplacian of the inverted slip distribution along the fault surface. To some extent, this constraint achieves a smoothing model by minimizing the local gradient of inferred stress drop. If solving the finite fault inversion using singular value decomposition (SVD), the smoothing of the fault slip can also be achieved by properly truncating the small eigenvalues (Hartzell & Heaton, 1983). All of these methods can lead to smoothing, but their impacts on the inverted slip distributions are different. For example, the Laplacian smoothing method will have a stronger smoothing effect on the asperity edge than simply constraining the difference in slip between adjacent subfaults.

A trade-off exists between how well a model fits the data and also satisfies smoothing constraints that are used to stabilize the inversion. Their relative impacts to the overall misfit can be adjusted with a particular weight, such as in Equation 5. How to properly select the value of the smoothing constraint is one of the unanswered questions in seismology (e.g., Harris & Segall, 1987; Somerville et al., 1999; Sekiguchi et al., 2000). During our inversions, we have used the trial and error approach proposed by Hartzell & Heaton (1983), which is subjective to the modelers. On the other hand, more quantitative methods have been introduced. Ide et al. (1996), Sekiguchi et al. (2000) and Fukahata et al. (2004) proposed to select the weight value quantitatively using Akaike's Bayesian

Information Criterion (ABIC). Du et al. (1992) and Mendoza & Hartzell (2013) suggested selecting it by inspecting the trade-off curve between data misfit and roughness of the inverted slip, i.e. the L-curve (e.g., Henson & O'Leary, 1993; Mendoza & Hartzell, 2013). To some extent, this kind of curve is similar to what is shown in Figure 2, though here $\overline{\Delta\tau_E}$ replaces the roughness of inverted slip as the horizontal axis.

As shown in Figure 10, there is a positive correlation between the energy based average stress drop $\overline{\Delta\tau_E}$ and the fault roughness defined using the Laplacian of the inverted slip distribution. It implies that the smoothing of the inverted slip model can also be achieved by reducing the pre-assigned $\overline{\Delta\tau_E}$value. Therefore, to some extent, looking for the lower bound of $\overline{\Delta\tau_E}$ for a given earthquake is analogous to looking for the optimal weight of the aforementioned smoothing constraints during the finite fault inversion. Obviously, the lower bound of $\overline{\Delta\tau_E}$ has a much clearer physical meaning. With the current global seismic network, the seismic moment or potency of Mw>6 earthquakes can be well constrained. Then the search for the lower bound of $\overline{\Delta\tau_E}$ is equivalent to the search for the lower bound of the available energy. Each dataset has its individual spatial resolution of the fault slip, which controls the resolution of the lower bound of the available energy. Hence such a lower bound is extremely important for the scientists who want to use them. This new approach can be named as the energy based smoothing constraint. It can also be applied to the inversions using geodetic data. More in-depth aspects of this approach need to be explored to, for example, more quantitatively select $\overline{\Delta\tau_E}$ using the L-curve or ABIC method mentioned above. However, they are beyond the scope of this work and we leave it to future efforts.

2.7 Conclusion

The static stress drop varies locally over the fault surface. In most cases only its average value can be determined using seismic observations and often with large uncertainties. In this study, we focus on the energy based average stress drop $\overline{\Delta\tau_E}$ estimated from the inverted finite fault slip model. Conventional finite fault inversions do not directly invert for on-fault stress change; thus it is unclear whether models with significantly different stress drops can match the observations equally well. To address this concern, we developed a new nonlinear inversion strategy to explore the uncertainty range of $\overline{\Delta\tau_E}$ for large earthquakes. For a given earthquake, we loop through a series of target stress drops; for each case we conduct a modified finite fault inversion to find the solution that matches not only the seismic and geodetic data but also matches a prescribed $\overline{\Delta\tau_E}$. As an example, we use teleseismic waveforms to constrain $\overline{\Delta\tau_E}$ of the 2014 Mw 7.9 Rat Islands intermediate depth earthquake. We found that the waveform misfit associated with the inverted model decreases quickly as $\overline{\Delta\tau_E}$ increases from 0.5 MPa to 5.0 MPa, but varies negligibly as $\overline{\Delta\tau_E}$ increases from 10 MPa to 50 MPa. Hence we are able to define the lower bound of $\overline{\Delta\tau_E}$ but fail to constrain its upper bound. Our further investigation indicates that this is caused by the fact that teleseismic data only has limited resolution of the fine scale roughness of fault slip. Because the spatial resolutions of all seismic or geodetic data are limited, this leads to the conclusion that the upper bound of $\overline{\Delta\tau_E}$ cannot be determined from inversions of this data.

Regarding the earthquake energy budget, failing to constrain the upper bound of $\overline{\Delta\tau_E}$ leads to the following conclusions:

1) The upper bound of the available energy (e.g., Kanamori & Heaton, 2000) cannot be retrieved using only seismic and/or geodetic data.
2) The observed seismic radiation efficiency is close to its upper bound.
3) The upper bound of average fracture energy E_G cannot be retrieved only with seismic or geodetic data.

Forcing an inverted slip distribution to have a pre-assigned $\overline{\Delta\tau_E}$ will strongly influence the inversion. It impacts other average kinematic parameters as well. As expected, when $\overline{\Delta\tau_E}$ increases by one order-from 5 MPa to 50 MPa the weighted average slip increases monotonically 3.5 times. In contrast, the impact on the average rupture velocity is negligible, and the effect on the average rise time is much smaller (<30%). The average slip rate, which is influenced by both slip and rise time, increases by a factor of two, which might suggest that the average dynamic stress drop rises by a factor of two when the static stress drop increases by a factor of ten.

Finally, $\overline{\Delta\tau_E}$ is correlated with the roughness of fault slip. Looking for the lower bound of $\overline{\Delta\tau_E}$ for a given earthquake is analogous to looking for the optimal weight of the smoothing constraints during the finite fault inversion but with a much clearer physical meaning. Such an energy based smoothing scheme needs to be further investigated.

2.8 References

Abercrombie, R. E., & Rice, J. R., 2005. Can observations of earthquake scaling constrain slip weakening?, *Geophys. J. Int.*, **162**(2), 406-424.

Akaike, H., 1980. Likelihood and the Bayes procedure. *Trabajos de estadística y de investigación operativa*, **31**(1), 143-166.

Aki, K., 1967. Scaling law of seismic spectrum, *J. Geophys. Res.*, **72**, 1217-1231.

Aki, K., 1972. Scaling law of earthquake source time-function, *Geophysical Journal International*, **31**(1-3), 3-25.

Allmann, B.P. & Shearer, P.M., 2007. Spatial and temporal stress drop variations in small earthquakes near Parkfield, California, *J. Geophys. Res.*, **112**, B04305, doi:10.1029/2006JB004395.

Allmann, B.P. & Shearer, P.M., 2009. Global variations of stress drop for moderate to large earthquakes, *J. Geophys. Res.*, **114**, B01310, doi:10.1029/2008JB005821.

Beroza, G. C., and P. Spudich, 1988. Linearized Inversion for Fault Rupture Behavior - Application to the 1984 Morgan-Hill, California, Earthquake, *J. Geophys. Res.*, **93** (B6), 6275-6296.

Brodsky, E. E., Kirkpatrick, J. D., & Candela, T., 2016. Constraints from fault roughness on the scale-dependent strength of rocks, *Geology*, **44**(1), 19-22.

Brune, J.N., 1970. Tectonic stress and the spectra of seismic shear waves from earthquakes, *J. Geophys. Res.*, **75**, 4997-5009.

Candela, T., Renard, F., Bouchon, M., Schmittbuhl, J., & Brodsky, E., 2011. Stress drop during earthquakes: effect of fault roughness scaling, *Bull. Seismol. Soc. Am.*, **101**(5), 2369-2387.

Causse, M., Dalguer, L.A., & Mai, P.M., 2013. Variability of dynamic source parameters

inferred from kinematic models of past earthquakes, *Geophys. J. Int.*, doi: 10.1093/gji/ggt478.

Choy, G. L., & Boatwright, J. L., 1995. Global patterns of radiated seismic energy and apparent stress. *J. of Geophys. Res.*, **100**(B9), 18205-18228.

Cotton, F., Archuleta, R., & Causse, M., 2013. What is Sigma of the Stress Drop? *Seism. Res. Lett.*, **84**, 42-48, doi: 10.1785/0220120087.

Cotton, F., Berge, C., Lemeille, F., Pitarka, A., Lebrun, B., & Vallon, M., 1998. Three-dimensional simulation of earthquakes in the Grenoble's basin, *The Effects of Surface Geology on Seismic Motion*, **2**, 873-878.

Di Toro, G., Han, R., Hirose, T., De Paola, N., Nielsen, S., Mizoguchi, K., ... & Shimamoto, T., 2011. Fault lubrication during earthquakes, *Nature*, **471**(7339), 494-498.

Dreger, D., Nadeau, R. M., & Chung, A., 2007. Repeating earthquake finite source models: Strong asperities revealed on the San Andreas Fault, *Geophys. Res. Lett.*, **34**, L23302. doi:10.1029/2007GL031353

Du, Y., Aydin, A., & Segall, P., 1992. Comparison of various inversion techniques as applied to the determination of a geophysical deformation model for the 1983 Borah Peak earthquake, *Bull. Seismol. Soc. Am.*, **82**(4), 1840-1866.

Dziewonski, A. M., & Anderson, D. L., 1981. Preliminary reference Earth model, *Physics of the earth and planetary interiors*, **25**(4), 297-356.

Ekström, G., & Engdahl, E. R. (1989). Earthquake source parameters and stress distribution in the Adak Island region of the central Aleutian Islands, Alaska. *J. of Geophys. Res.*, *94*(B11), 15499-15519.

Fukahata, Y., Nishitani, A., & Matsu'ura, M., 2004. Geodetic data inversion using ABIC to estimate slip history during one earthquake cycle with viscoelastic slip-response functions, *Geophys. J. Int.*, **156**(1), 140-153.

Guatteri, M., & Spudich, P., 2000. What can strong-motion data tell us about slip-weakening fault-friction laws?. *Bull. Seismol. Soc. Am.*, **90**(1), 98-116.

Hansen, P. C., & O'Leary, D. P., 1993. The use of the L-curve in the regularization of discrete ill-posed problems, *SIAM Journal on Scientific Computing*, **14**(6), 1487-1503.

Harris, R. A., & Segall, P., 1987. Detection of a locked zone at depth on the Parkfield, California, segment of the San Andreas fault, *J. Geophys. Res.*, **92**(B8), 7945-7962.

Hartzell, S. H., & Heaton, T. H. (1983). Inversion of strong ground motion and teleseismic waveform data for the fault rupture history of the 1979 Imperial Valley, California, earthquake, *Bull. Seismol. Soc. Am.*, **73**(6A), 1553-1583.

Heaton, T. H., & Heaton, R. E., 1989. Static deformations from point forces and force couples located in welded elastic Poissonian half-spaces: Implications for seismic moment tensors, *Bull. Seismol. Soc. Am.*, **79**(3), 813-841.

Ide, S., Takeo, M., & Yoshida, Y., 1996. Source process of the 1995 Kobe earthquake: Determination of spatio-temporal slip distribution by Bayesian modeling, *Bull. Seismol. Soc. Am*, **86**(3), 547-566.

Ji, C., Wald, D.J., & D.V. Helmberger (2002). Source description of the 1999 Hector Mine, California, earthquake, Part I: Wavelet domain inversion theory and resolution analysis, *Bull. Seismol. Soc. Am.* **92**, 1192-1207.

Kanamori, H., 1994. Mechanics of Earthquakes, *Ann. Rev. Earth Planet. Sci.*, **22**, 207-37.

Kanamori, H. & Anderson, D.L., 1975. Theoretical basis of some empirical relations in seismology, *Bull. Seismol. Soc. Am.*, **65**(5), 1073-1095.

Kanamori, H., & Heaton, T. H., 2000. Microscopic and macroscopic physics of earthquakes. *Geocomplexity and the Physics of Earthquakes*, 147-163.

Kanamori, H., & Rivera, L, 2006. Energy partitioning during an earthquake, *Earthquakes: Radiated Energy and the Physics of Faulting*, AGU Monograph, Eds., Abercrombie, McGarr and Kanamori, 3-13.

Kaneko, Y. & Shearer, P.M., 2014. Seismic source spectra and estimated stress drop derived from cohesive-zone models of circular subshear rupture, *Geophys. J. Int.*, doi: 10.1093/gji/ggu030.

Kaneko, Y., & Shearer, P. M., 2015. Variability of seismic source spectra, estimated stress drop, and radiated energy, derived from cohesive-zone models of symmetrical and asymmetrical circular and elliptical ruptures, *J. of Geophys. Res.*, **120**(2), 1053-1079.

Kikuchi, M., & Fukao, Y., 1987. Inversion of long-period P-waves from great earthquakes along subduction zones, *Tectonophysics*, **144**(1), 231-247.

Kim, A., Dreger, D. S., Taira, T., & Nadeau, R. M., 2016. Changes in repeating earthquake slip behavior following the 2004 Parkfield main shock from waveform empirical Green's functions finite-source inversion, *J. of Geophys. Res.: Solid Earth*, **121**(3), 1910-1926. doi:10.1002/2015JB012562

Madariaga, R., 1976. Dynamics of an expanding circular fault, *Bull. Seismol. Soc. Am.*, **66**, 639-667.

Madariaga, R., 1977. High-frequency radiation from crack (stress drop) models of earthquake faulting, *Geophys. J. Int.*, **51**(3), 625–651. http://doi.org/10.1111/j.1365-246X.1977.tb04211.x

Madariaga, R., 1979. On the relation between seismic moment and stress drop in the presence of stress and strength heterogeneity, *J. Geophys. Res.*, **84**, 2243-2250.

Madariaga, R., 1983. High frequency radiation from dynamic earthquake fault models, *Annales Geophys*, **1**(1), 17-23.

Mai, P.M., Page, M., Schorlemmer, D., Ampuero, J.-P., and 21 other authors, 2016. The earthquake source inversion validation (SIV) exercise, *Seis. Res. Lett.*, **87** (3), 690-708. doi: 10.1785/0220150231

Mai, P. M., Somerville, P., Pitarka, A., Dalguer, L., Song, S., Beroza, G., ... & Irikura, K., 2006. On scaling of fracture energy and stress drop in dynamic rupture models: Consequences for near-source ground-motions, *Earthquakes: Radiated Energy and the Physics of Faulting*, 283-293.

Mai, P. M., Spudich, P., & Boatwright, J., 2005. Hypocenter locations in finite-source rupture models. *Bull. Seismol. Soc. Am.*, **95**(3), 965–980. http://doi.org/10.1785/0120040111

Mai, P. M., & Thingbaijam, K. K. S., 2014. SRCMOD: An Online Database of Finite-Fault Rupture Models, *Seismological Research Lett.*, **85**(6), 1348–1357. http://doi.org/10.1785/0220140077

Mendoza, C., & Hartzell, S., 2013. Finite-fault source inversion using teleseismic P waves: Simple parameterization and rapid analysis, *Bull. Seismol. Soc. Am.*, **103**(2013), 834-844.

Miyake, H., Iwata, T., & Irikura, K., 2003. Source characterization for broadband ground-motion simulation: Kinematic heterogeneous source model and strong motion generation area, *Bull. Seismol. Soc. Am.*, **93**(6), 2531-2545.

Noda, H., Lapusta, N., & Kanamori, H., 2013. Comparison of average stress drop measures for ruptures with heterogeneous stress change and implications for earthquake physics, *Geophys. J. Int.*, doi: 10.1093/gji/ggt074.

Ohnaka, M., 2003. A constitutive scaling law and a unified comprehension for frictional slip failure, shear fracture of intact rock, and earthquake rupture, *J. Geophys. Res.*: *Solid Earth*, **108**(B2).

Ohnaka, M., & Shen, L. F., 1999. Scaling of the shear rupture process from nucleation to dynamic propagation: Implications of geometric irregularity of the rupturing surfaces. *J. Geophys. Res.*, **104**(B1), 817-844.

Okada, Y., 1992. Internal deformation due to shear and tensile faults in a half-space, *Bull. Seismol. Soc. Am.*, **82**(2), 1018-1040.

Olson, A. H., & Apsel, R. J., 1982. Finite faults and inverse theory with applications to the 1979 Imperial Valley earthquake, *Bull. Seismol. Soc. Am.*, **72**(6A), 1969-2001.

Ripperger, J. & Mai, P.M., 2004. Fast computation of static stress changes on 2D faults from final slip distributions, *Geophys. Res. Lett.*, **31**(18).

Scholz, C., 2000. Evidence for a strong San Andreas fault, *Geology*, **28**(2), 163-166, doi: 10.1130/0091-7613(2000)28<163:EFASSA>2.0.CO;2

Sekiguchi, H., Irikura, K., & Iwata, T., 2000. Fault geometry at the rupture termination of the 1995 Hyogo-ken Nanbu earthquake, *Bull. Seismol. Soc. Am.*, **90**(1), 117-133.

Shao, G. F., Li, X. Y., Ji, C., & Maeda, T., 2011. Focal mechanism and slip history of the 2011 M-w 9.1 off the Pacific coast of Tohoku Earthquake, constrained with teleseismic body and surface waves, *Earth, Planets Space*, **63**(7), 559-564**.**

Shao, G., Ji, C., & Hauksson, E., 2012a. Rupture process and energy budget of the 29 July 2008 M_W5.4 Chino Hills, California, earthquake, *J. Geophys. Res.*, **117**, B07307, doi:10.1029/2011JB008856.

Shao, G., & Ji, C., 2012b. What the exercise of the SPICE source inversion validation BlindTest 1 did not tell you, *Geophys. J. Int.*, **189**(1), 569-590.

Smith, D. E., & Heaton, T. H., 2011. Models of stochastic, spatially varying stress in the crust compatible with focal-mechanism data, and how stress inversions can be biased toward the stress rate, *Bull. Seismol. Soc. Am.*, **101**(3), 1396-1421.

Somerville, P.G. *et al.*, 1999. Characterizing crustal earthquake slip models for the prediction of strong ground motion, *Seismol. Res. Lett.*, **70**, 59-80.

Spudich, P., & Archuleta, R. J., 1987. Techniques for earthquake groundmotion calculation with applications to source parameterization of finite faults, *Seismic strong motion synthetics*, **37**, 205-265.

Takeo, M., Ide, S., & Yoshida, Y., 1993. The 1993 Kushiro-Oki, Japan, Earthquake: A high stress-drop event in a subducting slab, *Geophys. Res. Lett.*, **20**(23), 2607-2610.

Tibi, R., Bock, G., & Estabrook, C. H., 2002. Seismic body wave constraint on mechanisms of intermediate-depth earthquakes. *J.Geophys. Res.*, **107**(B3).

Twardzik, C., & Ji, C., 2015. The M_W7.9 2014 intraplate intermediate-depth Rat Islands earthquake and its relation to regional tectonics, *Earth and Planetary Science Letters*, **431**, 26-35.

Vallée, M. (2013). Source time function properties indicate a strain drop independent of earthquake depth and magnitude. *Nature communications*, **4**.

Venkataraman, A. & Kanamori, H., 2004. Observational constraints on the fracture energy of subduction zone earthquakes, *J. Geophys. Res.*, **109**, B05302, doi:10.1029/2003JB002549.

Wyss, M., & Molnar, P., 1972. Source parameters of intermediate and deep focus earthquakes in the Tonga arc, *Phys. Earth and Planet. Int.*, **6**(4), 279-292.

Ye, L., Lay, T., & Kanamori, H., 2014. The 23 June 2014 M_W 7.9 Rat Islands archipelago, Alaska, intermediate-depth earthquake, *Geophys. Res. Lett.*, **41**(18), 6389-6395.

Zhu, L., & Rivera, L. A., 2002. A note on the dynamic and static displacements from a point source in multilayered media, *Geophys. J. Int.*, **148**(3), 619-627.

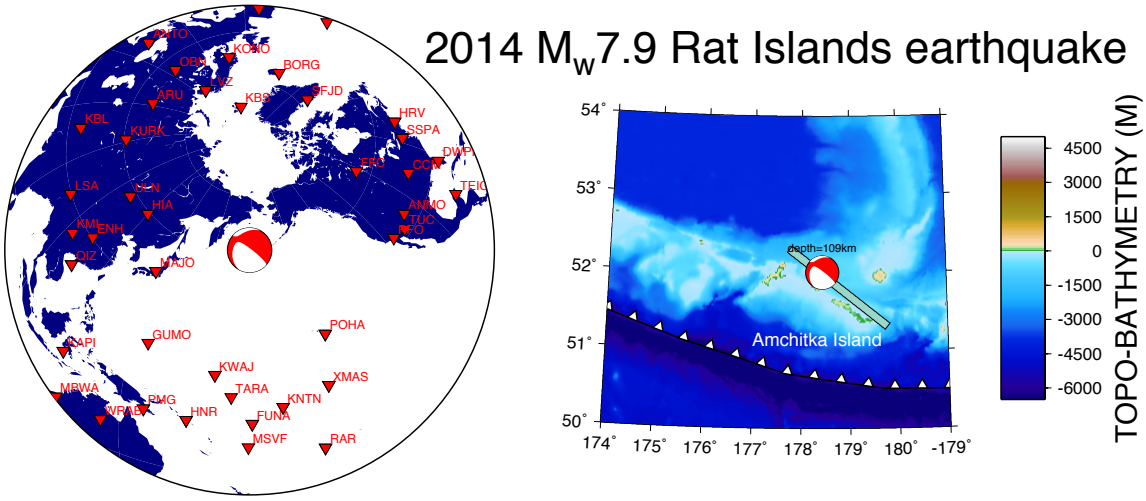

Figure 1: Left: Location and GCMT focal mechanism of the 2014 Mw 7.9 Rat Islands earthquake with the positions and names of the global seismic stations used (red triangles). **Right:** Surface projection of the causative high-angle fault plane superimposed on a map of the bathymetry of the Aleutian arc.

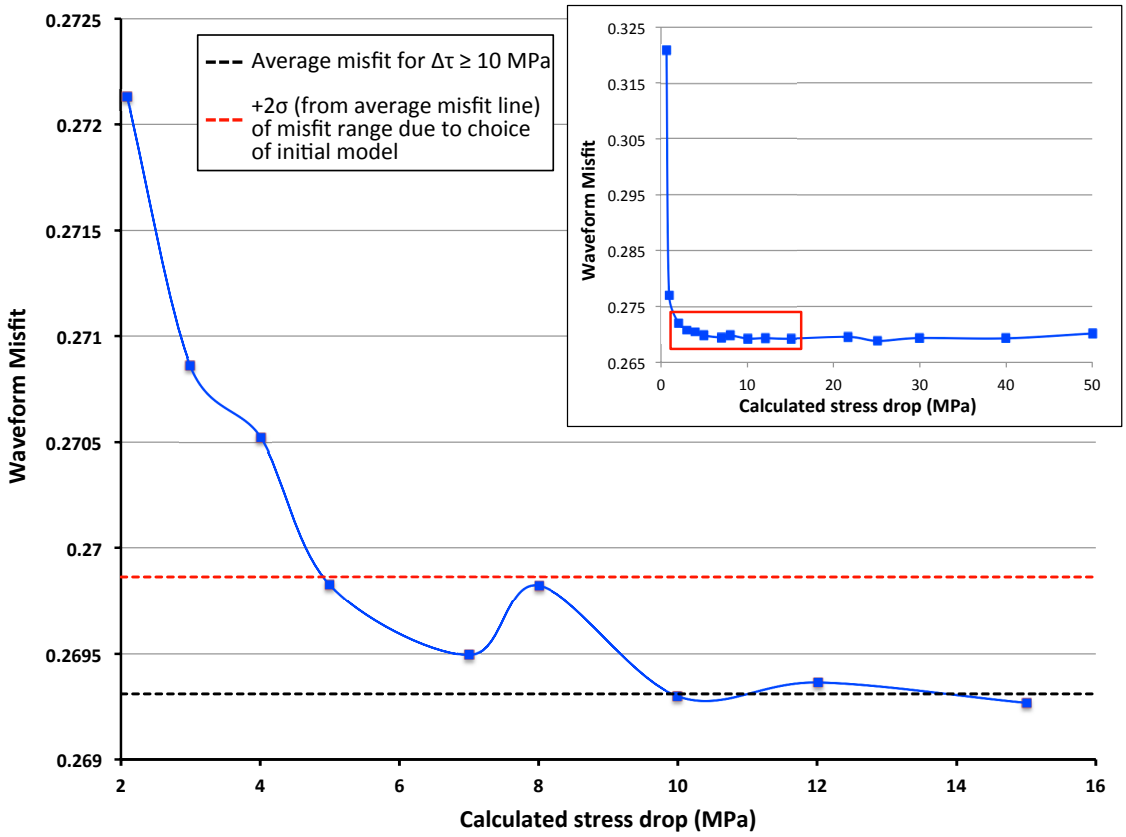

Figure 2: Energy based average stress drop ($\overline{\Delta\tau_E}$) of selected inverted slip models versus the corresponding waveform misfit. Upper-right inset shows the entire range of stress drops we have surveyed. Note that the waveform misfit is essentially constant when $\overline{\Delta\tau_E}$ is larger than 10 MPa. The red box highlights the stress range of 2-15 MPa, which is enlarged as the main figure. The black dashed line denotes the average misfit for inverted models with $\overline{\Delta\tau_E}$ ≥10 MPa. The red dashed line then denotes this average line plus two times the standard deviation of the waveform misfit range due to the choice of the initial model. See text for details.

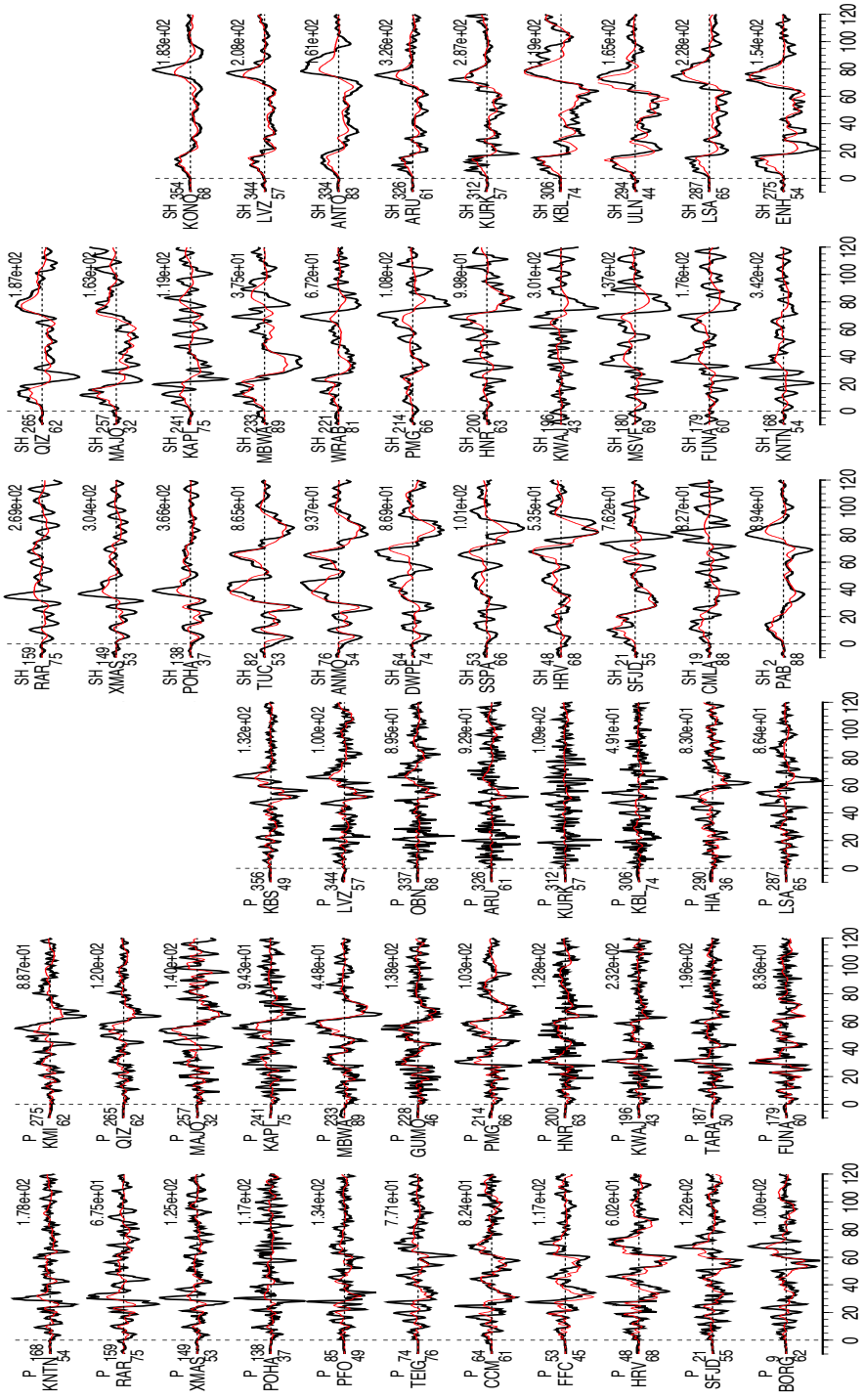

Figure 3: Comparison of 61 teleseismic P and SH velocity waveforms (black lines) and synthetic seismograms (red lines) predicted by the inverted model with $\overline{\Delta\tau_E}$ equal to 5 MPa. The station names are indicated to the left of the traces, along with the epicenter distance and azimuthal angle in degrees. At the end of each trace, the peak amplitude of the observation (μm/sec) is given.

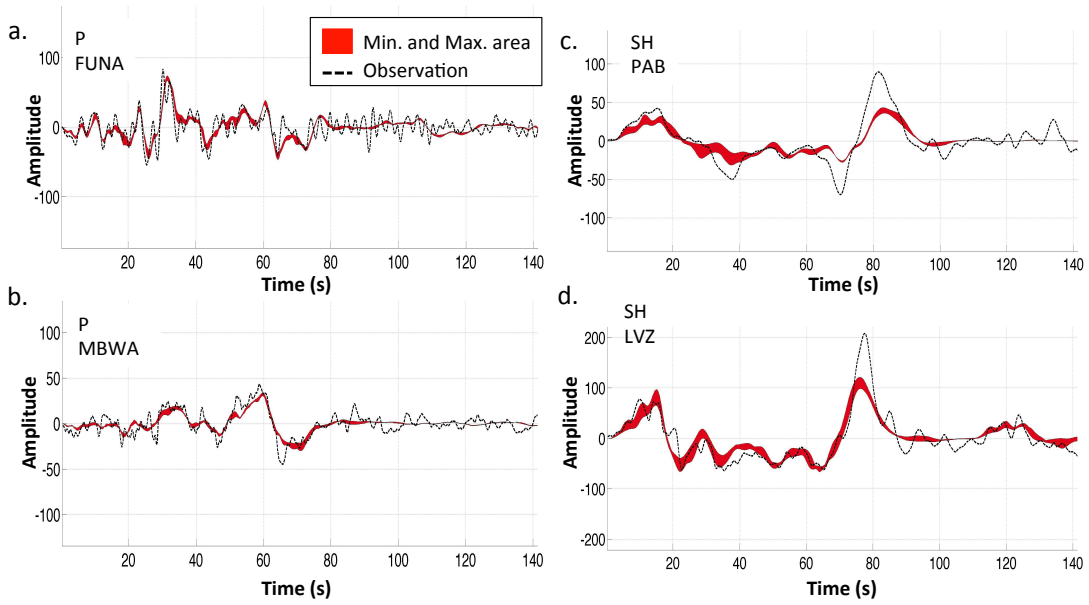

Figure 4: Comparison of P and SH synthetic seismograms at select stations. The red area shows the range of synthetic waveforms predicted using the inverted fault models with $\overline{\Delta\tau_E}$ ranging from 0.5 to 4 MPa. The observation is plotted as the black dashed line for comparison.

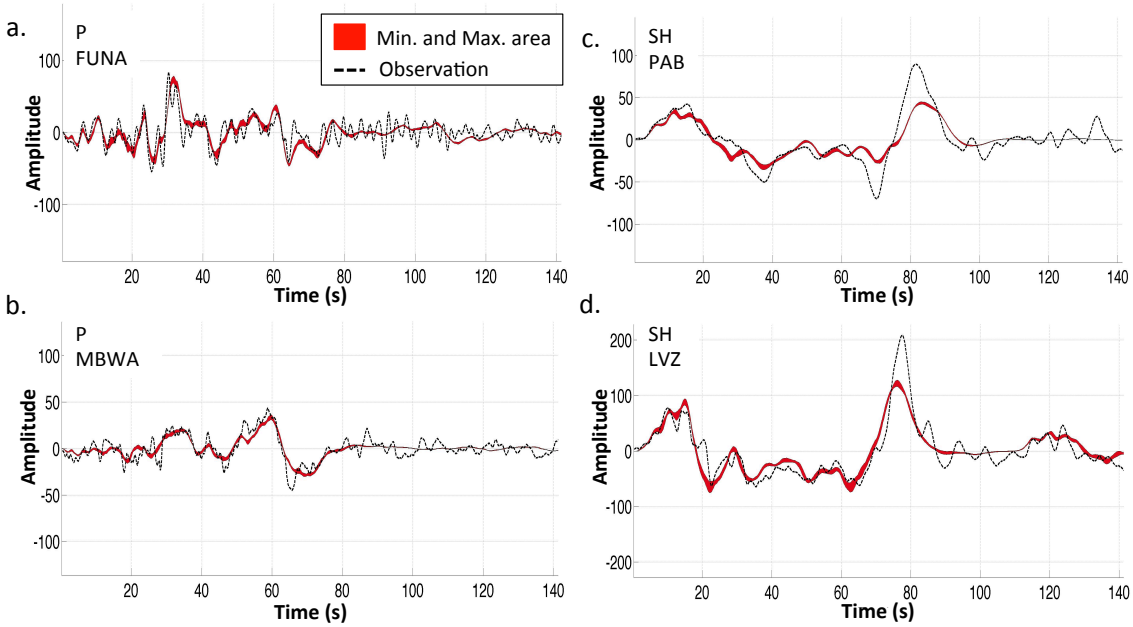

Figure 5: Similar to Figure 4 but here the red area shows the range of synthetic waveforms predicted using the inverted fault models with $\overline{\Delta\tau_E}$ from 5 to 50 MPa.

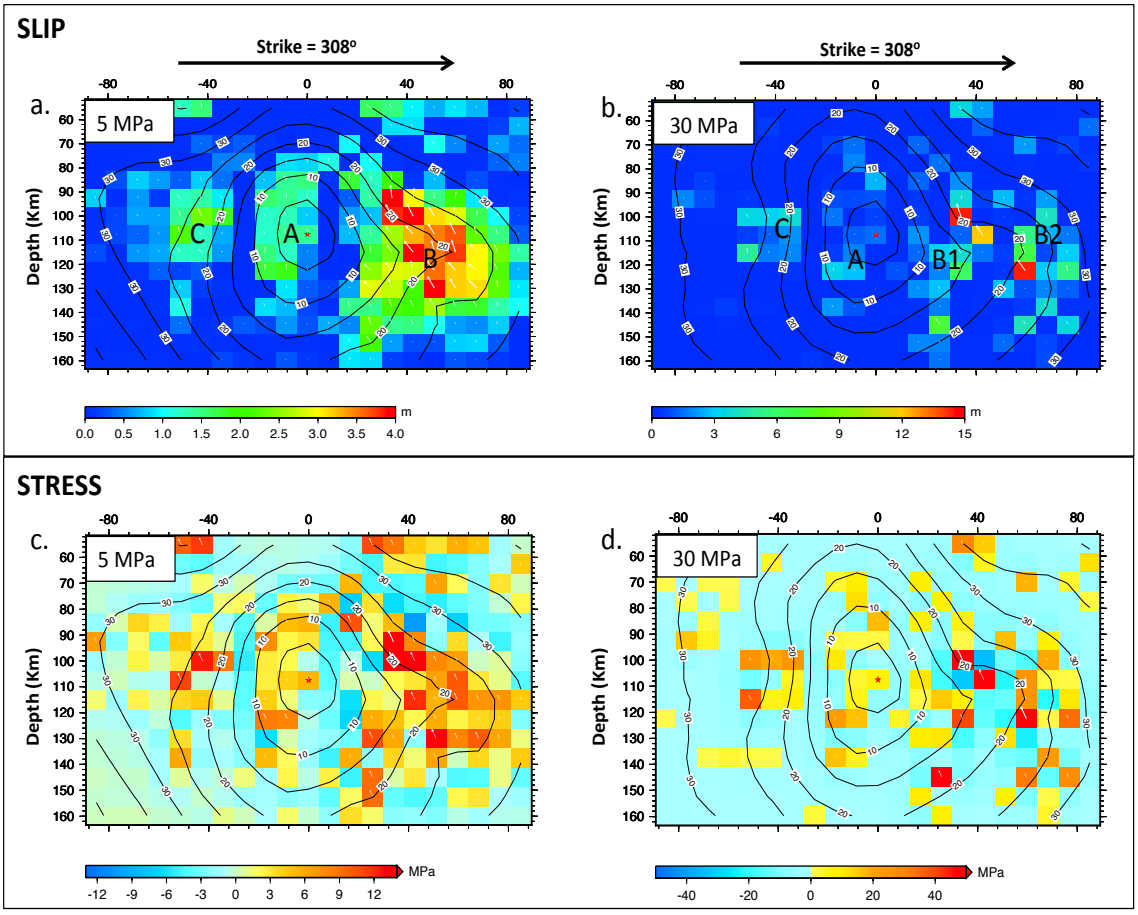

Figure 6: (a) Slip distribution of the Model-5MPa. A, B and C label the three major asperities; (b) slip distribution of the Model-30MPa. (c) and (d) show the stress drop distributions of these two models respectively. Color denotes the amplitude of the slip or stress drop. The contour lines show the rupture initiation locations at 5 sec intervals. See text for details.

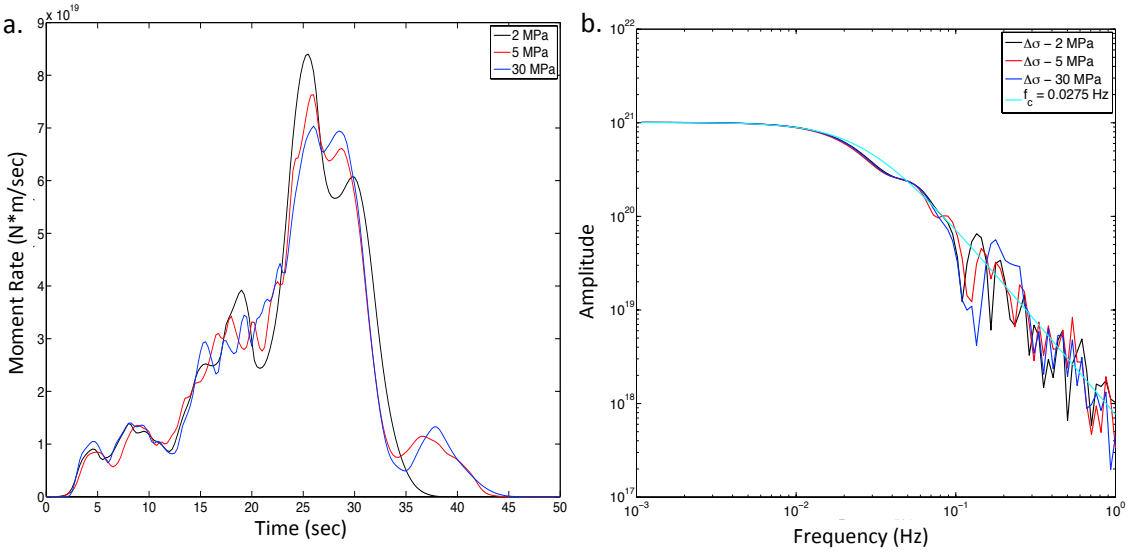

Figure 7: (a) Comparison of the cumulative moment rate functions of three selected inverted models with $\overline{\Delta\tau_E}$ equal to 2, 5 and 30 MPa, respectively. (b) Comparison of the Fourier spectra of the three models shown in (a), accompanied by the spectrum of a ω^2 model with corner frequency of 0.0275 Hz as reference.

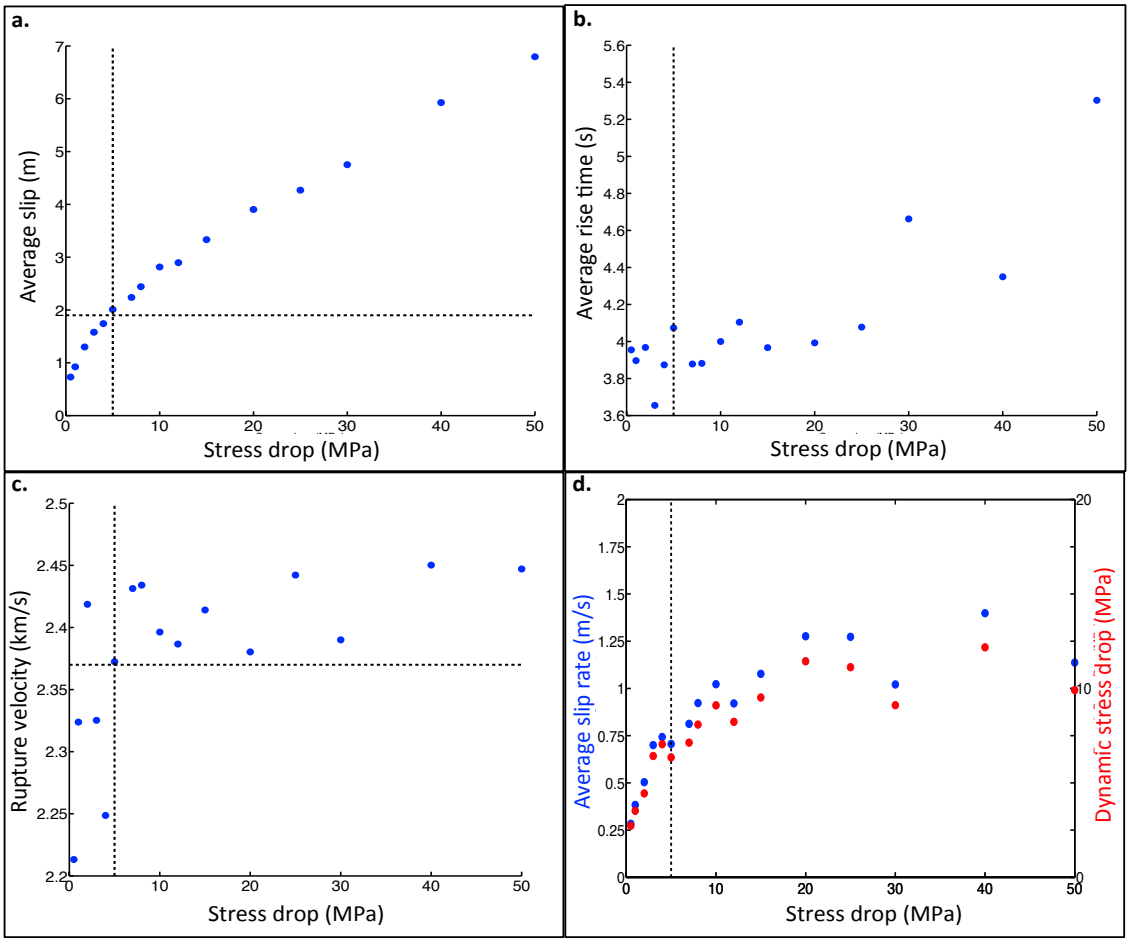

Figure 8: Variation of weighted average slip (a), weighted average rise time (b), weighted average rupture velocity (c), and weighted average slip rate (d) with $\overline{\Delta\tau_E}$. The vertical dashed lines mark $\overline{\Delta\tau_E}$=5MPa. See text for details.

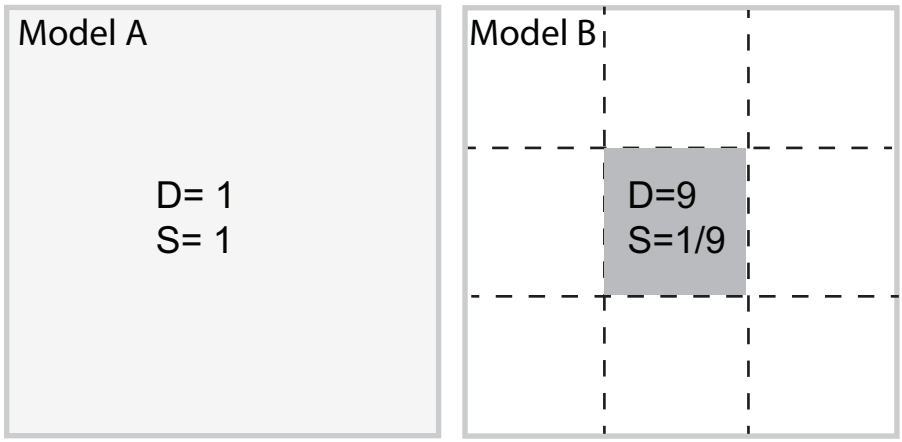

Figure 9: A cartoon illustrating the potential uncertainty of the estimate of the average stress drop due to limited spatial resolution. Two models, A and B, are embedded in a homogeneous medium. Model A has unit slip (D=1) on a square fault patch with unit area (S=1). Model B has all of its slip concentrated in a small square patch (the shaded grey area) with an area of 1/9, but the uniform slip in this grey patch is 9. Note that the two models (A and B) have the same seismic moment but the stress drop of model B is 27 times that of model A.

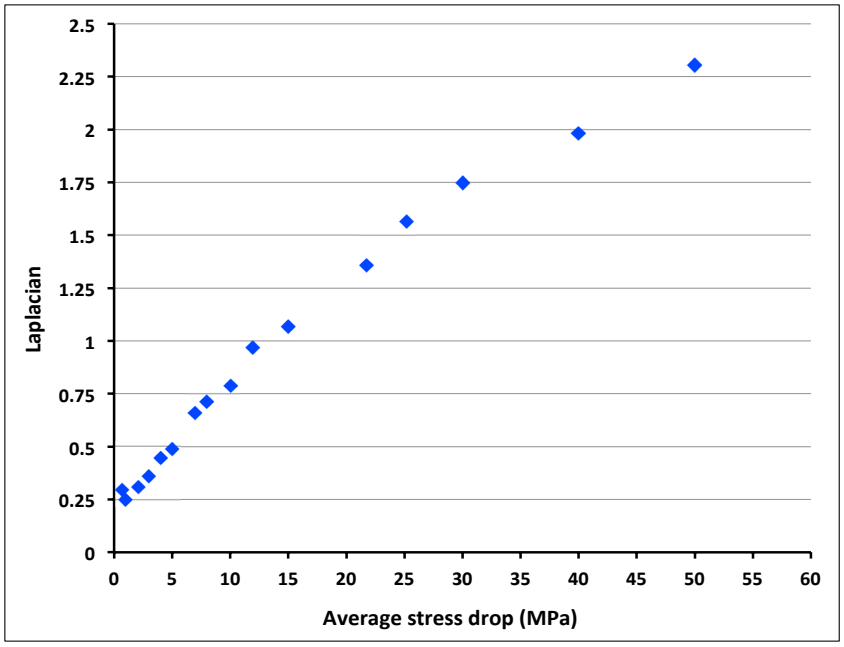

Figure 10: Variation of $\overline{\Delta\tau_E}$ with the fault roughness defined using the summation of the Laplacian of the corresponding inverted fault slip at all subfaults.

2.9 Appendix

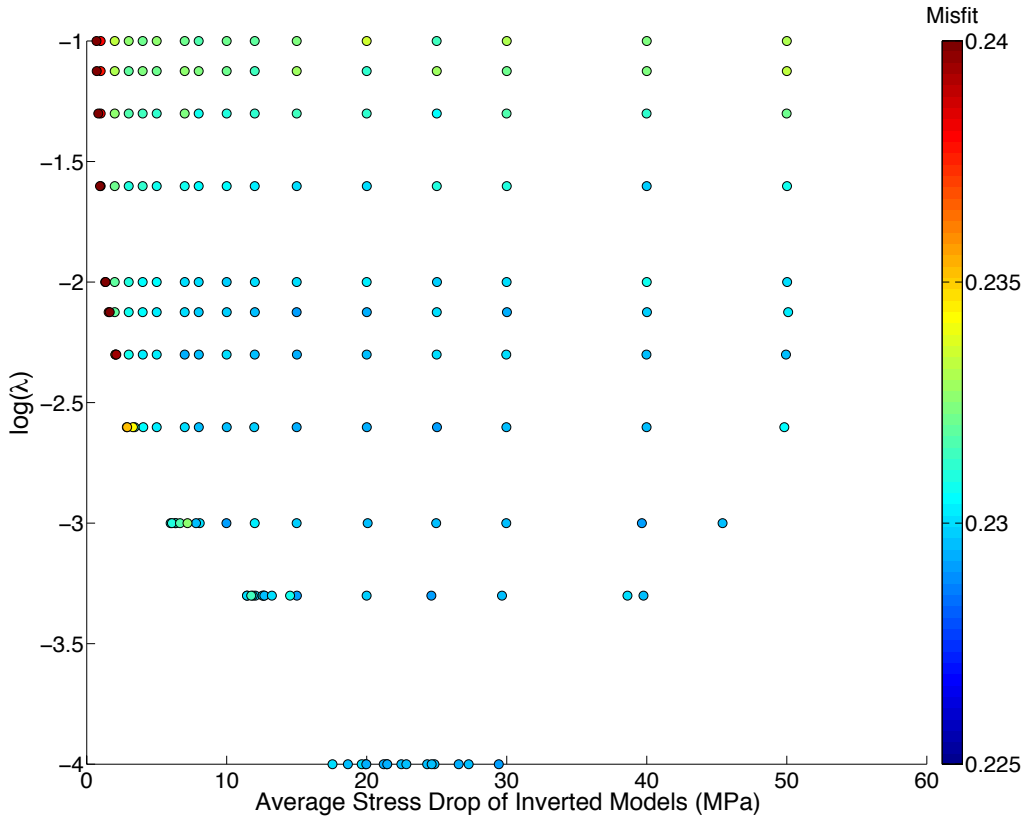

Figure S1: Variation of the waveform misfits of 176 inverted models with average stress drop ($\overline{\Delta\tau_E}$) and stress coefficient, λ_τ. Each circle denotes one inverted model with the color showing the value of the corresponding waveform misfit. As mentioned in the main text, we let the target stress drop change from 0.5 MPa to 50 MPa. However, when the target stress drop is small, for example 0.5 MPa, $\overline{\Delta\tau_E}$ of the inverted model might be significantly larger than the target. The respective waveform misfit colors each test, where high misfits are in red and low in blue. As the stress coefficient is increased the waveform misfit also increases, emphasizing the need to use the minimum λ_τ that still ensures the inversion converges to the target stress drop.

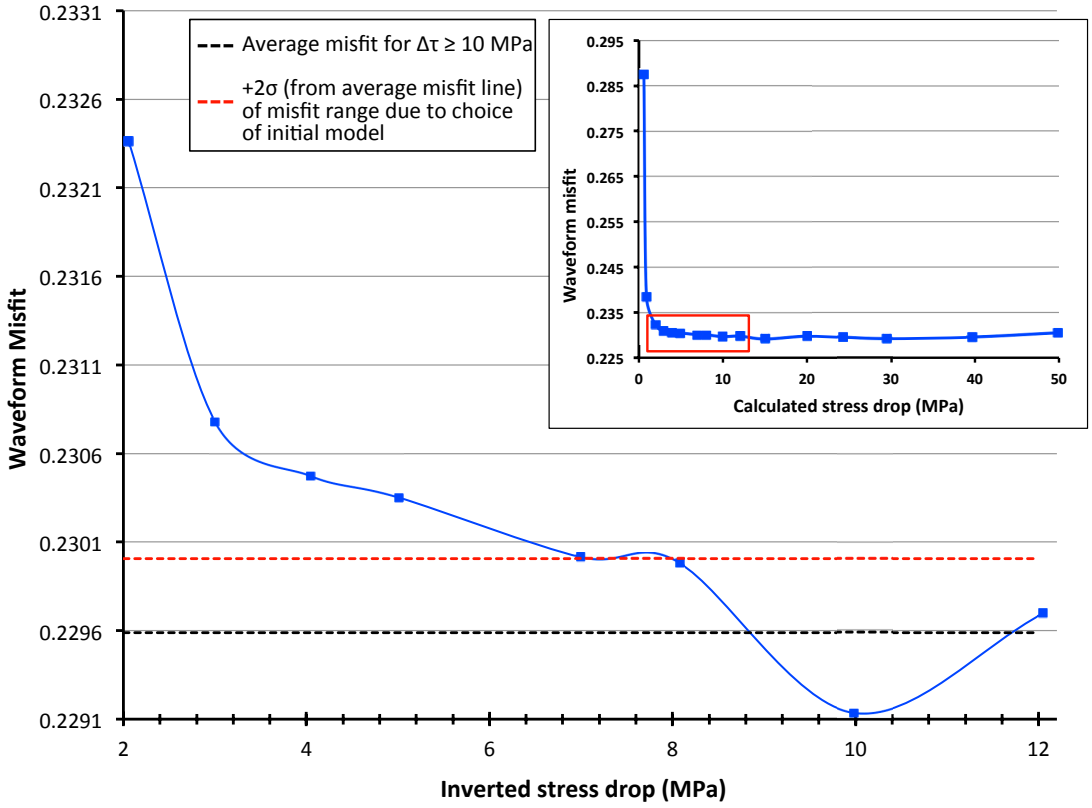

Figure S2: Variation of waveform misfit with $\overline{\Delta\tau_E}$. Upper-right inset shows the entire range of stress drops we have surveyed. Note that the waveform misfit is essentially constant when $\overline{\Delta\tau_E}$ is larger than 10 MPa. The red box highlights the stress range of 2-15 MPa, which is enlarged to be the main figure. The black dashed line denotes the average misfit for inverted models with $\overline{\Delta\tau_E}$ ≥10 MPa. The red dashed line further denotes this average line plus two times the standard deviation of the waveform misfit range due to the choice of the initial model.

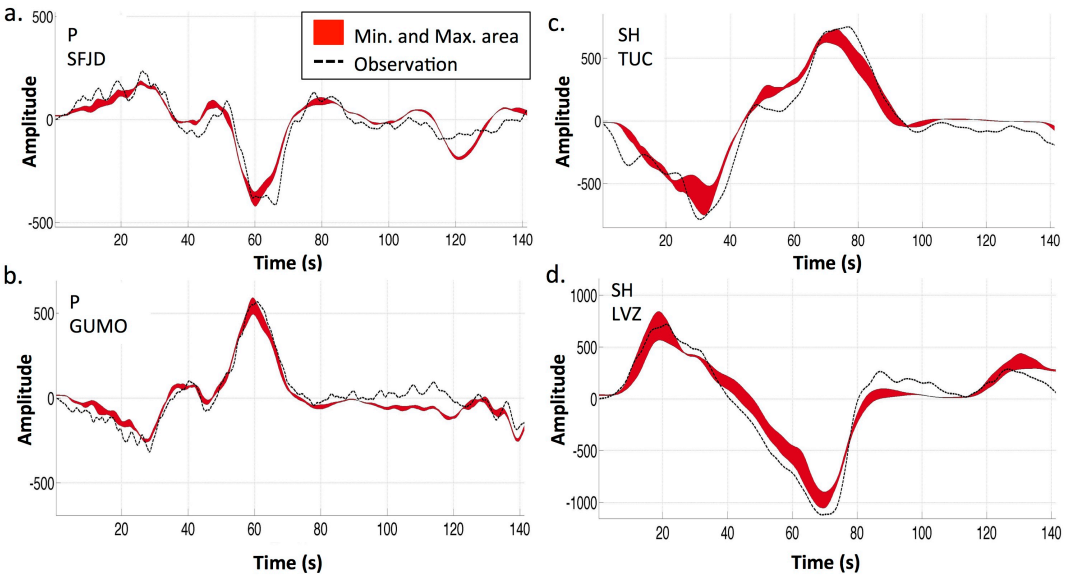

Figure S3: Comparison of P and SH synthetic ground displacement seismograms at select stations. The red area shows the range of synthetic displacement predicted using the inverted fault models with $\overline{\Delta\tau_E}$ ranging from 0.5 to 4 MPa. The observation is plotted as the black dashed line for comparison. The unit of vertical axis is μm.

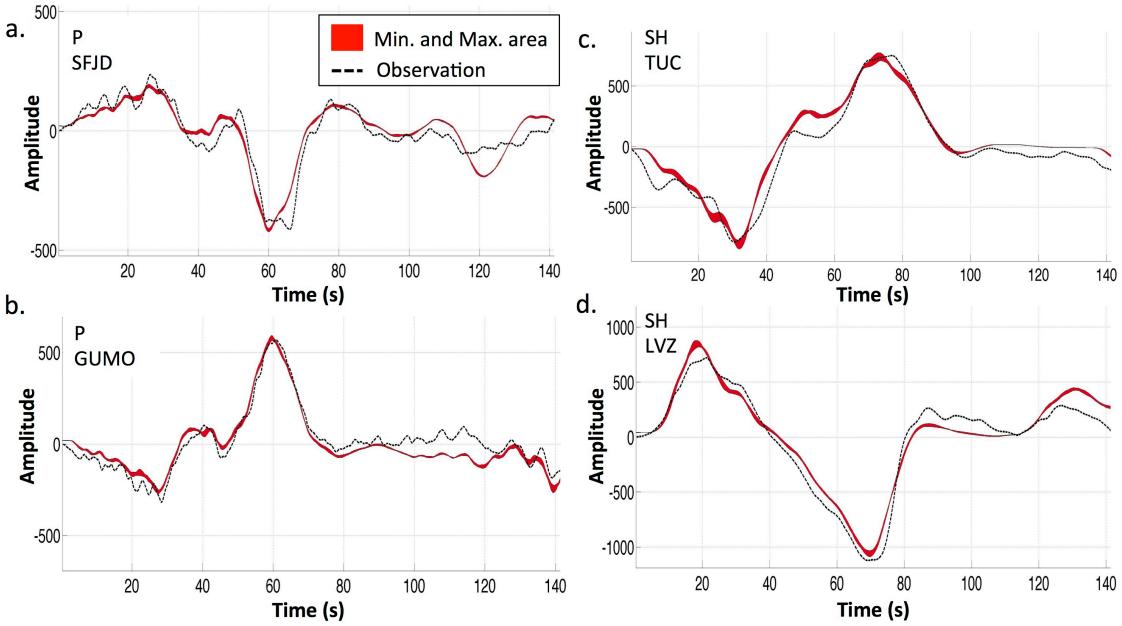

Figure S4: Similar to Figure S3 but here the red area shows the range of synthetic ground displacement waveforms predicted using the inverted fault models with $\overline{\Delta\tau_E}$ ranging from 5 to 50 MPa.

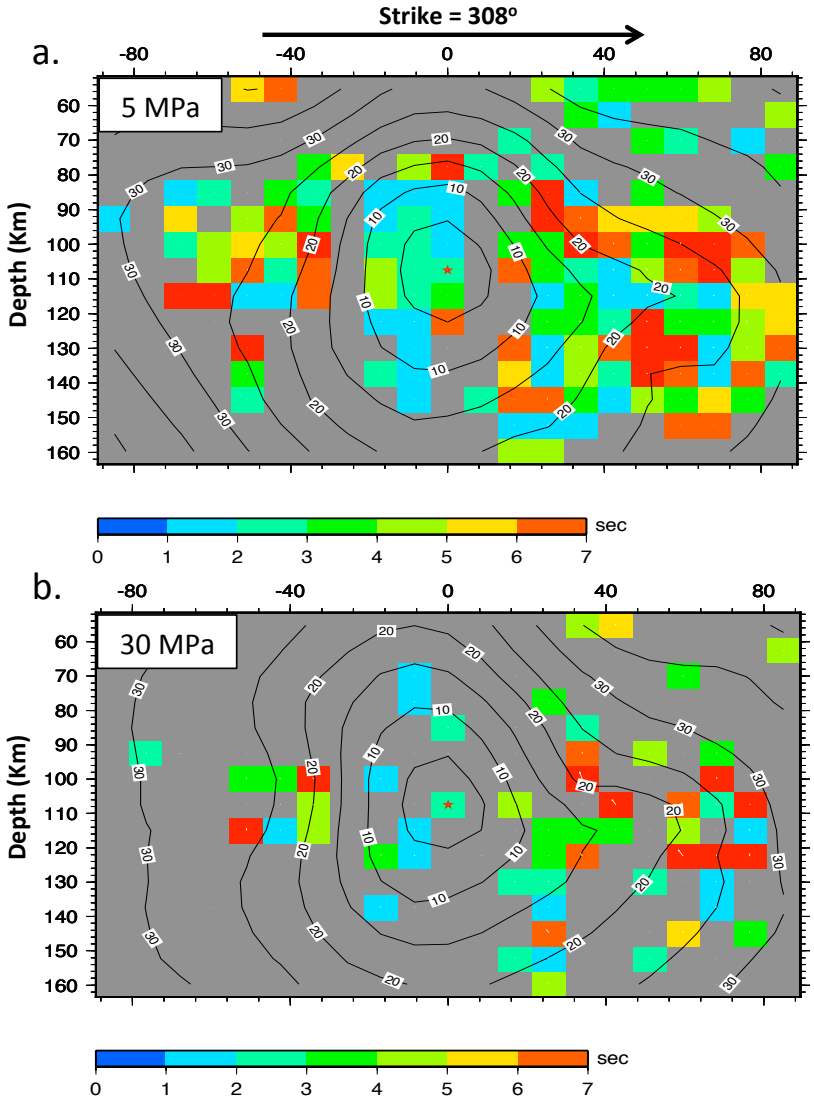

Figure S5: Distribution of the rise time (sec) for selected slip models with $\overline{\Delta\tau_E}$ equal to a) 5 MPa, and b) 30 MPa. Color denotes the rise time values of the subfaults with significant slip (> 10% of inverted peak slip). The corresponding slip and stress distributions are shown in Figure 7.

Parameter	Search Range
Slip (m)	0 – 15
Rake Angle (^{o})	215 – 275
Rupture Velocity (km/sec)	1.5 – 4.5
Rise Time (sec)	1.0 – 8.0

Table S1: Search range for inverted parameters.

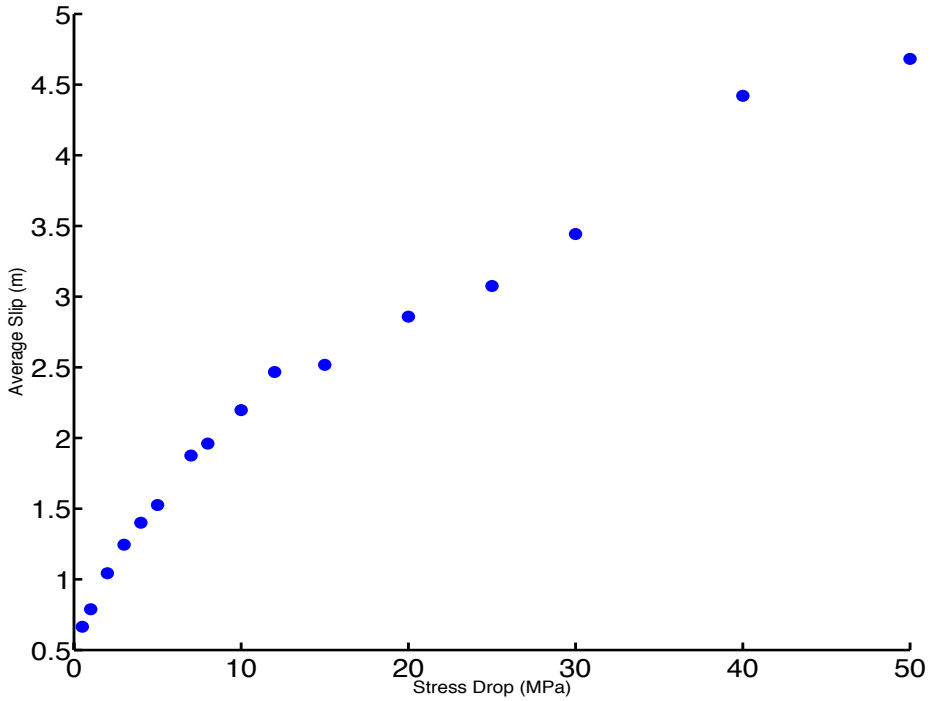

Figure S6: Average slip (m) for all inversions calculated using the simple definition:

$$\overline{D}_{simple} = \frac{1}{n}\sum_{i=1}^{n} D_i \qquad (s1)$$

where D_i is the slip at the i^{th} subfault, and n is the number of subfaults with slip greater than 10% of the peak slip. The average slip increases monotonously with average stress drop from 0.66 m to 4.68 m (a factor of ~7).

	Simple Average Slip (m)	Weighted Average Slip (m)	Peak Slip (m)
Model-5MPa	1.53	2.01	3.97
Model-5MPa A	0.97	1.21	1.86
Model-5MPa B	1.92	2.51	3.97
Model-5MPa C	0.92	1.25	2.38
Model-30MPa	3.44	4.75	14.39
Model-30MPa A	1.55	1.96	3.43
Model-30MPa B1	3.98	7.27	14.39
Model-30MPa B2	3.97	6.06	14.36
Model-30MPa C	1.42	5.77	4.78

Table S2: The average slip values for the two test cases shown in Figure 6, Model-5MPa and Model-30MPa, calculated using the simple and weighted average slip formulae. Also, the simple and weighted average slip for each main asperity for each of the two test cases, as labeled in Figure 6, is given. Finally, the peak slip (m) for each model as a whole, and for each asperity, is also shown. The weighted average slip is given by equation 7(a), and the simple average slip is given by equation (s1).

3. Energy based average stress drop and its uncertainty during the 2015 Mw 7.8 Nepal earthquake constrained by geodetic data and its implications to earthquake dynamics

This paper has been submitted to *Geophysical Journal International*, and has been accepted with minor revisions.

3.1 Abstract

The slip and static stress drop of the 2015 M_w 7.8 Gorkha, Nepal earthquake has been studied using its excellent near-source static observations and a newly developed finite fault inversion algorithm with an average stress drop constraint. A series of non-linear inversions with different target stress drops are conducted to search for the solution that not only most accurately fits the geodetic data, but also has an energy based stress drop, $\overline{\Delta\tau_E}$, matching the target value. Our result reveals that the misfit to the geodetic data gradually decreases when the $\overline{\Delta\tau_E}$ of the inverted slip model increases from 2 to 7 MPa; but becomes nearly constant when $\overline{\Delta\tau_E}$ further increases. Hence, only the lower bound of $\overline{\Delta\tau_E}$, i.e. $\overline{\Delta\tau_E}^{min}$(~7MPa), of the Gorkha earthquake can be constrained with near fault geodetic measurements, consistent with our previous study using just far field seismic data. The upper bound of $\overline{\Delta\tau_E}$ can be constrained with an extra constraint on the maximum local stress drop. An artificial upper bound can also be reached if using a large subfault size to represent the source. The lower bound of $\overline{\Delta\tau_E}$ leads to the lower bound of the apparent available energy and the upper bound of the radiation efficiency (η_R, 0.09-0.15), though the latter is also sensitive to the determination of the radiated seismic energy. We find that the lower η_R and the reported high rupture velocity (80-93% shear wave speed) can be reconciled by considering the aspect ratio of the dominant slip patch. We recommend using $\overline{\Delta\tau_E}^{min}$ to replace various slip smoothing constraints to stabilize the finite fault inversion because of its clear physical meaning.

3.2 Introduction

Accurate images of the growth of slip and faulting are critical in understanding the physics of earthquakes, and subsequently aid in the prediction of the ground motion that could be expected from future rupture events. However, the constraints of geophysical surface observations, such as seismic and geodetic measurements, to the underground earthquake rupture processes are generally limited, leading to non-unique solutions (e.g., Beresnev, 2003; Razafindrakoto et al., 2015). It is common practice for geophysicists to reduce the non-uniqueness of the inverse process by restricting the complexity of the target earth system. Two principal approaches have been widely adopted in earthquake source studies. First, by aiming to understand the average parameters of earthquakes, researchers only attempt to constrain a few inverted parameters by directly assuming a simple rupture scenario. The results of such analyses are mathematically over-determined but come with significant inherent uncertainties caused by simple source parameterization (e.g., Adams et al., 2017). For example, by assuming the earthquake as the rupture of a circular crack with constant rupture velocity, its average stress drop can be estimated based on only the corner frequency of recorded spectra and the seismic moment (Brune, 1970; Madariaga, 1979; Kaneko & Shearer, 2014):

$$\overline{\Delta\tau}_B = cM_0 f_c^3 \qquad (1)$$

where M_0 is the seismic moment, f_c is the corner frequency, and c is a constant dependent on the rupture speed.

Second, in order to explore the evolution of slip on faults, the source process is parameterized to be as realistic as possible (e.g., Olson & Apsel, 1982; Hartzell & Helmberger, 1982; Ide et al., 1996; Ji et al., 2002). Hundreds of free parameters are often

used, despite the fact that not all of them are well constrained by the available observations. Consequently, regularizations, such as smoothing constraints applied to the fault slip, are implemented to stabilize the solutions. Thus, the uncertainties of individual parameters are often difficult to access because they are not only caused by the limited data, but also these regularizations. Different constraints inevitably result in differences in inverted slip model distributions (e.g., Hartzell et al., 1991), though the long-wavelength features tend to be well preserved.

Recently, we have started to explore the uncertainty of average fault parameters using a realistic source representation. These parameters, such as average stress drop, can also be estimated using inverted slip models. In fact, previous analyses using published slip models yield significantly smaller deviations from the expected value of the average stress drop than the spectrum approach as mentioned above (Causse et al., 2014). However, it is not clear whether these results are caused by the use of more realistic fault parameterizations, or simply due to the regularizations used to smooth the inverted fault slip. To answer this question, in our companion work (Adams et al., 2017), we developed a new finite fault inversion strategy to explore the uncertainty range for the energy based average stress drop ($\overline{\Delta\tau}_E$) of large earthquakes, which is defined as

$$\overline{\Delta\tau}_E = \frac{\int_A \Delta\tau D dA}{\int_A D dA} \qquad (2)$$

where D and $\Delta\tau$ is on-fault static slip and stress drop, respectively (e.g., Kanamori & Allen, 1986; Kikuchi & Fukao, 1988; Shao et al., 2012; Noda et al., 2013). Noda et al. (2013) named $\overline{\Delta\tau}_E$ the energy based average stress drop because it is equivalent to twice

the ratio of the "apparent" available strain energy ($\Delta W_0 = \frac{1}{2}\int_A \Delta\tau D \mathrm{dA}$; Kanamori & Rivera, 2006) to the total seismic potency ($\int_A DdA$; Heaton & Heaton, 1989). For a given rupture event, such as the 2014 Mw 7.9 Rat Islands earthquake (Twardzik & Ji, 2015), a series of modified finite fault inversions are conducted to search for the solution that not only fits seismic and geodetic data, but also has a $\overline{\Delta\tau}_E$ matching a given value. This procedure results in a trade-off curve between $\overline{\Delta\tau}_E$ and the misfit to the observations, allowing us to explore the range of $\overline{\Delta\tau}_E$ constrained by a given geophysical dataset to be robustly defined. The application of this inversion strategy revealed that only the lower bound of $\overline{\Delta\tau}_E$, hereafter referred to as $\overline{\Delta\tau}_E^{\,min}$, could be constrained with far field seismic data (Adams et al., 2017). Unlike the temporal kinematic rupture process, the static stress drop of an earthquake can, in principle, be constrained with only geodetic observations. Here we will demonstrate that the same arguments hold for the source slip inversion using only near-field static data.

As mentioned above, various regulations have to be applied to finite fault studies to stabilize the inversions. These regulations inevitably affect the inverted solutions but how to appropriately select them is a challenging task for source modelers. For instance, slip-smoothing constraints are used in most inversion algorithms (e.g. Hartzell & Heaton, 1983), though there is no reason that fault slip necessarily needs to be smooth. Subsequently, the true target of these finite fault inversion algorithms becomes "*the most spatially smooth slip model that still explains the observations well*". The definition of the slip model roughness, which is concurrently minimized during the inversions, is, however, not unique. Hartzell & Heaton (1983) favored a simple smoothing scheme, i.e.,

$D_i - D_j \cong 0$, where D_i and D_j are the slip on adjacent subfaults. Du et al. (1992) defined the fault roughness as the Laplacian of the inverted slip distribution along the fault surface. If the finite fault inversion is carried out with the singular value decomposition (SVD) method, the smoothing of the fault slip might also be achieved by properly truncating the small eigenvalues (e.g., Hartzell & Heaton, 1983). These methods impact the inverted slip distribution differently (Adams et al., 2017), and there is no physical reason to select one approach over the others.

Adams et al., (2017) noticed the good correlation between the Laplacian of the slip distribution and energy based average stress drop $\overline{\Delta\tau_E}$, and suggested that the $\overline{\Delta\tau_E}^{min}$ can be used as an alternative way to smooth the fault slip. Unlike the constraints mentioned above, this regulation, which we name as "*minimum average stress drop*" constraint, has a clear physical meaning. Because of the aforementioned relationship in equation (2), and the fact that the seismic potency of a large earthquake can often be well constrained, searching for the lower bound of $\overline{\Delta\tau_E}$ is equivilant to searching for the lower bound of the available energy (ΔW_0) of this earthquake. In other words, we can replace the previous target of finite fault inversions, the smoothest slip distribution that can explain the observations well, with a more physical and well defined new target: the slip model with the lowest available energy that can explain the observations well.

The ability to estimate the lower bound of the available energy is important in studying the physics of the source process. For example, a lower bound for the available energy infers an upper bound for the seismic radiation efficiency (η_R), which is defined as the

ratio of the radiated seismic energy to the available energy, $\eta_R = \frac{E_R}{\Delta W_0}$ (e.g. Husseini, 1977; Venkataraman & Kanamori, 2004). Husseini (1977) and Venkataraman & Kanamori (2004) showed that η_R is positively correlated with the average rupture velocity. Thus, a rupture with a small radiation efficieny implies more energy is dissipated as fracture energy to create the rupture plane. Ye et al. (2016) systematically analyzed 110 M_w>7 earthquakes in the world and reported the average value of η_R to be 0.34 (logarithmic) or 0.49 (linear).

Here we study the slip distribution and static stress drop of the 2015 M_w7.8 Gorkha, Nepal earthquake, which has some of the best near-field geodetic observations for earthquakes with similar or larger magnitudes (e.g., Yue et al., 2016; Mcnamara et al., 2016; Lindsey et al., 2015, Wang & Fialko, 2015). The Gorkha earthquake has previously been extensively studied with seismic and geodetic data individually or combined together (e.g., Avouac et al., 2015; Lindsey et al., 2015; Mcnamara et al., 2016; Yue et al., 2016; Denolle et al., 2016; Lay et al., 2016). These studies revealed that this earthquake has a fast average rupture velocity, varying from 2.8 to 3.2 km/s (Avouac et al., 2015; Fan & Shearer, 2015; Zhang et al., 2016), 83-92% of the shear wave speed (3.5 km/s) in the depth of coseismic rupture. In this study, we will first explore the lower and upper bounds of $\overline{\Delta\tau_E}$ during the 2015 Nepal earthquake that are consistent with this excellent near-field static data. Second, a classic L-curve method is introduced to quantitatively define the lower bound of $\overline{\Delta\tau_E}$, i.e., $\overline{\Delta\tau_E}^{min}$. The lower bound of $\overline{\Delta\tau_E}$ leads to the upper bound of the radiation efficiency, i.e., $\eta_R{}^{max}$, which is in fact much smaller than the previous reported mean values of global large earthquakes (Ye et al., 2016). We

subsequently show that the low η_R and the high rupture velocity can be reconciled by considering the shape of the slip patch. In the end, we recommend using $\overline{\Delta\tau_E}^{min}$ to replace various slip smoothing constraints in order to stabilize the finite fault inversion.

3.3 Tectonic Background and Observations

The April 25th, 2015 M_W 7.8 Gorkha earthquake occurred at 06:11:25 (UTC) on the Main Himalayan thrust (MHT) as a result of thrust faulting on or near the main thrust interface between the subducting India plate and the overriding Eurasia plate (Avouac et al., 2015) (Figure 1). Previous geodetic studies revealed that the MHT is the primary fault interface accommodating 20 mm/yr of convergence between these two plates (Avouac, 2003; Larson et al., 1999; Molnar, 1988). Using interseismic GPS observations, Ader et al., (2012) concluded that the MHT is locked from the surface to approximately 20 km depth. The segment of the MHT where the Gorkha earthquake occurred previously ruptured in 1833, with a rupture length of 100 km (Bilham et al., 2001), comparable to the 2015 Gorkha earthquake.

We use co-seismic geodetic data distributed to the public domain in this analysis. The unwrapped InSAR data was downloaded from http://topex.ucsd.edu/nepal/, which counts the LOS (line-of-sight) surface deformation between 02/22/2015 and 05/03/2015 measured by Advanced Land Observing Satellite 2 (ALOS-2, operated by Japanese Aerospace Exploration Agency) (Lindsey et al., 2015). The data has been subsampled to 678 points using the QuadTree resampling method (Lohman & Simons, 2005). The co-seismic displacements at four near-fault GPS stations deployed by the Caltech Tectonics

Observatory (e.g., Avouac et al., 2015) were processed by Advanced Rapid Imaging and Analysis Center for Natural Hazards at Jet Propulsion Laboratory (JPL) using GIPSY-OASIS software (Galetzka et al., 2015). Figure 2a illustrates the distribution of the LOS displacement measurements, with the locations of the InSAR and GPS points. The color maps the LOS displacements, which change from -70.9 to 107.6 cm. The southern end shows a larger and positive coseismic LOS offset compared to the northern region, and implies a greater uplift compared to the smaller subsidence in the north.

3.4 Method

Without loss of generality, assume that the rupture of the earthquake occurs on a rectangular fault plane, that is then divided into N (along-strike) by M (down-dip) subfaults. Let (j, k) denote the position of an arbitrary subfault, where j = 1, 2, …, N, and k = 1, 2, …, M. $u(\vec{x})$ represents the static response of this earthquake at location $\vec{x}$, which can be calculated by adding the contributions of all subfaults (e.g., Olson & Apsel, 1982; Ji et al., 2002):

$$u(x) = \sum_{j=1}^{N} \sum_{k=1}^{M} D_{jk}\left[cos(\lambda_{jk}) Y_{jk}^{1}(\vec{x}) + sin(\lambda_{jk}) Y_{jk}^{2}(\vec{x})\right] \qquad (3)$$

Where D_{jk} and λ_{jk} are the dislocation amplitude and rake angle respectively. Y_{jk}^{1} and Y_{jk}^{2} are the subfault Green's functions for unit slip in the strike and down-dip direction, respectively. Ordinarily, during the finite fault inversion with geodetic data, the fault model $\boldsymbol{m}$, described by D_{jk} and λ_{jk}, is determined by minimizing the difference between the synthetic and observed static displacements.

The shear stress drop at the center of the (*i, j*) subfault can be calculated by:

$$\tau_{ij}^{r}(m) = \sum_{k=1}^{N}\sum_{l=1}^{M}\left[D_{kl}^{1}(m)\sigma_{ij,kl}^{r,1} + D_{kl}^{2}(m)\sigma_{ij,kl}^{r,2}\right] \quad (4)$$

where $\tau_{ij}^{r}(m)$; for *r = 1,2* denotes the left-lateral (*r = 1*) or thrust shear (*r = 2*) stress at this location, respectively, for a given model ***m***, and $D_{kl}^{p}(m)$, for *p = 1,2*, is the corresponding left-lateral (*p = 1*) or thrust (*p = 2*) displacements at the (*k,l*) subfault. Various synthetic algorithms (e.g. Okada, 1992; Cotton & Campillo, 1995) can then be used to pre-calculate a kernel function, $\sigma_{ij,kl}^{r,p}$, that represents the shear stress response at the center of subfault (*i,j*) caused by the unit slip on subfault *(k,l)*. Thus, the energy based average stress drop (e.g., Shao et al., 2012; Noda et al., 2013) of a model ***m*** can be calculated as:

$$\overline{\Delta\tau_E}(m) = \frac{\sum_{i=1}^{N}\sum_{j=1}^{M}\tau_{ij}(m)\cdot D_{ij}(m)}{\left|\sum_{i=1}^{N}\sum_{j=1}^{M}D_{ij}(m)\right|} \quad (5)$$

where $\tau_{ij}(m)$ is the stress drop at the center of the (*i,j*) subfault, as the response to the fault slip of model *m*. As suggested by Noda et al. (2013), when the components of stress drop and slip in the overall slip direction dominate, τ_{ij} and D_{ij} in equation (5) can be approximated as their components in the overall slip direction. This approximation is used in this study.

Following Adams et al. (2017), we evaluate the slip model (***m***) using the objective function *E(**m**)* defined as:

$$E(m) = E_{fit} + \lambda_1 E_{moment} + \lambda_\tau \left| ln\left(\frac{\overline{\Delta\tau}_E(m)}{\tau_{target}}\right)\right| \quad (6)$$

In this study, we simply define $E_{fit}(m)$ as the root mean square (RMS) of the difference between the observed and synthetic static displacements. E_{moment} is a function of the discrepancy between the inverted seismic moment and the value based on other methods, such as the GCMT solution. The weight λ_1 is fixed at 0.1 in this study for all inversions. However as we discuss later, changing this to a negligible value (10^{-4}) does not affect our conclusions. Finally, the last term is called the "fixed average stress drop constraint", and it is zero when the $\overline{\Delta\tau}_E(m)$ of the inverted slip model $\boldsymbol{m}$ is equal to the pre-assigned τ_{target}. The logarithm function is selected here to limit the range of variation due to different $\overline{\Delta\tau}_E(m)$. Note that as $\overline{\Delta\tau}_E(m)$ approaches τ_{target}, $\left|ln\left(\frac{\overline{\Delta\tau}_E(m)}{\tau_{target}}\right)\right|$ converges to zero as $\frac{|\overline{\Delta\tau}_E(m)-\tau_{target}|}{\tau_{target}}$. λ_τ is the coefficient balancing the effects of E_{fit}(m) and the "fixed average stress drop constraint". It can be selected using a grid search approach (Adams et al., 2017).

During this study, we let τ_{target} vary within a large range and a simulated annealing algorithm (Ji et al., 2002a) is used to search for the minimum of $E(m)$ for each given τ_{target} (Adams et al., 2017).

3.5 Fault Geometry and velocity structure

We approximate the fault with a single rectangular fault plane inferred from the GCMT solution (http://www.globalcmt.org), the USGS epicenter (28.231°N, 84.731°E) and a slightly shallow hypocenter depth of 12 km. It is oriented with a strike of 293° and dips 7° to the north. Similar fault geometry is also used in previous studies (e.g., Yue et al, 2016).

After some preliminary tests, the final fault plane used in this study extends 176 km along-strike and 80 km down-dip, spanning a depth range of 8.3 to 18.1 km. The fault plane is divided into 880 subfaults measuring 4.0 km (along-strike) and 4.0 km (down-dip). The fault slip and rake angle of each subevent are inverted, leading to a total of 1760 free parameters. To test the impact of the subfault size, we also conduct inversions using a subfault size of 8 km by 8 km, resulting in a total of 440 free parameters. It is important to recognize that the 4x4 km subfault case is under-determined as we have fewer data points (678) than free parameters, whereas the 8x8 km case is not. During the inversion, the slip on individual subfaults is allowed to change from 0.0 to 15 m, and the rake angle is allowed to vary from 80^o to 140^o. We also limit the slip at the edges of the fault plane to less than 0.01 m.

We use a one-dimensional layered velocity model (Figure 3) interpolated from the Global CRUST 2.0 model (Bassin et al., 2000), to approximate the earth structure in the source region. It is important to note that from a depth of 0.6 to 21.5 km, which encompasses the depth region of coseismic rupture, the S wave speed is 3.5 km/s, according to this model. The corresponding rigidity is then 3.31×10^4 MPa. While the surface static displacements of the layered structure are computed using the method of Xie and Yao (1989), the constant velocity and density in the source depth range allow us to quickly calculate the on-fault stress change using the analytic solution for a half-space earth (Okada, 1992).

3.6 Results

We have conducted three sets of inversions to explore the upper and lower bounds of $\overline{\Delta\tau_E}$ and the potential uncertainties associated with subfault size and the maximum local stress

drop. We will first investigate the results using 4 km by 4 km subfaults and then discuss the uncertainties.

3.6.1 $\overline{\Delta\tau_E}^{min}$ of the 2015 Gorkha earthquake

We have conducted inversions with 22 different target stress drops (τ_{target}) ranging from 2 to 50 MPa. The subfault size of all fault models is 4 km by 4 km. Inversions are allowed a variety of different initial models, but the number of iterations is fixed to 400 after preliminary tests. For each τ_{target}, we conduct multiple inversions with the coefficient λ_τ gradually **i**ncreasing from a negligible value of 10^{-4} until 0.1, and select the model with the smallest λ_τ value that still could guarantee the difference between $\overline{\Delta\tau_E}$ of the inverted model and τ_{target} to be less than 10% (Adams et al., 2017). Figure 4 shows the relationship between $\overline{\Delta\tau_E}$ of the inverted models and the value of the corresponding misfit function E_{fit}. It can be seen that E_{fit} generally decreases quickly as $\overline{\Delta\tau_E}$ increases from 2 MPa to 7 MPa, and then remains essentially constant when $\overline{\Delta\tau_E}$ increases from 7 MPa to 50 MPa, albeit with small fluctuations. The pattern is identical to our previous work using teleseismic data (Adams et al., 2017).

In principle the simulated annealing algorithm should be independent of the initial models, but in practice, because of the limitations such as a fixed maximum iteration number, small dependences are often observed. We conduct 10 additional inversions with different initial models for the same τ_{target} of 7 MPa. The E_{fit} values of these models have a mean of 2.694 cm and a standard deviation (σ) of 0.011. The two red dashed lines in Figure 4a define the $\pm 2\sigma$ misfit range due to the choice of the initial model. Note that

all E_{fit} values of models with $\Delta\tau_E$>7 MPa fall within this range. Hence, this excellent geodetic dataset allows us to define the lower bound of $\overline{\Delta\tau_E}$ but fails to constrain its upper bound, similar to our previous conclusion using teleseismic data (Adams et al., 2017).

All inverted models with $\overline{\Delta\tau_E} \geq 7\ MPa$ explain the data well. Figure 2c shows the distribution of the residuals (observed-synthetics) of the worst scenario, i.e., the solution with $\overline{\Delta\tau_E} = 7\ MPa$. The misfits for the majority of the InSAR points across the actual fault plane are near zero. However, relatively large discrepancies are found in the points far to the south and near the bottom left-hand corner of the assigned fault plane. As large misfits for measurements in similar regions can also be seen in other studies, the misfits are likely caused by errors unrelated to the coseismic rupture.

The exact lower bound of $\overline{\Delta\tau_E}$, or $\overline{\Delta\tau_E}^{min}$, depends on the errors and limitations of observations, the synthetic earth response, and the inversion procedure. If only considering the error caused by the choice of the initial model, we might argue that, with 95% confidence, the $\overline{\Delta\tau_E}$ of 2015 Nepal earthquake is about 7 MPa (upper red dashed line, Figure 4a (Adams et al., 2017). Alternatively, Adams et al. (2017) found that the $\overline{\Delta\tau_E}$ of the inverted model changes monotonically with the roughness of the inverted slip model measured as the Laplacian of fault slip. One of the classic methods that is widely used to deal with the trade-off between data misfit and the roughness of the inverted slip model is the L-curve method (e.g., Hansen & O'Leary, 1993; Mendoza & Hartzell, 2013). We adopt it here to deal with the balance between $\overline{\Delta\tau_E}$ and E_{fit}. Analogously,

$\overline{\Delta\tau_E}^{min}$ is defined as the "corner" or the point with the maximum curvature of the log($\overline{\Delta\tau_E}$)–log(E_{fit}) plot. Following Hansen & O'Leary (1993), a local smoothing polynomial function is applied before a 2D spline curve is used to fit the set of points that make up the L-curve: which are the average stress drops of the model and their respective inversion misfit values. Then, the point of maximum curvature on this spline curve is computed and the "corner" becomes the data point closest to this calculated point. After applying this algorithm, the corner, i.e. the lower bound, of the misfit versus stress drop curve is at 7 MPa (Figure 5a), which is consistent with our earlier results.

As pointed out by Adams et al. (2016), there is a positive correlation between $\overline{\Delta\tau_E}$ and the fault roughness defined using the Laplacian of the inverted slip distribution. For a comparison, in Figure 5b we show the RMS misfit and fault roughness of every model used in Figure 5a. The two dashed lines denote the values of these two parameters associated with the model with $\overline{\Delta\tau_E}^{min}$, respectively. Visually these models also fall in a L-shape curve and the location of the model with $\overline{\Delta\tau_E}^{min}$ is near the point of maximum curvature of this inferred L-shape curve (Figure 5b). Hence, even using the slip roughness as a constraint, the model with $\overline{\Delta\tau_E}^{min}$ is still one of its optimal solutions. This similarity implies that the solutions using conventional finite fault methods will have a similar $\overline{\Delta\tau_E}$ that is close to $\overline{\Delta\tau_E}^{min}$ if all of them use similar datasets. This is consistent with the previous analysis of the published slip models (Causse et al., 2014).

Figure 6a shows the slip distributions of the models with $\overline{\Delta\tau_E} = \overline{\Delta\tau_E}^{min}$, hereafter referred to as "M_{eb}-7MPa". It has a cumulative seismic moment of 7.55x10^{20} Nm (M_w

7.8). The inverted peak slip is 8.67 m. The weighted average fault slip amplitude $\overline{D}$, defined as $\overline{D} = \frac{\sum_j \sum_k D_{jk}^2}{\sum_j \sum_k D_{jk}}$, where D_{jk} is the slip amplitude of subfault *(j,k)* (Ji et al., 2002), is 4.3 m (Figure 7b). The slip distribution of this model is compact, as only 43% of all subfaults have significant slip, which is here defined as slip larger than 0.87 m, 10% of the peak slip. Most of the subfaults with significant slip are within the largest slip patch with an inverse triangular shape, which is outlined by the 10% peak slip contour in white (Figure 6a). Several small slip patches can also be seen at the edges of the fault plane, which are likely caused by errors in the observations.

According to the values of the objective function, all models with $\overline{\Delta\tau}_E \geq$7MPa cannot be distinguished simply by their fit to the observations (Figure 2a); all of them also have a similar seismic moment. Figure 6b shows the slip distribution of one such representative: the model with $\overline{\Delta\tau}_E$ equal to 20 MPa, which we will refer to as "M_{eb}-20MPa". Note that the edges of the asperities are again outlined using the same criterion as above, by contours of 10% of the peak slip. Comparing Figure 6a with 6b, we can see that as $\overline{\Delta\tau}_E$ increases, the fine scale roughness intensifies. The peak slip of M_{eb}-20MPa is ~15 m, and its weighted average fault slip $\overline{D}$ is 5.7 m, 25% larger than that of model M_{eb}-7MPa. On the other hand, the spatial extent and location of the main slip asperity remains relatively intact, despite the increased heterogeneity. For example, it can be seen that the shape of the large triangular asperity in model M_{eb}-20MPa spans nearly the same area as that of M_{eb}-7MPa (white contour line, Figures 6a and 6b). Figure 7a illustrates the difference between M_{eb}-7MPa and M_{eb}-20MPa. On the individual subfaults, the differences range from -5.85 to 9.32 m, which is notable considering the peak slip of model M_{eb}-7MPa is

only 8.67 m. The mean of the differences is 0.002 m and the standard deviation is 1.67 m. Over the main slip asperity, regions of the slip distributions of the two models generally differs in the range of -4 m to +4 m. Figure 7a then highlights the difficulty to constrain the slip of individual subfaults using available geodetic data. Then, as shown in Figure 7b, the weighted average fault slip $\overline{D}$ increases almost linearly from 4.3 m to 8.5 m as $\overline{\Delta\tau_E}$ increases from 7MPa to 50 MPa.

Figures 8a and 8b show the static stress drop distributions of M_{eb}-7MPa and M_{eb}-20MPa, respectively. The heterogeneity of the slip distributions is clearly reflected in the stress distributions, with the most variability in the model with the higher stress drop. The subfaults with the large stress drop are also correlated with the subfaults with high slip. The peak stress drop of M_{eb}-20MPa is about 2 times greater than that of M_{eb}-7MPa.

Furthermore, tests were conducted that relaxed the moment constraint, i.e. λ_1 was set to 0.0001 rather than 0.1, and the inverted seismic moment increased by 8% (6.98×10^{20} Nm versus 7.55×10^{20} Nm). The misfit value also decreased slightly from 2.71 to 2.69. The only noticeable difference was that when the moment constraint was less strict, the peak slip was slightly more: 9.3 m versus 8.7 m.

3.6.2 Can we constrain $\overline{\Delta\tau_E}^{max}$ of the 2015 Gorkha earthquake?

We have explored the possibility of constraining the maximum of $\overline{\Delta\tau_E}$ and found that under two circumstances E_{fit} will increase again when $\overline{\Delta\tau_E}$ becomes large enough. First, we find that the pattern of the E_{fit} vs. $\overline{\Delta\tau_E}$ curve shown in Figure 4a depends on the

subfault size. For comparison, we have repeated the above analysis with models using 8 km by 8 km subfaults, i.e. four times larger in area. The number of inverted free parameters is subsequently reduced by a factor of 4. As shown in Figure 4b, the value of the misfit function E_{fit} decreases quickly as $\overline{\Delta\tau_E}$ increases from 2 MPa and reaches the minimum when $\overline{\Delta\tau_E}$ equals 7-8 MPa, consistent with the above analyses using 4 km by 4 km subfaults. However, as expected the minimum value of E_{fit} is 3.395, larger than the analysis using 4 km by 4 km subfaults. When $\overline{\Delta\tau_E}$ further increases, the value of E_{fit} starts to increase as well, particularly when $\overline{\Delta\tau_E}$ exceeds 18 MPa (Figure 4b). Hence, when using large subfaults, the E_{fit} vs. $\overline{\Delta\tau_E}$ curve seems to suggest the upper bound of $\overline{\Delta\tau_E}$ can also be constrained using geodetic data. Note that using a larger subfault size limits the shortest wavelength of the spatial variation of slip allowed, and subsequently, the shortest wavelength of the local stress drop variation. Adams et al. (2017) pointed out that the difficulty to constrain the upper bound of the energy based average stress drop $\overline{\Delta\tau_E}$ is due to the difficulty to constrain the shortest wavelength of the local stress drop variation with surface data. Thus, this result with static data is an expected artifact.

Second, the above inversions with the fixed average stress drop constraint only have a weak sensitivity to the stress drop at individual subfaults. As shown in Figure 8a, the average stress drop is only 7 MPa but the maximum local stress drop is much higher at 46 MPa. We have attempted to further constrain the maximum local stress drop by adding one more term to the objective function $E(m)$:

$$E(m) = E_{fit} + \lambda_1 E_{moment} + \lambda_\tau \left| ln\left(\frac{\overline{\Delta\tau}_E(m)}{\tau_{target}}\right)\right| + \lambda_{\tau_{local}} E_{\tau_{local}} \qquad (7)$$

with

$$E_{\tau_{local}} = \sum_{ij} \begin{pmatrix} 0 & if\ \Delta\tau_{ij} < \Delta\tau_{max} \\ \left|\frac{\Delta\tau_{ij} - \Delta\tau_{max}}{\Delta\tau_{max}}\right| & if\ \Delta\tau_{ij} \geq \Delta\tau_{max} \end{pmatrix} \quad (8)$$

$\Delta\tau_{ij}$ denotes the stress drop at subfault *(i,j)* and $\Delta\tau_{max}$ is the pre-assigned maximum local stress drop. $\lambda_{\tau_{\mathrm{local}}}$ is the local stress coefficient, which is set to the minimum value possible while still ensuring $E_{\tau_{local}}$ is less than 0.1, i.e., the stress drop at any subfault cannot be 10% larger than the given $\Delta\tau_{max}$. We name this new physical regulation the "maximum local stress drop constraint". Figure 4c shows the $\overline{\Delta\tau_{\mathrm{E}}}$ vs. E_{fit} curve in blue after we set $\Delta\tau_{max}$ to 25 MPa, in comparison to the case without the maximum local stress drop constraint in red. It can be seen that the two curves are nearly overlapping when $\overline{\Delta\tau_E}$ is less than 15 MPa. However, E_{fit} starts to increase again as τ_{target} increases past ~15 MPa if $\Delta\tau_{max}$ is constrained to 25 MPa. While our final estimate of $\overline{\Delta\tau_E}^{min}$ still holds in this case ($\Delta\tau_{max} < 25\ MPa$), one can also expect it to be affected if a much smaller $\Delta\tau_{max}$, for example 7MPa, is chosen. While $\Delta\tau_{max}$ is unfortunately unknown, the 25 MPa assumed in this case is not abnormally high. It is less than one third of the maximum shear stress at a depth of 10-15 km, estimated with the empirical relationship proposed by McGarr (1999). Furthermore, Shao et al. (2012) reported that $\overline{\Delta\tau_E}$ and the peak stress drop of the 2009 Mw 5.4 Chino Hills earthquake are 38 MPa and 80 MPa, respectively, at a source depth of about 15 km.

Figures 6c and 6d show the inverted slip distributions using equations (7) and (8) as the objective function, with a τ_{target} of 7MPa and 20 MPa, respectively. We refer to them as "M_{ls}-7MPa" and "M_{ls}-20MPa", respectively. It can be seen that the constraint to the local

stress drop has negligible impact to the general shape of the slip asperities, which are similar to the first set of models (Figure 6a and 6b). The peak slips for these models are similar to the first two models at 8.8 and 10.4 m, respectively. Also, both M_{ls}-7MPa and M_{ls}-20MPa exhibit fewer patches of high slip, i.e. considering only the ruptured area, the asperity itself has a more homogeneous slip distribution, than M_{eb}-7MPa and M_{eb}-20 MPa, respectively. Overall, these four models do have similar slip extensions and the asperity boundary in all cases considered here are well constrained.

Regardless of the promise to constrain the upper bound of $\overline{\Delta\tau_E}$ with additional information of the maximum local stress drop $\Delta\tau_{max}$, readers should be aware that $\Delta\tau_{max}$ mentioned here is different than what has been found in the laboratory. The $\Delta\tau_{max}$ is the maximum stress drop across a fault length proportional to the subfault size, i.e., on the order of kilometers. In contrast, the rock units used in laboratory experiments are generally on the order of meters or less (e.g., Mclaskey et al., 2014). The $\Delta\tau_{max}$ should then be less than the maximum local stress drop found in laboratory experiments.

3.7 Discussion

Our previous study of the 2014 M_W 7.9 Rat Islands earthquake (Adams et al., 2017) revealed that using teleseismic waveforms, only the lower bound of $\overline{\Delta\tau_E}$ could be constrained. We interpreted it as a result of the limited resolution to the fine scale roughness of the fault slip. In this study, we reach the same conclusion for the 2015 M_W 7.8 Gorkha, Nepal earthquake with its excellent near-source geodetic observations. We further illustrate that the upper bound of $\overline{\Delta\tau_E}$ can be accessed only when the highest local

stress drop is known. Also, we must caution readers about the potential for a pseudo upper bound, caused by using too large a subfault size.

3.7.1 Preferred slip model of the 2015 Gorkha event and its uncertainty

All models with $\overline{\Delta\tau}_E > \overline{\Delta\tau}_E^{\,min}$ match the data indistinguishably. Considering the large differences amongst these models (e.g., Figure 7a), it is not meaningful to discuss the slip distributions without additional constraints to $\overline{\Delta\tau}_E$. As mentioned above, $\overline{\Delta\tau}_E$ is related to the "apparent" available strain energy (ΔW_0), i.e., $\Delta W_0 = \frac{1}{2}\overline{\Delta\tau}_E P$, where P denotes the seismic potency (Kanamori & Rivera, 2006). ΔW_0 is the portion of the total strain energy responsible for creating a new fault plane and radiating seismic waves. Since the seismic potency is often well constrained, the solution with $\overline{\Delta\tau}_E = \overline{\Delta\tau}_E^{\,min}$ is then the model with the minimum available strain energy ($\Delta W_0^{\,min}$) that also matches the data.

We have conducted 10 additional inversions with different initial models but with the same target stress drop of $\tau_{target} = \overline{\Delta\tau}_E^{\,min}$ (7 MPa). While what is shown in Figure 6a and Figure 8a can be viewed as one representative model, here Figure 9a and Figure 9b show the mean slip distribution of all of these slip models and the corresponding standard deviations for individual subfaults, respectively. We find that besides the similar seismic moment and $\overline{\Delta\tau}_E$, the weighted average slip, $\overline{D}$, defined above is also incredibly stable, changing negligibly from 4.30 to 4.41 m among these models. The variation of slip on individual subfaults is still notable but much smaller than what is shown in Figure 7a. The average standard deviation of slip is only 0.42 m (5% of the peak slip), though on

individual subfaults the standard deviation of slip can be up to 1.5 m (18% of the peak slip). However, amongst these models the peak slip varies from 8.5 m to 11.7 m, suggesting that peak slip is not a well-constrained variable.

Given the small standard deviation, it is unsurprising that the mean of these slip models (Figure 9a) is visually identical to what is shown in Figure 6a, and has a cumulative seismic moment of 7.55×10^{20} Nm (Mw 7.8). The peak slip of this mean slip distribution is 8.36 m, and also has a compact slip distribution as only 389 (44%) subfaults have significant slip, i.e., slip larger than 10% of the peak slip. Most of the subfaults with significant slip are within the aforementioned large slip patch with an inverse triangle shape (Figure 7a). It extends 152 km along-strike and 56 km down-dip, and the corresponding depth extension is limited to 9.3-15.2 km.

Figures 9c and 9d further show the average stress distribution of the models with $\overline{\Delta\tau_E}^{min}$ and its respective standard deviation. The average stress drop varies from -13.3 to 32.5 MPa over the fault (Figure 9c) but has large uncertainty. The standard deviations on individual subfaults are up to 12.6 MPa with a mean of 3.7 MPa. Considering such a large uncertainty, it is not surprising that in Figure 8c even when we set the maximum local stress drop to 25 MPa (Figure 8c), the inverted model still can explain the data equally well. In other words, in the case where a local maximum stress drop is enforced, the distribution of the average stress drop across the total fault plane does not vary drastically, but there are more individual patches of subfaults with high stress drop, as $\overline{\Delta\tau_E}$ is still being forced to τ_{target}. In Figure 9c, the circles denote the epicenters of 379

M>4.5 aftershocks that occurred between 4/25/2015 and 5/12/2015 and were relocated using the local network data (Adhikari et al., 2015). Although some of them may have occurred outside the fault plane that hosted the mainshock, it can be seen that in map view most of them are located in regions of negative shear stress drop, as expected (Mendoza & Hartzell, 1988).

The group of slip models with $\overline{\Delta\tau_E}^{min}$ are our preferred models. These solutions are generally consistent with previous analyses using seismic and geodetic data (e.g., Avouac et al., 2015; Galetzka et al., 2015; Wang & Fialko, 2015; Yue et al., 2017) in terms of the location of the dominant asperity and its along-strike and down-dip extension. However, we admit that the peak slips of our models are considerably higher than previous analyses, which are less than 6.5 m (Avouac et al., 2015; Galetzka et al., 2015; Wang & Fialko, 2015; Yue et al., 2017). The cause of this discrepancy is not unique. Differences in fault plane depth, subfault size, the weight of the smoothing constraint and the choice of data used are potential reasons. As we mentioned above, the value of the peak slip is not well constrained. Nevertheless, in comparison with the previous Laplacian smoothing constraints, it appears that our new approach tolerates more small-scale variations.

3.7.2 $\overline{\Delta\tau_E}^{min}$ and the energy budget

Our estimate of the seismic potency due to the 2015 M_W 7.8 Gorkha earthquake is 2.28 x 10^{10} m^3 (M_{eb}-7MPa). This value is close to the value inferred from GCMT, 2.54 x 10^{10} m^3, as well as the potency from the USGS W-Phase, 2.01 x 10^{10} m^3 (using the same rigidity of 3.3x10^4MPa). Just considering $\overline{\Delta\tau_E}^{min}$ = 7 MPa, the minimum "apparent"

available strain energy, ΔW_0^{min}, during this earthquake is 7.99 x 10^{16} J. Such an estimate is also data dependent. Using their slip model constrained by teleseismic body waves, Lay et al., (2016) estimated the $\overline{\Delta\tau_E}$ of the Gorkha earthquake to be 3 MPa, a factor of two smaller than our $\overline{\Delta\tau_E}^{min}$ value. We suspect that this discrepancy simply reflects the fact that the near fault static observations better resolve the small scale spatial variations of the fault slip than the teleseismic body waves, i.e., $\overline{\Delta\tau_E}$ estimated using teleseismic data might be systematically lower. Consequently, an underestimation of $\overline{\Delta\tau_E}$ will lead to an underestimation of ΔW_0.

The radiated seismic energy of the Gorkha earthquake has been estimated using teleseismic data by multiple researchers (see a review in Lay et al., 2016), varying within a factor of 2 from 7.1x 10^{15} J to 12.5 x 10^{15} J (e.g., Lay et al., 2016). The corresponding ratio of E_R and M_0 is 0.8-1.5x10^{-5} and the apparent stress drop is 0.3-0.5 MPa. Both are compatible with the global average values of large thrust earthquakes (E_R/M_0, 1.06-1.81x10^{-5}, Convers and Newman, 2011; Ye et al, 2016). Using the ΔW_0^{min} mentioned above, the inferred seismic radiation efficiency ($\eta_R = E_R/\Delta W_0$) is only 0.09-0.15. This estimate of η_R is close to its upper bound, i.e., η_R^{max}, unless E_R was significantly underestimated during the previous studies (e.g., Lay et al., 2016). It is considerably lower compared with estimates of other large earthquakes. Ye et al. (2016) systematically analyzed the finite fault solutions of 114 M_w>7 earthquakes constrained by teleseismic body waves. The mean of their estimates of η_R is 0.34 (logarithmic) or 0.49 (linear) (Ye et al., 2016). However, as mentioned above, η_R estimates in Ye et al. (2016) might be systematically higher because of the underestimated ΔW_0 using teleseismic data.

Understanding the upper bound of η_R has important implications for rupture dynamics. Previous theoretical analyses and observations (e.g., Venkataraman & Kanamori, 2004) indicated a positive correlation between η_R and the rupture speed. Then an upper bound of η_R would help us to define an upper bound for the rupture velocity under some assumptions of the source physics. This inferred maximum rupture velocity could be used in comparison with the observations and subsequently help to verify the underlying source physics. For instance, if the rupture can be modeled as a dynamic mode III crack obeying the slip weakening law, Venkataraman & Kanamori (2004) showed that the rupture velocity satisifies the relation:

$$\eta_R = 1 - \sqrt{(1 - \frac{V_R}{V_s})/(1 + \frac{V_R}{V_s})} \qquad (9)$$

where V_R and V_s are the rupture velocity and shear velocity of the source region. A maximum η_R of 0.15 suggests that the rupture velocity (V_R) would be less than 16% of the shear wave velocity (V_s), i.e., 0.6 km/s. However, the Gorkha earthquake was reported to have a fast rupture velocity, ~2.8-3.2 km/s (Avouac et al., 20015; Galetzka et al., 2015; Lay et al., 2016, Yue et al., 2016), 80-93% of the local shear velocity. This difference of a factor of 5 in the rupture velocity cannot be explained as just an error in the inverted rupture velocity. Furthermore, the rupture velocity of this event is well constrained by the strong motion and high-rate GPS stations that sit on top of the rupture plane.

Though the explanations to this result are not unique, we suspect that it is partially caused by the shape of the rupture patch, which is ignored by equation (8). As mentioned above, the majority of the fault slip during the Gorkha earthquake occurred as unilateral rupture

within a large triangular slip patch (Figure 6), with a length (L) of 152 km and width (W) of 56 km. The L/W ratio is roughly 2.7. According to our best knowledge, Kikuchi & Fukao (1988) first noticed that earthquakes with large L/W ratios often have lower radiation efficiencies, and this has also been confirmed with recent dynamic modeling (Kaneko & Shearer, 2014). Using a quasi-static elliptic crack model similar to Sato & Hirasawa (1973), Kikuchi & Fukao (1988) found that η_R can be approximated as

$$\eta_R \sim (\frac{V_R}{V_S})^2 \varepsilon^{-2} \qquad (10)$$

where ε is the aspect ratio of the elliptic fault patch. According to equation (10), an elliptic fault with large ε, i.e. L/W>>1, would result in a η_R close to zero. This surprising prediction can be explained intuitively. For the constant rupture propagation on such a long fault, its moment rate function can also be approximated as an isosceles trapezoid function, i.e., a Haskell model. Far-field seismic radiation in this approximation is only associated with the beginning and end parts of the moment rate function, which scales with the cube of the width of the fault (W^3) if the stress drop and rupture velocity are constant. In contrast, the fracture energy is proportional to (LW^2). Thus, η_R should be close to zero for large L/W. However, the decay rate due to the aspect ratio of this simple kinematic approach is slower than the more precise prediction using the dynamic elliptic crack model, i.e., equation (10).

Using $\frac{V_R}{V_S}$ = 0.8-0.93 and approximating ε as the L/W ratio mentioned above, the predicted η_R using equation (10) is 0.09-0.12, consistent with our estimation. However, readers should be aware that in the model of Kikuchi and Fukao (1988), the slip within the main asperity varies smoothly. Then, the heterogeneous rupture process during the Gorkha

earthquake suggested by the inverted slip (Figure 6 and 9) and stress drop distributions (Figure 7) will radiate more seismic energy than a quasi-static elliptic crack rupture. Nevertheless, our result suggests that the earthquake rupture could propagate quickly and still dissipate most of the available strain energy in fracturing the fault plane. Hence, investigating the upper bound of η_R provides an additional but interesting angle to study the earthquake rupture process.

3.7.3 Effect of subfault size

The choice of the subfault size is one of the most important *a priori* conditions affecting the source inversion (e.g., Hartzell & Helmberger, 1982; Beresnev, 2003). While small subfaults can provide a more detailed description of the earthquake rupture process, limitations in the station distribution and bandwidth of the data that can be modeled forces modelers to use a large subfault size and to sometimes even ignore slip in one dimension to decrease the number of unknowns (e.g. Bouchon & Vallee, 2003). For the inversion using seismic data, spatial changes less than the smallest wavelength within a certain frequency range of the seismic waves for the analysis cannot be constrained by the data (e.g., Sekiguchi et al., 2000). Thus, in some instances, this has been considered a rough guide for the choice of the subfault size (e.g., Shao & Ji, 2012). For geodetic inversions, efforts have been made to use irregular subfault sizes according to data resolution (e.g., Fialko et al., 2001; Lohman & Simons, 2005; Page et al., 2009).

When we discuss the uncertainty of inverted parameters, the effect of the subfault size cannot be ignored. As stated in the methods section, the stress change is estimated at the center of each subfault. Thus it can only represent a low-pass filtered version of the target

stress distribution. The maximum wavenumber is $\frac{1}{2\Delta x}$, where Δx is the subfault size. In other words, solutions in the model space cannot represent the spatial variation of stress on a scale smaller than two times the subfault size. Such a limitation will inevitably affect the stress estimation of the inverted result (e.g., Dreger et al., 2007), and as it is an *a priori* condition its impact can only be explored by comparing the final results using different subfault sizes. The comparison shown in Figure 4b suggests that the low bound of $\overline{\Delta\tau}_E$ defined here is stable in terms of the subfault size but the upper bound of $\overline{\Delta\tau}_E$ is not. Readers should also be aware that such a conclusion is for the relatively "small" subfault sizes of 4 to 8 km. If we instead use a much larger subfault size, even the low bound of $\overline{\Delta\tau}_E$ could be affected. For a given earthquake, the "small" or "large" subfault sizes mentioned here are not absolute values. Instead it is correlated with not only the data used but also the earthquake itself. A stable $\overline{\Delta\tau}_E^{\,min}$ can, therefore, be used as one of the conditions during the search for an appropriate subfault size for the given observations.

The uncertainty of $\overline{\Delta\tau}_E$ has received considerable attention in the source inversion community. Duputel et al. (2015) estimated the uncertainty of $\overline{\Delta\tau}_E$ during the 2014 Mw 8.1 Iquique earthquake by analyzing the ensemble of accepted solutions obtained during their Bayesian inversion. They found the posterior probability density of $\overline{\Delta\tau}_E$ has a peak around 10 MPa, and is negligible for $\overline{\Delta\tau}_E$<5 MPa and $\overline{\Delta\tau}_E$>25 MPa. In principle all accepted solutions during Bayesian inversions should have good misfit values, and to some extent the probability of the solutions are correlated with the misfit values. The low posterior probability density for models with smaller $\overline{\Delta\tau}_E$ is then consistent with our

result, and $\overline{\Delta\tau_E}^{min}$ is close to 5 MPa. At first glance, the low posterior probability density for the models with large $\overline{\Delta\tau_E}$ is inconsistent with our result. However, as we mentioned above (Figure 4a), such an apparent $\overline{\Delta\tau_E}^{max}$ of about 25 MPa can simply be an artificial result of using large subfaults. Besides, it is noteworthy that the inferred posterior probability density of one model also depends on the topology of the model space near this optimal solution. For example, even the two arbitrary optimal solutions have the exact same misfit value, the one associated with a broad and flat "basin" type minimum in terms of the misfit value has a higher posterior probability density than the other with a narrow "valley" type minimum. Therefore, it is also possible that the latter scenario is associated with the optimal models with large $\overline{\Delta\tau_E}$. Nevertheless, the low posterior probability density for the models with large $\overline{\Delta\tau_E}$ found by Duputel et al. (2015) cannot be used as unique evidence against our statement that the $\overline{\Delta\tau_E}^{max}$ of an earthquake cannot be solely constrained by the surface geophysical observations. Instead, it might provide supplementary information on this interesting source property.

3.7.4 Using $\overline{\Delta\tau_E}^{min}$ as a new inversion constraint

We end our discussion by outlining the finite fault inversion strategy using the "*minimum average stress drop constraint*". After the routine data and Green's functions preparation, this new inversion procedure starts with a grid search for $\overline{\Delta\tau_E}^{min}$. The subfault size will then gradually be reduced until $\overline{\Delta\tau_E}^{min}$ becomes stable and the flat pattern shown in Figure 4b can be observed in the trade-off curve between the misfit and $\overline{\Delta\tau_E}$. A method such as the L-curve algorithm mentioned above is then applied to more rigorously determine the point of maximum curvature. The corresponding stress drop thus becomes

$\overline{\Delta\tau_E}^{min}$ of this earthquake, which is data dependent. To explore the epistemic uncertainty in the inverted slip and stress drop distributions, multiple inversions with $\tau_{target} = \overline{\Delta\tau_E}^{min}$ are then conducted, with the only difference in this part being the choice of the initial model. Other types of perturbations, such as bootstraping the data (Custodio et al., 2009) or allowing a perturbation in the alignment of data and synthetics (Hartzell et al., 2007) when using seismic data, could be included in a future study. It is of interest to note that the new procedure has no parameter that needs to be assigned empirically. However, as hundreds of inversions need to be conducted, this procedure is time consuming. Nevertheless, all individual inversions are independent and identical in a computational perspective. The entire procedure is then easily made parallel and can take full advantage of desktops or clusters with a modern multiple core CPU or GPU.

3.8 Conclusion

Resolving the state of stress on the fault is a key component in understanding the physics of earthquakes, and it has important implications to the earthquake energy budget. As a continuation of our companion work (Adams et al., 2017), we found that only the lower bound of the energy based average stress drop $\overline{\Delta\tau_E}$ can be constrained using teleseismic data, and here we demonstrate that this argument holds even with excellent near-source geodetic data for the 2015 M_W 7.8 Gorkha earthquake. The lower bound of $\overline{\Delta\tau_E}$ or $\overline{\Delta\tau_E}^{min}$ during this earthquake is ~7 MPa. We also show numerically that the upper bound of $\overline{\Delta\tau_E}$ may also be constrained if an extra constraint to the maximum local stress drop is available (e.g. via laboratory experiments). At the same time, readers should be

cautious about a potential pseudo-upper bound of $\overline{\Delta\tau_E}$ resulting from the use of a large subfault size to represent the source.

The lower bound of $\overline{\Delta\tau_E}$ leads to the lower bound of the apparent available strain energy ΔW_0 (7.99×10^{16} J) and an upper bound of the seismic radiation efficiency (η_R), though the latter is also affected by the large uncertainty of the observed seismic radiated energy. Both of these are important parameters in earthquake energy budget analyses. The estimate of η_R^{max} is 0.09-**0.15**, despite the high rupture velocity (V_R=83-94% of the shear wave speed). We point out that the low η_R and high V_R can be reconciled by considering the aspect ratio of the dominant slip patch. The earthquake rupture with large aspect ratio could propagate quickly but still dissipate most of the available strain energy in fracturing the fault plane. Finally, we have introduced a new, more physical constraint to smooth the inverted fault slip during finite fault inversions, the "*minimum average stress drop constraint*", which is based on finding the slip and stress distribution with the minimum available strain energy of the earthquake.

.

3.9 References

Adhikari, L.B., Gautam, U.P., Koirala, B.P., Bhattarai, M., Kandel, T., Gupta, R.M., Timsina, C., Maharjan, N., Maharjan, K., Dahal, T. and Hoste-Colomer, R., 2015. The aftershock sequence of the 2015 April 25 Gorkha–Nepal earthquake. *Geophysical Supplements to the Monthly Notices of the Royal Astronomical Society*, *203*(3), 2119-2124.

Adams, M., Twardzik, C. & Ji, C., 2017. Exploring the uncertainty range of coseismic stress drop estimations of large earthquakes using finite fault inversions. *Geophysical Journal International*, 208, pp.86–100.

Ader, T., Avouac, J. P., Liu-Zeng, J., Lyon-Caen, H., Bollinger, L., Galetzka, J., … Flouzat, M., 2012. Convergence rate across the Nepal Himalaya and interseismic coupling on the Main Himalayan Thrust: Implications for seismic hazard. *Journal of Geophysical Research: Solid Earth*, *117*(4), 1–17.

Avouac, J. P., 2003. Mountain building, erosion, and the seismic cycle in the Nepal Himalaya. In: *Advances in geophysics*, *46*, Elsevier, San Diego 1-80.

Avouac, J.-P. et al., 2015. Lower edge of locked Main Himalayan Thrust unzipped by the 2015 Gorkha earthquake. *Nature Geoscience*, 8(9), pp.708–711.

Bassin, C., Laske, G., & Masters, G., 2000. The current limits of resolution for surface wave tomography in North America. *Eos*, *81*.

Beresnev, I.A., 2003. Uncertainties in finite-fault slip inversions: To what extent to believe? (A critical review). *Bulletin of the Seismological Society of America*, 93(6), pp.2445–2458.

Bilham, R., Gaur, V. K., & Molnar, P., 2001. Himalayan seismic hazard. *Science*, *293*(5534), 1442-1444.

Bouchon, M. & Vallee, M., 2003. Observation of Long Supershear Rupture during the Magnitude 8 . 1 Kunlunshan Earthquake. *Science*, 301, pp.824–826.

Brune, J.N., 1970. Tectonic stress and the spectra of seismic shear waves from earthquakes. *Journal of Geophysical Research*, 75(26), pp.4997–5009.

Causse, M., Dalguer, L. A., & Mai, P. M., 2014. Variability of dynamic source parameters inferred from kinematic models of past earthquakes. *Geophysical Journal International*, *196*(3), 1754–1769.

Convers, J. A., & Newman, A. V., 2011. Global evaluation of large earthquake energy from 1997 through mid-2010. *Journal of Geophysical Research: Solid Earth*, *116*(8), 1–17.

Cotton, F. & Campillo, M., 1995. Frequency domain inversion of strong motions: application to the 1992 Landers earthquake. *Journal of Geophysical Research*, 100(B3), pp.3961–3975.

Custódio, S., Page, M.T. & Archuleta, R.J., 2009. Constraining earthquake source inversions with GPS data: 2. A two-step approach to combine seismic and geodetic data sets. *Journal of Geophysical Research: Solid Earth*, 114(1), pp.1–20.

Denolle, M.A., Fan, W. & Shearer, P.M., 2015. Dynamics of the 2015 M7.8 Nepal earthquake. *Geophysical Research Letters*, 42(18), pp.7467–7475.

Dreger, D., Nadeau, R.M. & Chung, A., 2007. Repeating earthquake finite source models: Strong asperities revealed on the San Andreas fault. *Geophysical Research Letters*, 34(23), pp.1–5.

Du, Y., Aydin, A. & Segall, P., 1992. Comparison of various inversion techniques as applied to the determination of a geophysical deformation model for the 1983 Borah Peak earthquake. *Bulletin of the Seismological Society of America*, 82(4), pp.1840–

1866.

Duputel, Z., Jiang, J., Jolivet, R., Simons, M., Rivera, L., Ampuero, J.P., Riel, B., Owen, S.E., Moore, A.W., Samsonov, S.V. and Ortega Culaciati, F., 2015. The Iquique earthquake sequence of April 2014: Bayesian modeling accounting for prediction uncertainty. *Geophysical Research Letters*, 42(19), pp.7949-7957.

Fan, W., & Shearer, P. M., 2015. Detailed rupture imaging of the 25 April 2015 Nepal earthquake using teleseismic P waves. *Geophysical Research Letters*, *42*(14), 5744–5752.

Fialko, Y., Simons, M., & Agnew, D., 2001. The complete (3‐D) surface displacement field in the epicentral area of the 1999 Mw7. 1 Hector Mine earthquake, California, from space geodetic observations. *Geophysical Research Letters*, *28*(16), 3063-3066.

Galetzka J., Melgar D, Genrich J.F, Geng J., Owen S., Lindsey EO, Xu X., Bock Y, Avouac J.P, Adhikari L.B, Upreti B.N, Pratt-Sitaula B., Bhattarai T.N, Sitaula B.P, Moore A., Hudnut K.W, Szeliga W., Normandeau J., Fend M., Flouzat M., Bollinger L., Shrestha P., Koirala B., Gautam U., Bhatterai M., Gupta R., Kandel T., Timsina C., Sapkota S.N, Rajaure S., Maharjan N., 2015. Slip pulse and resonance of the Kathmandu basin during the 2015 Gorkha earthquake, Nepal. *Science*, 349(6252), pp.1091–1095.

Hansen, P.C. & O'Leary, D.P., 1993. The Use of the L-Curve in the Regularization of Discrete Ill-Posed Problems. *SIAM Journal on Scientific Computing*, 14(6), pp.1487–1503.

Hartzell, S. H., & Heaton, T. H., 1983. Inversion of strong ground motion and teleseismic waveform data for the fault rupture history of the 1979 Imperial Valley, California, earthquake. *Bulletin of the Seismological Society of America*, *73*(6), 1553–1583.

Hartzell, S. & Helmberger, D. V., 1982. Strong-motion modeling of the imperial valley earthquake of 1979. *Bulletin of the Seismological Society of America*, 72(2), pp.571–596.

Hartzell, S., Liu, P., Mendoza, C., Ji, C., & Larson, K. M., 2007. Stability and uncertainty of finite-fault slip inversions: Application to the 2004 Parkfield, California, earthquake. *Bulletin of the Seismological Society of America*, *97*(6), 1911-1934.

Hartzell, S. H., Stewart, G. S., & Mendoza, C., 1991. Comparison of L 1 and L 2 norms in a teleseismic waveform inversion for the slip history of the Loma Prieta, California, earthquake. *Bulletin of the Seismological Society of America*, *81*(5), 1518-1539.

Heaton, T. H., & Heaton, R. E., 1989. Static deformations from point forces and force couples located in welded elastic Poissonian half-spaces: Implications for seismic moment tensors. *Bulletin of the Seismological Society of America*, *79*(3), 813–841.

Husseini, M. I., 1977. Energy balance for motion along a fault. *Geophys. J. R. Astr. Soc.*, *49*, 699–714.

Ide, S., Takeo, M. & Yoshida, Y., 1996. Source process of the 1995 kobe earthquake: Determination of spatio-temporal slip distribution by bayesian modeling. *Bulletin of the Seismological Society of America*, 86(3), pp.547–566.

Ji, C., Wald, D. J., & Helmberger, D. V., 2002. Source Description of the 1999 Hector Mine , California , Earthquake , Part I : Wavelet Domain Inversion Theory and Resolution Analysis, *92*(4), 1192–1207.

Ji, C., Wald, D.J. & Helmberger, D. V., 2002. Source description of the 1999 Hector Mine, California, earthquake, part II: Complexity of slip history. *Bulletin of the Seismological Society of America*, 92(4), pp.1208–1226.

Kanamori, H., & Allen, C. R., 1986. Earthquake repeat time and average stress drop.

Kanamori, H. & Rivera, L., 2006. Energy Partitioning During an Earthquake. *Earthquakes: Radiated Energy and the Physics of Faulting*, pp.3–13.

Kaneko, Y., & Shearer, P. M., 2014. Seismic source spectra and estimated stress drop derived from cohesive-zone models of circular subshear rupture. *Geophysical Journal International*, *197*(2), 1002–1015.

Kikuchi, M., & Fukao, Y., 1988. Seismic wave energy inferred from long-period body wave inversion. *Bulletin of the Seismological Society of America*, *78*(5), 1707-1724.

Larson, K. M., Bürgmann, R., Bilham, R., & Freymueller, J. T., 1999. Kinematics of the India-Eurasia collision zone from GPS measurements. *Journal of Geophysical Research: Solid Earth*, *104*(B1), 1077-1093.

Lay, T., Ye, L., Koper, K. D., & Kanamori, H., 2016. Assessment of teleseismically-determined source parameters for the April 25, 2015 MW 7.9 Gorkha, Nepal earthquake and the May 12, 2015 MW 7.2 aftershock. *Tectonophysics*.

Lindsey, Eric O.; Natsuaki, Ryo; Xu, Xiaohua; Shimada, Masanobu; Hashimoto, Manabu; Melgar, Diego; Sandwell, David T., 2015. Line-of-sight displacement from ALOS-2 interferometry: Mw 7.8 Gorkha Earthquake and Mw 7.3 aftershock. *Geophysical Research Letters*, 42(16), pp.6655–6661.

Lohman, R. B., & Simons, M., 2005. Some thoughts on the use of InSAR data to constrain models of surface deformation: Noise structure and data downsampling. *Geochemistry, Geophysics, Geosystems*, *6*(1).

Madariaga, R., 1979. On the Relation Between Seismic Moment and Stress Drop in the Presence of Stress and Strength Heterogeneity. *Journal of Geophysical Research*, *84*(B5), 2243–2250.

McGarr, A., 1999. On relating apparent stress to the stress causing earthquake fault slip. *Journal of Geophysical Research*, *104*(B2), 3003–3011.

McLaskey, G. C., Kilgore, B. D., Lockner, D. A., & Beeler, N. M., 2014. Laboratory generated M-6 earthquakes. *Pure and Applied Geophysics*, *171*(10), 2601-2615.

Mcnamara, D.E. et al., 2016. Tectonophysics Source modeling of the 2015 Mw 7.8 Nepal (Gorkha) earthquake sequence : Implications for geodynamics and earthquake hazards. *Tectonophysics*, TECTO-1272, pp.0–9.

Mendoza, C., & Hartzell, S. H., 1988. Aftershock patterns and main shock faulting. *Bulletin of the Seismological Society of America*, *78*(4), 1438-1449.

Mendoza, C. & Hartzell, S., 2013. Finite-fault source inversion using teleseismic P waves: Simple parameterization and rapid analysis. *Bulletin of the Seismological Society of America*, 103(2 A), pp.834–844.

Molnar, P., 1988. A review of geophysical constraints on the deep structure of the Tibetan Plateau, the Himalaya and the Karakoram, and their tectonic implications. *Phil. Trans. R. Soc. Lond. A*, *326*(1589), 33-88.

Noda, H., Lapusta, N. & Kanamori, H., 2013. Comparison of average stress drop measures for ruptures with heterogeneous stress change and implications for earthquake physics. *Geophysical Journal International*, 193(3), pp.1691–1712.

Okada, Y., 1992. Internal deformation due to shear and tensile faults in a half-space. *Bulletin of the Seismological Society of America*, 82(2), pp.1018–1040.

Olson, A.H. & Apsel, R.J., 1982. Finite faults and inverse theory with applications to the

1979 Imperial Valley earthquake. *Bulletin of the Seismological Society of America*, 72(6), pp.1969–2001.

Page, M. T., Custódio, S., Archuleta, R. J., & Carlson, J. M., 2009. Constraining earthquake source inversions with GPS data: 1. Resolution‐based removal of artifacts. *Journal of Geophysical Research: Solid Earth*, *114*(B1).

Razafindrakoto, Hoby N. T.; Mai, P. Martin; Genton, Marc G.; Zhang, Ling; Thingbaijam, Kiran K. S., 2015. Quantifying variability in earthquake rupture models using multidimensional scaling: application to the 2011 Tohoku earthquake. *Geophysical Journal International*, 202(1), pp.17–40.

Sato, T., & Hirasawa, T., 1973. Body wave spectra from propagating shear cracks. *Journal of Physics of the Earth*.

Sekiguchi, H., Irikura, K. & Iwata, T., 2000. Fault geometry at the rupture termination of the 1995 Hyogo-ken Nanbu earthquake. *Bulletin of the Seismological Society of America*, 90(1), pp.117–133.

Shao, G., & Ji, C., 2012. What the exercise of the SPICE source inversion validation BlindTest 1 did not tell you. *Geophysical Journal International*, *189*(1), 569–590.

Shao, G., Ji, C. & Hauksson, E., 2012. Rupture process and energy budget of the 29 July 2008 Mw 5.4 Chino Hills, California, earthquake. *Journal of Geophysical Research: Solid Earth*, 117(7), pp.2–13.

Twardzik, C., & Ji, C., 2015. The Mw7.9 2014 intraplate intermediate-depth Rat Islands earthquake and its relation to regional tectonics. *Earth and Planetary Science Letters*, *431*, 26–35.

Venkataraman, A. & Kanamori, H., 2004. Observational constraints on the fracture

energy of subduction zone earthquakes. *Journal of Geophysical Research: Solid Earth*, 109(B05302), pp.1–20.

Wang, K. & Fialko, Y., 2015. Slip model of the 2015 Mw 7.8 Gorkha (Nepal) earthquake from inversions of ALOS-2 and GPS data. *Geophysical Research Letters*, 42, pp.7452–7458.

Xie, X., & Yao, Z. X., 1989. A generalized reflection-transmission coefficient matrix method to calculate static displacement field of a dislocation source in a stratified half space. *Chin. J. Geophys*, *32*, 191-205.

Ye, L., Lay, T., Kanamori, H., & Rivera, L., 2016. Rupture characteristics of major and great (M W ≥ 7.0) megathrust earthquakes from 1990-2015: I. Source parameter scaling relationships. *Journal of Geophysical Research: Solid Earth*, 121, 845-863.

Yue, H., Simons, M., Duputel, Z., Jiang, J., Fielding, E., Liang, C., Owen, S., Moore, A., Riel, B., Ampuero, J. P., Samsonov, S. V., 2016. Tectonophysics Depth varying rupture properties during the 2015 Mw 7.8 Gorkha (Nepal) earthquake. *Tectonophysics*, TECTO-1271.

Zhang, H., Van Der Lee, S., & Ge, Z. (2016). Multiarray rupture imaging of the devastating 2015 Gorkha, Nepal, earthquake sequence. *Geophysical Research Letters*, *43*(2), 584–591.

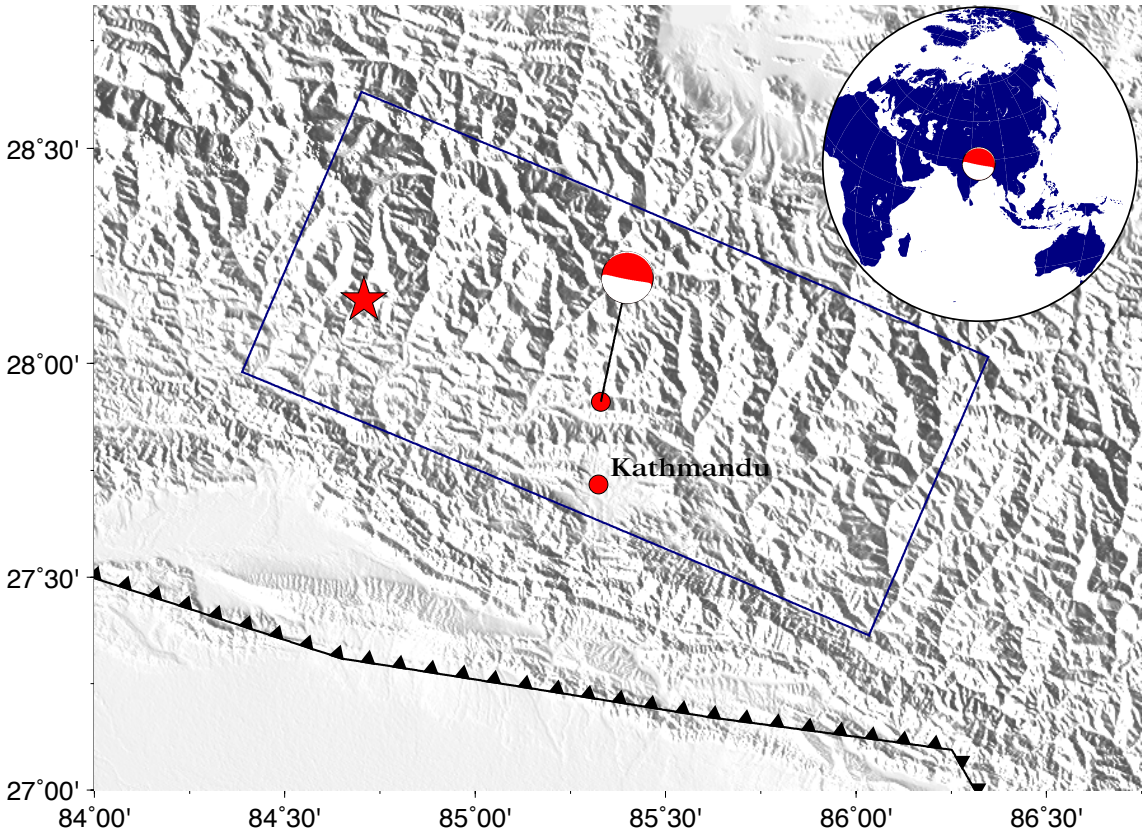

Figure 1: Tectonic setting of the 2015 M_W 7.9 Gorkha earthquake with the GCMT solution and focal mechanism shown. The star locates the hypocenter that was used in the finite fault inversions, and the slip contours (in m) of the preferred inverted model are superimposed in blue.

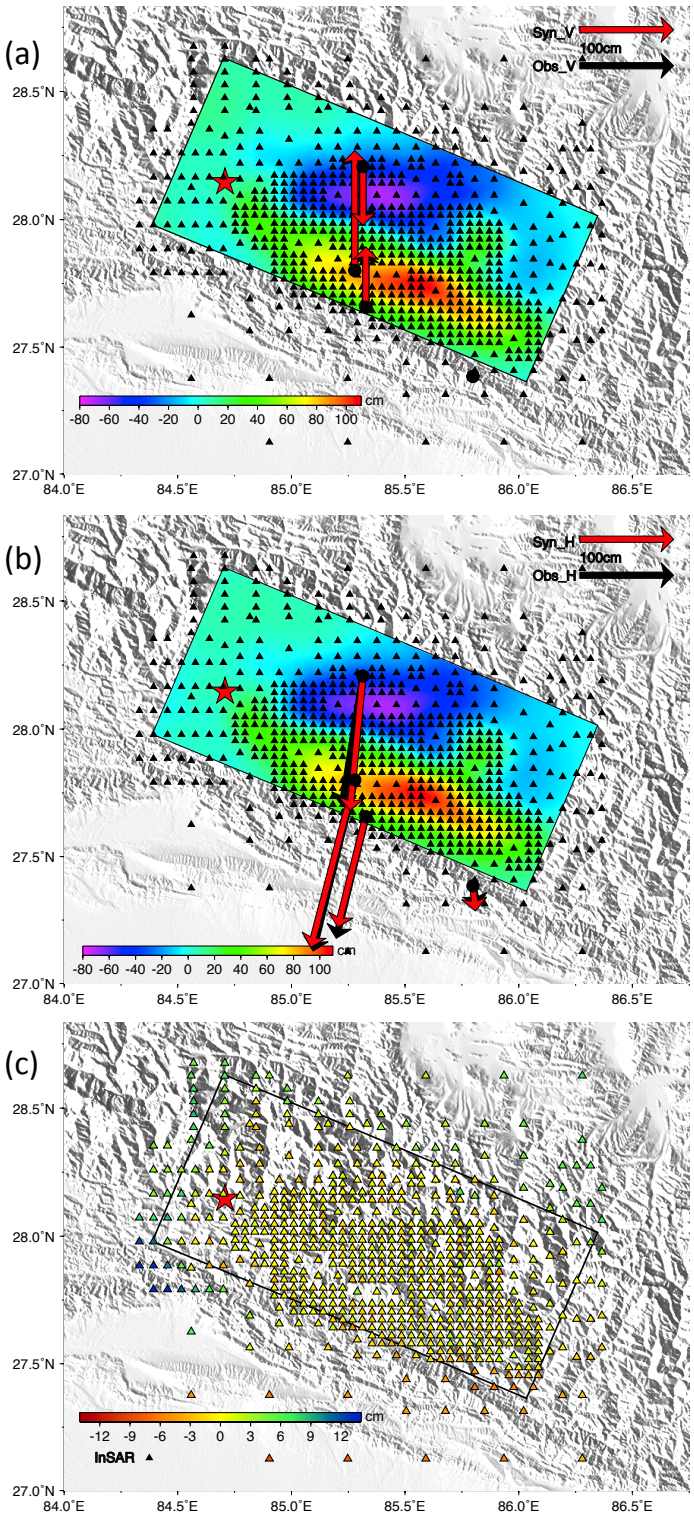
(a)
Syn_V
100cm
Obs_V
cm
-80 -60 -40 -20 0 20 40 60 80 100
(b)
Syn_H
100cm
Obs_H
cm
-80 -60 -40 -20 0 20 40 60 80 100
(c)
cm
-12 -9 -6 -3 0 3 6 9 12
InSAR
28.5°N
28.0°N
27.5°N
27.0°N
84.0°E
84.5°E
85.0°E
85.5°E
86.0°E
86.5°E

Figure 2: (a) Distribution of the resampled points of InSAR LOS measurements (black triangles) and GPS stations (black circles), accompanied with the image of the unwrapped ALOS-2 LOS displacement field. The color bar denotes the motion amplitude. The black and red arrows show the GPS observed and synthetic vertical offsets, respectively. See text for details. (b) Similar to (a) but synthetic image of the LOS displacement field. The black and red arrows show the GPS observed and synthetic horizontal offsets, respectively. (c) Distribution of the resampled points (triangles) with the colors showing the amplitude of the residuals (observed-synthetic).

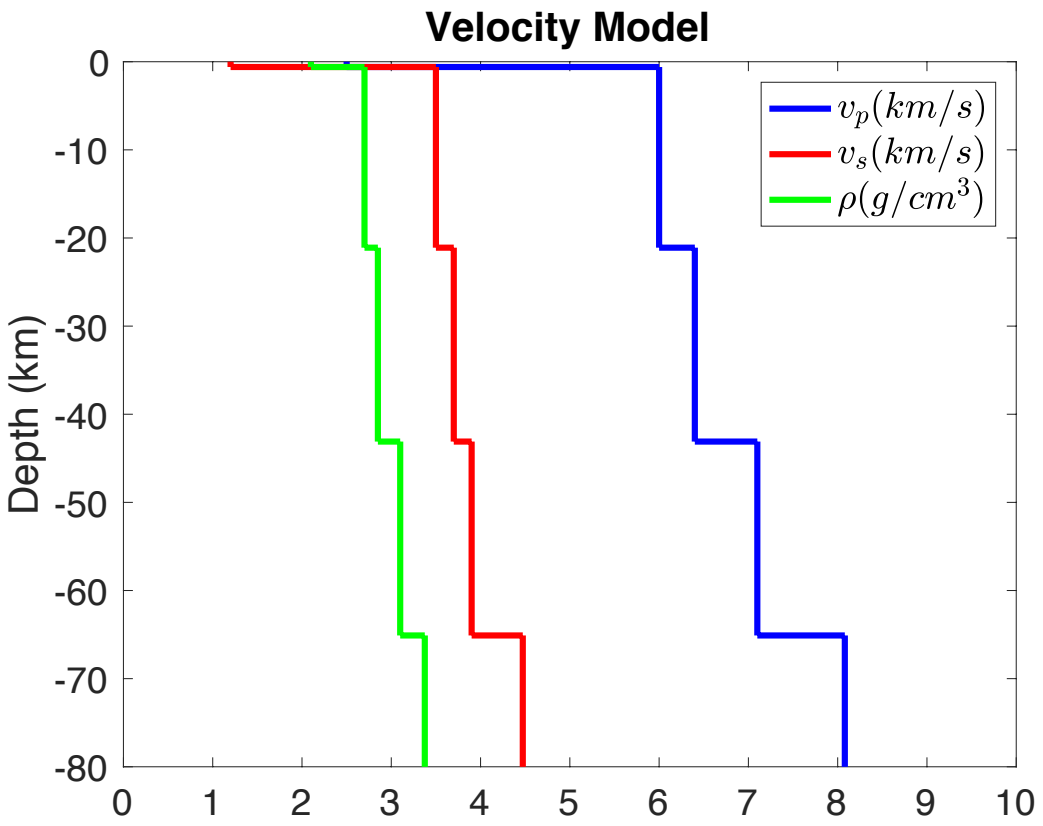

Figure 3: 1D Velocity model used in all inversions. The P-wave velocity (km/s), S-wave velocity (km/s), and the density (g/cm^3) are shown in blue, red and green, respectively.

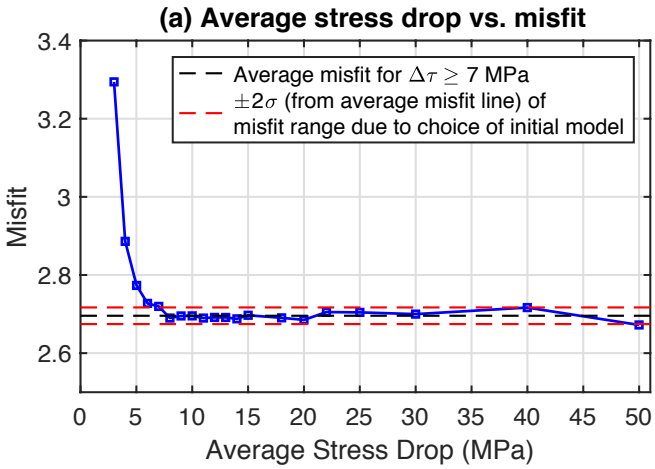
(a) Average stress drop vs. misfit
Average misfit for $\Delta\tau \geq 7$ MPa
$\pm 2\sigma$ (from average misfit line) of misfit range due to choice of initial model
Misfit
Average Stress Drop (MPa)

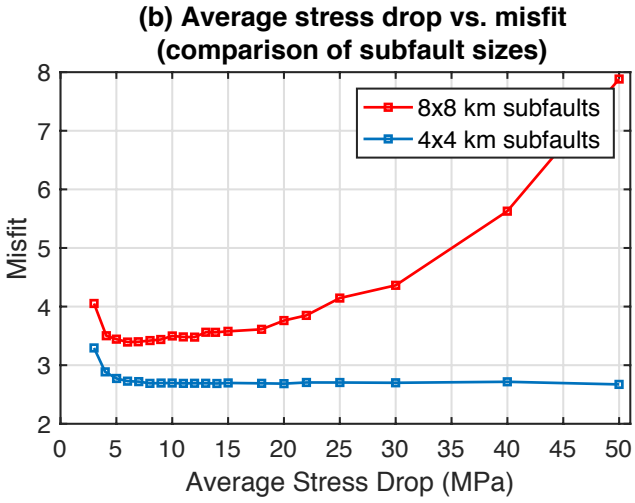
(b) Average stress drop vs. misfit (comparison of subfault sizes)
8x8 km subfaults
4x4 km subfaults
Misfit
Average Stress Drop (MPa)

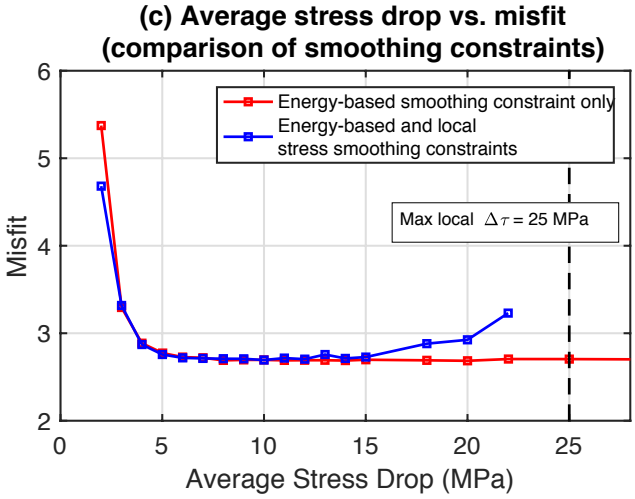
(c) Average stress drop vs. misfit (comparison of smoothing constraints)
Energy-based smoothing constraint only
Energy-based and local stress smoothing constraints
Max local $\Delta\tau$ = 25 MPa
Misfit
Average Stress Drop (MPa)

Figure 4: (a) Energy based average stress drop ($\overline{\Delta\tau_E}$, MPa) versus RMS misfit (cm) for inversions using a subfault size of 4x4 km. Only the fixed average stress drop constraint is used (equation 6). The misfit first decreases as $\overline{\Delta\tau_E}$ increases, suggesting it is possible to define a clear lower bound. The average misfit for $\overline{\Delta\tau_E} \geq 7$ MPa is plotted as the black dashed line, and ±2σ of the misfit range due to the choice of the initial model is plotted as the red lines.

(b) Comparison of the relationships of the energy based average stress drop ($\overline{\Delta\tau_E}$, MPa) and misfit (cm) for inversions using a subfault size of 8x8 km (in red) and 4x4 km (in blue). Only the fixed average stress drop constraint is used. The misfit in both cases first decreases as $\overline{\Delta\tau_E}$ increases, suggesting it is possible to define a clear lower bound. However, only the misfit in the tests using 8x8 km subfaults increases significantly again as $\overline{\Delta\tau_E}$>25 MPa.

(c) Comparison of the relationships of the energy based average stress drop ($\overline{\Delta\tau_E}$ in MPa) and misfit (cm) for inversions using the additional fixed maximum local stress constraint (in blue), and inversions without (in red), both with 4x4 km subfaults and the fixed average stress drop constraint. The misfit in both cases first decreases as $\overline{\Delta\tau_E}$ increases, suggesting it is possible to define a clear lower bound. The local stress constraint imposes a maximum local stress drop of 25 MPa. Thus, the blue curve cannot converge to any values greater than 25 MPa. The blue curve also increases rapidly as $\overline{\Delta\tau_E}$ increases and approaches the local maximum.

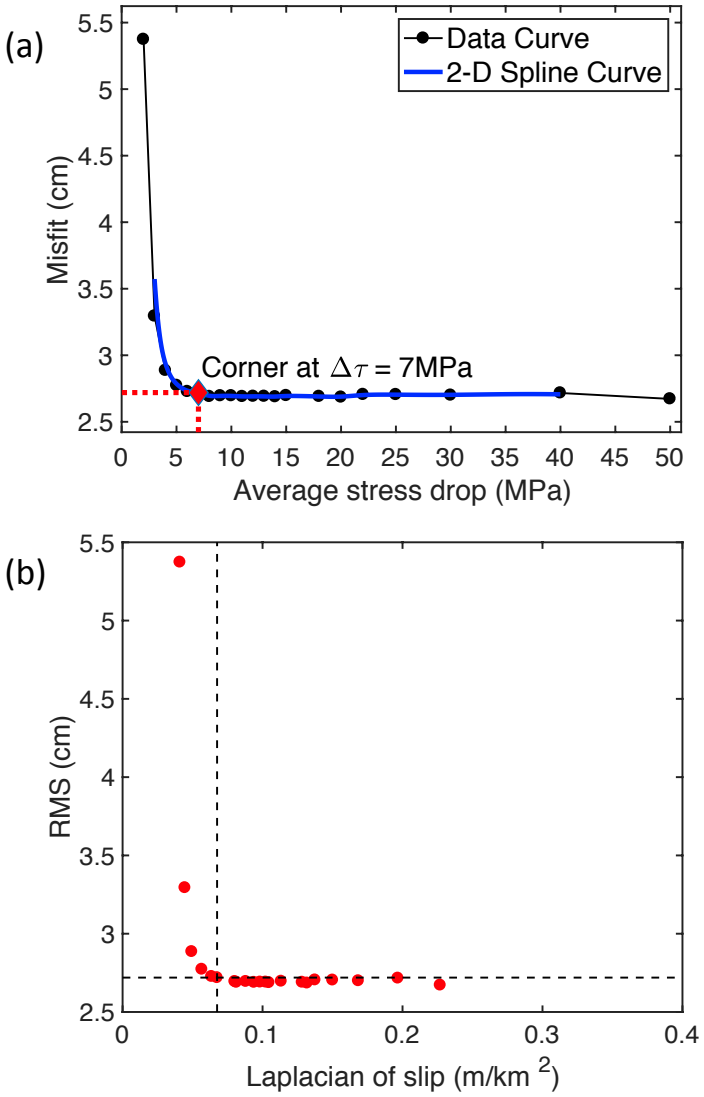

Figure 5: (a) L-curve illustrating the trade-off between the average stress drop (in MPa) and the misfit (cm). Black dots denote the models used, which are treated as data. A fourth order 2D spline curve used to fit the data is in blue. The corner, or the point of maximum curvature of the blue line, is located near $\overline{\Delta\tau_E}$ = 7 MPa. See text for details. (b) Fault roughness (Laplacian of slip) versus RMS misfit (cm). The dashed lines represent the values of the Laplacian and the RMS of the model with $\overline{\Delta\tau_E}$ = 7 MPa.

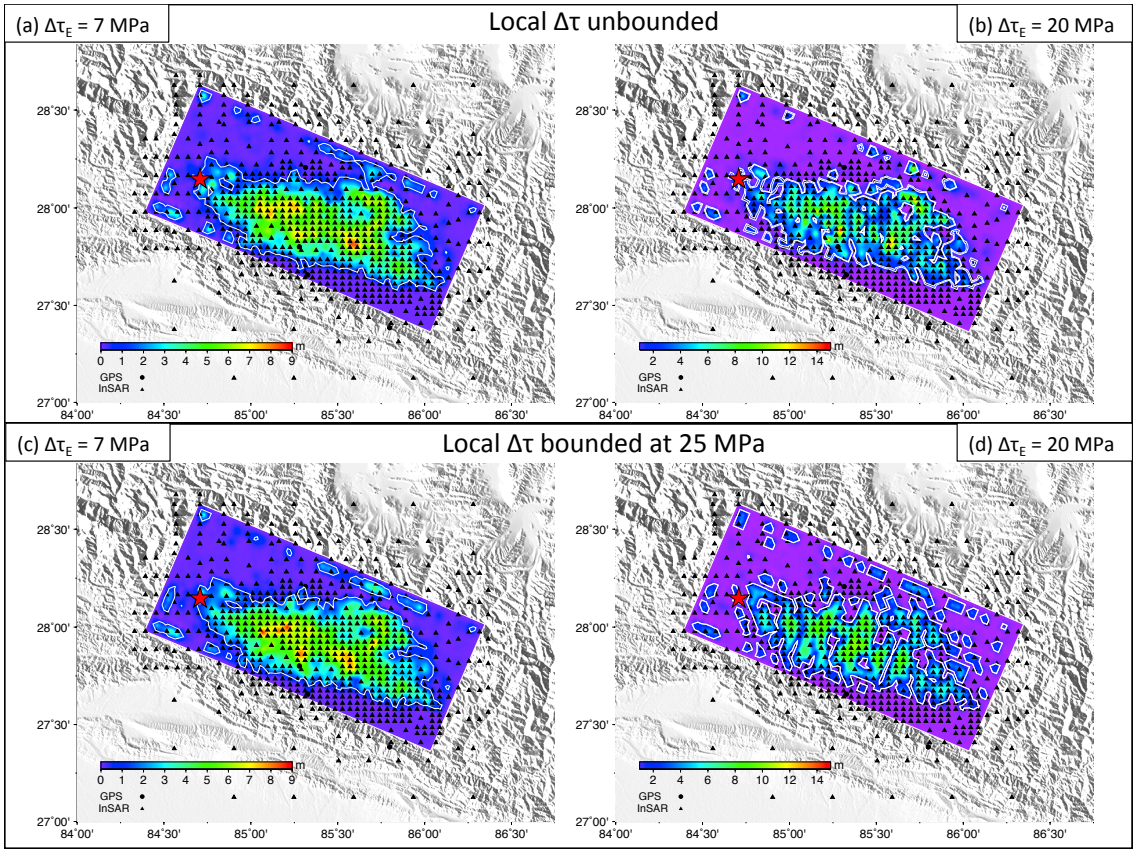

Figure 6: Slip distributions for inversions with just the fixed average stress drop constraint, (a) and (b), and also with the additional maximum local stress constraint, (c) and (d). Figures (a) and (c) have $\overline{\Delta\tau_E}$ equal to 7 MPa, and (b) and (d) have $\overline{\Delta\tau_E}$ = 20 MPa. Contours outline the areas with slip (m) greater than 10% of the peak slip value. Visible greater degree of heterogeneity in tests done with a higher $\overline{\Delta\tau_E}$, though the overall shape of the large slip patch is well resolved in both distributions.

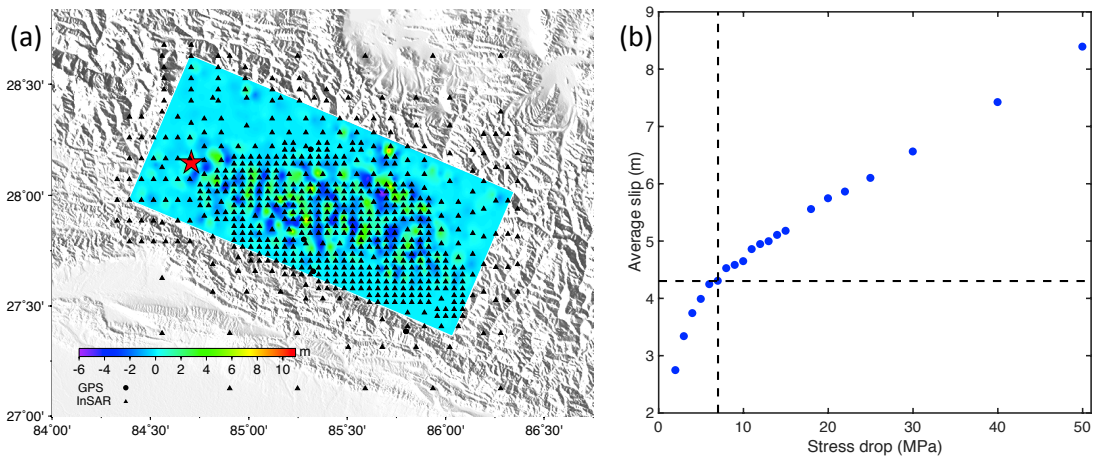

Figure 7: (a) Map projection of the difference between the slip distributions of M_{eb}-20MPa and M_{eb}-7MPa. **(b)** Variation of weighted average slip (m) for subfaults with displacement greater than 10% of the peak slip value versus stress drop (MPa). The vertical dashed line marks $\overline{\Delta\tau_E}$ = 7 MPa, and the horizontal line shows the corresponding average slip value.

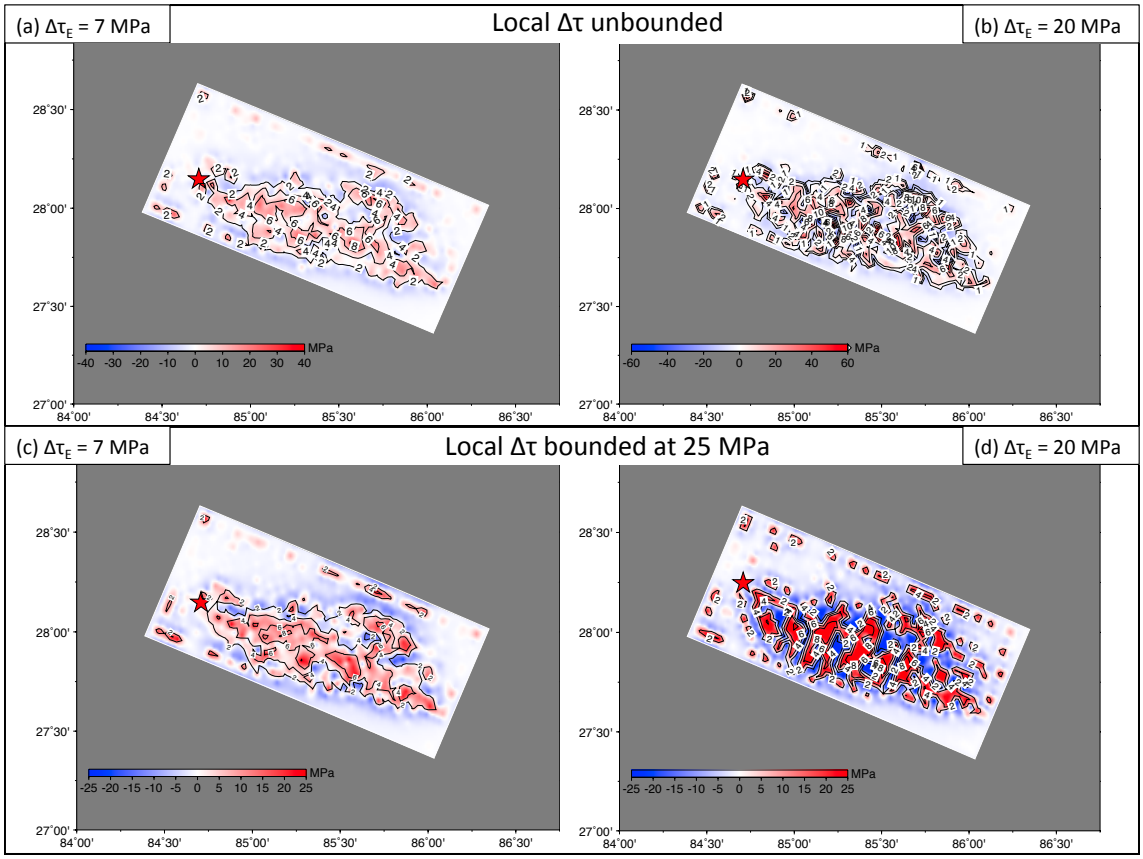

Figure 8: Stress distributions for inversions using just the fixed average stress drop constraint, (a) and (b), and with the additional maximum local stress constraint, (c) and (d). Figures (a) and (c) have $\overline{\Delta\tau_E}$ equal to 7 MPa, and (b) and (d) have $\overline{\Delta\tau_E}$ = 20 MPa. Shear stress drop in the overall slip direction (rake angle of 96^o) is shown. Visible greater degree of heterogeneity in the tests done with a higher $\overline{\Delta\tau_E}$, though the overall regions of high stress are well resolved in both distributions. Clearly, imposing a local maximum allowable stress drop forces a generally smoother and more widely distributed stress distribution, (c) and (d). In all cases, the respective slip distribution (shown in Figure 6) is contoured and superimposed on the stress distributions here.

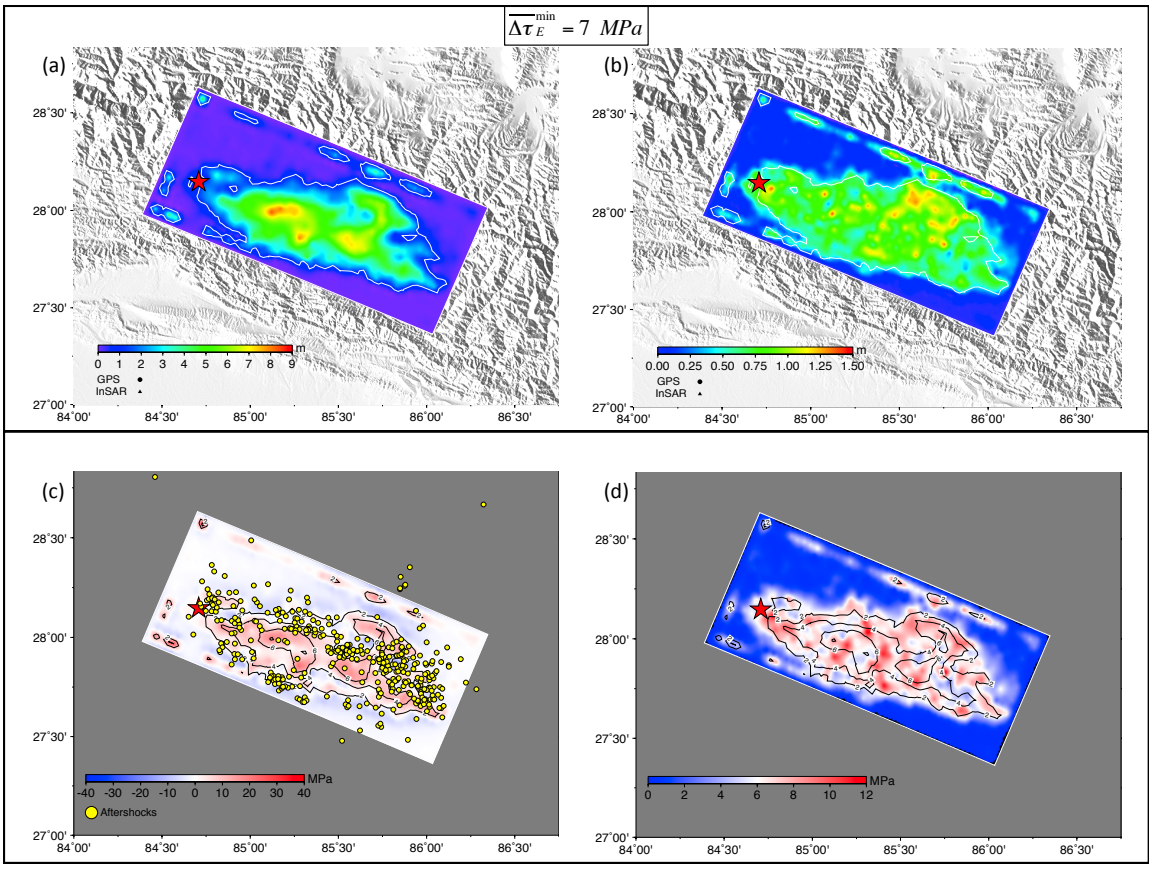

Figure 9: (a) Average slip distribution for ten different models, varying only the choice of the initial model, with $\overline{\Delta\tau_E}^{min} = 7\ MPa$, and (b) distribution of the standard deviation of the ten models. Contours outline the area where greater than 10% of the peak slip occurs. (c) Average stress distribution of the ten models and (d) the distribution of the standard deviation of the ten different models used to create the average model. Contours outlining the slip distribution in (a) are superimposed on the stress distributions in (c) and (d).

4. Insights into the fault geometry and rupture history of the 2016 M_W 7.8 Kaikoura, New Zealand, earthquake

4.1 Abstract

The November 14th 2016 M_W 7.8 Kaikoura, New Zealand earthquake occurred along the east coast of the northern part of the South Island. The local tectonic setting is complicated. The central South Island is dominated by oblique continental convergence; whereas the southern part of this island experiences eastward subduction of the Australian plate. Available information (e.g., Hamling et al., 2017; Bradley et al., 2017) indicate that this earthquake involved multiple fault segments of the Marlborough fault system (MFS) as the rupture propagated northwards for more than 150 km. Additional slip might also occur on the subduction interface of the Pacific Plate under the Australian Plate, beneath the MFS. However, the exact number of involved fault segments as well as the temporal co-seismic rupture sequence has not been fully determined with geodetic and geological observations. Knowledge of the kinematics of complex fault interactions has important implications for our understanding of global seismic hazards, particularly in the modeling of multi-segment ruptures. Understanding the Kaikoura earthquake will provide insight into how one incorporates multi-fault ruptures in seismic-hazard models. We propose two inversion strategies to determine the fault geometry and spatiotemporal rupture history: first we use teleseismic and strong motion waveforms to determine point-source focal mechanisms for all of the faults that participated in the rupture; second, we use seismic and geodetic data to invert for the kinematic rupture parameters on a limited number of fault segments. In the first approach we approximate the Kaikoura earthquake as the summation of multiple subevents. This allows us to determine a rupture timing sequence for different fault segments. It also allows us to evaluate the potential of slip on the Hikurangi subduction interface. Once we have the multiple double-couple solution

and timing among fault segments, we invert the seismic and geodetic data for the spatial and temporal kinematic parameters.

4.2 Introduction

New Zealand's tectonic setting is unique in the sense that it is characterized by two subduction systems: 1) in the North Island the Pacific Plate subducts obliquely under the Australian Plate known as the Hikurangi subduction zone; 2) the central South Island is dominated by oblique convergence, whereas the southern part of this island experiences eastward subduction of the Australian Plate (Kaiser et al., 2012). Furthermore, the majority of the relative plate motion in the central South Island is taken up along the transpressional plate-boundary: the Alpine Fault. The Marlborough fault system (MFS) makes up part of the transition from the Hikurangi subduction zone to convergence in the South Island (Kaiser et al., 2017). The M_W 7.8 Kaikoura earthquake occurred on November 14th 2016 along the east coast of the upper South Island, New Zealand. Available information indicated that this earthquake involved multiple fault segments of the Marlborough fault system (MFS) as the rupture propagated northwards for more than 150 km (Figure 1). However, the exact number of involved fault segments is still debated. Geodetic data show that 21 faults ruptured from the southwest to the northeast of the MFS (e.g. Litchfield et al., 2016; Hamling et al., 2017; Clark et al., 2017). On the other hand, Nicol et al. (2018) documented the surface rupture characteristics, e.g. fault scarps, and determined that the Kaikoura earthquake produced significant displacement at the ground surface on 17 active faults.

Several groups have investigated the complex faulting during the Kaikoura earthquake using a myriad of data sets and methods: field observations, seismic waveforms, InSAR and geodetic data, and tsunami recordings. First, a large nondouble-couple component

was present in the GCMT and USGS *W*-phase moment tensors suggesting that multiple faults within the MFS ruptured during the Kaikoura earthquake. Overall the composite focal mechanism indicated that both right-lateral and thrust slip occurred. Duputel & Rivera (2017) used long-period teleseismic data and a four-point-source model. They determined that the earthquake initiated as a small strike-slip rupture followed by the largest moment release after ~60 seconds. Hollingsworth et al. (2017) calculated a finite source kinematic model from the back-projection of teleseismic P waves. They use two faults in their model: the Kekerengu fault and a deeper, low-angle offshore fault to satisfy the long-period seismic data.

As an added complication, the subducted Pacific plate to the north has been found to extend beneath the South Island (Eberhart-Phillips & Bannister, 2010). It is possible that slip occurred on this subduction interface during the Kaikoura earthquake; another possibility is that slip occurred on a large shallow-dipping thrust fault that extends just below the shallow strike-slip crustal faults. Tsunami records were combined with teleseismic data in Bai et al. (2017) and Furlong & Herman (2017) who proposed that the major source of the tsunami (5 m run-up on the Bank Peninsula) is caused by slip on the megathrust fault below the crustal fault system.

This region has dense geodetic and strong motion networks. Satellite radar data can be acquired from the European Space Agency's C-band Sentinel-1 spacecraft paths and the Japan Aerospace Exploration Agency L-band Advanced Land Observing Satellite-2 (ALOS-2) paths. Both the ascending and descending interferograms maintain good coherence across most of the area, with maximum line-of-sight (LOS) changes of ~-3-1.3

m in the descending and ascending tracks, respectively (Hamling et al., 2017). The Institute of Geological and Nuclear Sciences (GNS) in New Zealand operates 162 3-component accelerograms in the region, providing valuable near-field seismic observations. The previous analyses based solely on the local data did not support the co-seismic rupture along the plate interface. Hamling et al. (2017) used GPS and InSAR data and provided two different models, one with 19 crustal fault segments and another with an additional 20th segment representing the subduction interface. The surface displacements could be fit reasonably well with both models, however the models had trouble modeling the tsunami waveforms. However, Clark et al. (2017) indicated that the tsunami excitation and coastal uplift data can be explained by the co-seismic rupture on an offshore low-angle thrust fault, the Point Kean fault. The existence of the Point Kean fault, which was previously unmapped and had a large inverted offset of 6-8 m (e.g., Clark et al., 2017; Kääb et al., 2017), is also consistent with the relocated aftershock distribution (Cesca et al., 2017). Seismologically, Holden et al. (2017) demonstrated that high-rate GPS and local strong motion observations can be well modeled with slip only on the crustal fault. They then argued that the Hikurangi subduction thrust most likely did not slip during the rupture event. However, the scenario of coseismic rupture on the Hikurangi subduction interface also cannot be completely ruled out (Clark et al., 2017; Cesca et al., 2017; Holden et al., 2018; Xu et al., 2018). For example, using geodetic data only, Xu et al. (2018) presented 3 different finite fault models: the first with only crustal inland fault segments, the second with crustal inland fault segments and the subduction interface, and the third with crustal inland fault segments and the Point Kean fault. They concluded that the estimated slip on the subduction interface or on the Point Kean fault could not be reliably constrained.

Efforts have also been made using both local and teleseismic observations. Cesca et al., (2017) further showed that a multi-fault segment model consisting of such a shallow dipping thrust fault with large slip connected to two shallow strike-slip faults can explain the GPS and teleseismic body wave waveforms well. In contrast, Wang et al. (2018) studied this earthquake with a joint inversion of the waveforms of local strong motion observations, teleseismic body waves, GPS vectors and INSAR images. They found that almost half (45%) of the released moment is distributed on the subduction interface. However, Wang et al. (2018) didn't take the Point Kean fault into consideration.

The Papatea fault is another important fault with a surface uplift up to 8 m (Clark et al., 2017). Early studies such as Hamling et al. (2017) and Clark et al. (2017) could not recreate the deformation pattern observed around the Papatea fault using an elastic earth model. They attribute the observed pattern to anelastic deformation within a fault-restraining bend. As such, they do not include it in their slip inversions. Holden et al. (2017) used various tests in an attempt to isolate the impact of slip on this fault had on the local waveforms and found it had a minor contribution despite its large slip value. They partially attribute this result to the fact that there are no nearby seismic or high-rate GPS stations around the Papatea fault. Also, this fault has a complicated geometry and is difficult to represent as a single plane. This contributes to the uncertainty of modeled rupture on this fault. Recently, Xu et al. (2018) and Wang et al. (2018) demonstrated that the large static deformation on the surface could be modeled with elastic dislocation on this fault; they found up to 18 m of slip at shallow depths near the intersection of the

Papatea fault and Kekerengu fault. However, in the model of Xu et al. (2018), the thrust motion dominates the rupture of this fault, but in the model of Wang et al. (2018) it is mainly a strike-slip fault.

In short, despite many sophisticated modeling approaches, and the availability of GPS, InSAR, teleseismic, and strong motion data, there is still a large debate about whether or not slip occurred on the Hikurangi subduction zone. From the published models, results show that the inclusion of slip on the subduction interface generally improves the fit to long-period seismic and tsunami data, while geodetic data and strong motion observations can be well modeled with just a shallow crustal fault system. Furthermore, the temporal rupture sequence of these fault segments depends heavily on whether a crustal fault system is used versus a crustal and interface fault system. Knowledge of the kinematics of complex fault interactions has important implications for our understanding of global seismic hazards, particularly in the modeling of multisegment ruptures. Understanding the Kaikoura earthquake will hopefully provide insight into how one incorporates multi-fault ruptures in seismic-hazard models.

The one common thread of all these published studies is that the M_w 7.8 Kaikoura earthquake is highly complex and that fault systems involving diverse orientations, slip directions, and intricate mechanical linkages can produce lengthy and highly energetic ruptures. A clear rupture sequence and timing has yet to be agreed upon. Here our study is composed of two parts. First, we apply a multiple double-couple inversion (MDC) to constrain the centroid time and seismic moment of a static fault model (Clark et al., 2017) with long period strong motion observations. The results are then used to forward predict

the long period seismic data. Second, we conduct a finite fault inversion on a crustal fault system consisting of 10 different fault segments to determine a more detailed spatiotemporal slip history, using both seismic and geodetic data. Campaign and continuous GPS data will also be jointly inverted for with the local seismic data. With these combined results, we include in our study a discussion on the potential role of the Hikurangi subduction zone.

4.3 Data Processing

In this study we use three different datasets. First, we selected 16 three-component strong motion stations within 110 km of the fault plane sequence. All waveforms were integrated to velocity and down-sampled to dt = 0.25 seconds. During the multiple double-couple (MDC) analysis, the data are further band-passed between 10 and 50 seconds. For the finite fault inversion the data are band-passed between 2 and 50 seconds.

Second, we use the vertical and transverse components of 26 displacement waveforms at teleseismic distances that are band-passed between 166.67 and 250 seconds. Our Earth model of the teleseismic data is the 1D Preliminary Reference Earth Model (PREM, Dziewonski & Anderson, 1981). Initially, we used waveforms from more than 40 stations in our inversions. However, we noticed in the first set of teleseismic results that the timing and alignment of the synthetics and the centroid locations were consistently erroneous.

To correct the alignment and centroid locations we modeled a M_w 6.4 aftershock that also occurred on November 14th (the distance between mainshock and aftershock epicenters is

20 km) to recalibrate the data that we used in the inversions of the mainshock. Generally, in inversion modeling there are two sets of unknowns: one is the source and the other is the Earth structure. To reduce the impact of the inaccurate Earth structure in the modeling of the source, we correct for the path effects. For this reason, we didn't invert for the focal mechanism and location of the aftershock. Instead we assumed the hypocentral location given by GNS is correct, and then used it to forward predict the synthetic seismograms at the selected stations. If the Earth model along one source to station pair is correct, the synthetic seismogram will match the observations. Usually this is not the case, but the match can be improved by slightly time-shifting the observations. This time-shift is viewed as the correction to the inaccurate Earth structure and applied to the data of the mainshock. However, the drawback of applying this method is it strongly limits the number of waveforms that can be used. Hence the reason we only consider 16 stations.

4.4 Multiple Double-Couple Inversion

4.4.1 Methods

For rupture on such a complex causative fault system, it is a challenge to define the fault geometry. First, we attempt to solve this problem by using a Multiple Double-Couple inversion approach (MDC) (Li et al., 2014). In general this involves approximating an earthquake as a summation of multiple subevents, i.e. double-couples, and then inverting for their magnitude and location.

Due to the use of 1D synthetic seismograms, we model the subevents as double-couples rather than as full moment tensors. Henry et al. (2002) demonstrated that spurious large

non-double-couple components obtained in inversions for the full deviatoric moment tensor for shallow crustal earthquakes can be obtained as the result of inaccurate Earth models. This typical "best double-couple" solution does not generally provide the optimal estimate of a double-couple mechanism, and is only consistent when the non-double-couple component of the full deviatoric solution is small. Due to the dominant double-couple mechanism of common crustal, tectonic earthquakes and the normal error involved in using 1D Earth models to generate the synthetic Earth response, we choose to approximate each subevent, or the source of moment release for each fault segment in this case, as a double-couple rather than a full deviatoric moment tensor.

Using this approach, each subevent is represented by a total of nine parameters characterizing its fault geometry (strike, dip and rake), seismic moment, centroid time, half-duration, and location (latitude, longitude and depth). The half-duration (t_h) is often not well constrained. Here we set the half-duration by the empirical relationship: $t_h = 2.26\times10^{-6} * M_0^{1/3}$, where M_0 is the inverted seismic moment in Nm (Ekström et al., 2005). Thus, the number of independent variables of each point source is 8. We use relatively long period seismic data recorded at local or distant stations, and use a combination of L1 and L2 norms to calculate the misfit between data and synthetic seismograms in the wavelet domain (Ji et al., 2002). We search for the MDC model associated with the minimum of the objective function using the simulated annealing algorithm.

4.4.2 Inversions using only teleseismic long period data

The first set of tests conducted was simply trying to reproduce only the teleseismic long period data with a variable number of point sources; stations used are shown in Figure 3a. In other words, we progressively increased the number of point sources used in the MDC inversion until the additional source could not produce significant improvement to the observations. Inversions were done with 1-5 sources, allowing a combination of the geometry, location, and timing to vary.

After many tests, the results were inconclusive as there was no resolution beyond a two-point source model (Figure 2). Using just the long-period teleseismic data, a model with 2 or 3 sources produced only marginal differences in the resolution of the far-field data and could not illuminate the complexity of this earthquake. Figure 3c and 3d show the locations and focal mechanisms of the 2-source model (misfit = 0.756) and 3-source model (misfit = 0.652), respectively.

Both models place sources in the far southwest and northeast of the MFS and miss the middle Kekerengu fault section. Interestingly, the 3-source model places a source of energy on the Point Kean fault. The moment rate functions for both models (Figure 3b) show two very different rupture patterns. The 2-source model has the largest moment release within the first 20 seconds; whereas the 3-source model does not produce any energy release in this time interval. Both models show a similar peak between ~55-80 seconds. The cumulative moment (tensor summation) of the 2-point source model is high 1.32×10^{21} Nm (M_w 8.01). The seismic moment of the 3-point source model is only slightly lower at 1.03×10^{21} Nm (M_w 7.94). Thus, looking at Figures 2 and 3, we can see that the results from both the 2- and 3-source models are significantly variable. Most

striking perhaps are the cumulative focal mechanisms for both of these models: mostly thrust motion with a high non-double couple component (ε = -0.29 for the 2-source model and -0.45 for the 3-source model). Neither model resembles the GCMT solution. Considering these results, it is difficult to differentiate between models. Moreover, the main locations of slip for either model is not well constrained.

4.4.3 Inversions using both the long period strong motion and teleseismic data

Due to the lack of resolution from long-period teleseismic seismograms, we will not discuss the tests discussed in section 3.2 in the subsequent sections. We will only consider the following MDC inversion tests using strong motion data, and the finite fault inversion tests using both strong motion and geodetic data to increase our resolution of this rupture event.

As mentioned previously, Hamling et al. (2017) developed a model using geodetic data that involved 19/20 faults. Using the same method described in Hamling et al. (2017), Clark et al. (2017) later updated this model by including a refined fault geometry, adding the Point Kean fault, incorporating the new Lidar measurements of coastal deformation and including vertical uplift data for offshore faults.

We use the fault geometry and results from Clark et al. (2017) because they used as complete a geodetic dataset as possible. We assume that this data type can constrain the fault locations and geometries most accurately. However, these types of models lack the timing element and cannot produce a rupture sequence. Hence, in our approach, we fix the fault geometry but invert for the centroid time, allowing a rapid inversion and

focusing on the less well-constrained element of the rupture event. It is important to note that this approach has its disadvantages: namely that any error present in the model of Clark et al. (2017) will of course propagate through our inversions as well. Because we treat the slip on each fault segment as a point source with a fixed shape for the moment rate function, the detailed short period waveforms cannot be properly matched. We therefore choose a period range of 10-50 seconds for the MDC inversions. In order to tackle this challenge, we consider finite fault inversions in section 4.

Figure 4 shows the surface projections of 20/21 fault segments Clark et al. (2017). The number of faults depends on inclusion of an interface source. Their best-fitting slip model consists of each fault segment represented as an individual finite fault source, which has then been divided into a series of subfaults, each with its own slip value. Using these results we estimate the cumulative seismic moment, focal mechanism and centroid location of each fault segment. The total seismic moment of the Clark et al. (2017) model is 8.0 x 10^{20} Nm, M_w 7.87. Out of their 21 fault segments, eight have an individual M_w larger than 7.0. The plate interface subevent has a moment of 6.62x10^{19} Nm (M_w 7.1), making up 8.3% of the total cumulative seismic moment.

We determine the centroid location, i.e. the latitude, longitude and depth, for each fault segment by averaging the location of each subfault weighted by the slip in the subfault. We plot the focal mechanism for each centroid location on the surface projection of each fault segment sized with their relative contribution to the overall seismic moment (Figure 4). In the case without a subduction interface, we have 20 fault segments resulting in 8 parameters*20 fault segments = 160 unknowns. Note we have 8 parameters and not 9

because we calculate the half-duration based on the seismic moment. In the second case, which includes a large fault for the Hikurangi subduction interface, we have 8*21 = 168 unknowns. Using the FK code (Zhu & Rivera, 2002) we have constructed a 1D Green's function lookup table. In this table, the hypocenter depth changes from 1 km to 40 km with a spatial interval of 2 km; the horizontal range varies from 0 to 300 km, with a spatial interval of 0.5 km.

Inverting for the geometry, moment, and centroid time of each fault segment leads to a large number of unknowns: so we invert for only a subset of all parameters. First, we consider just the crustal fault system (20 fault segments) and ask whether or not we can reproduce the strong motion waveforms by inverting for just the centroid time – hereafter we call Case 1. Thus, we fix the fault geometry and centroid location. This reduces the number of unknowns to 20. The centroid time for each of the point sources is shown in Table 1. Case 2, adds an additional unknown the seismic moment, M_0, bringing the total number of unknowns to 40. Seismic moment for each fault segment is allowed to vary ±40% from the corresponding values of the geodetic models. Because the geodetic data, such as INSAR and campaign GPS, includes the post-seismic deformation, the model based on geodetic data might over-predict the co-seismic rupture. Of course, due to the complexity of the tectonic setting of the MFS, an important question is whether there are other sources of slip, namely the subduction interface? Including an interface source, Case 3 is equivalent to Case 1 and Case 4 is equivalent to Case 2. The natural question is whether incorporating this subduction interface fault segment improves the waveform fit.

An important result from Hamling et al. (2017) is that using only geodetic data they cannot distinguish between models with or without the added subduction interface. Furthermore, static tests do not shed light on timing and so the temporal distribution of the fault rupture is still unclear. Using the updated fault geometry from Clark et al. (2017) and our MDC inversion approach, we attempt to determine a rupture timing sequence for the Kaikoura earthquake. It is unknown whether all 20 fault segments ruptured co-seismically. It is also unknown whether slip on the subduction interface explains the far-field seismic, strong motion and geodetic data better than just the crustal faults.

4.4.4 Comparison of Case 1 and Case 3

The waveform misfits for the four cases are given in Table 1. The largest misfit (0.283) is for Case 1, and the smallest misfit (0.251) is for Case 4. Regardless of the number of fault segments (20 or 21) allowing the seismic moment to vary produces a smaller misfit. Models that incorporate an interface also have a lower misfit than the ones without, i.e. Case 1 versus Case 3, and Case 2 versus Case 4, resulting in a better fit to the strong motion waveforms.

Considering Case 1 and Case 3, i.e. the Clark et al. (2017) model with just the added time parameter, we would like to answer the question whether slip on the interface is significant or not. The fit to the waveforms visually increases, Figure 6. In particular, the later pulse in station SCAC and GVZ, and the amplitude of peaks at station LTZ are better predicted by Case 3 than in Case 1. The misfit from Case 1 to Case 3 decreases by only 1.6%; however the number of unknowns between cases increases by 5% (from 20 to

21 because of the addition of the timing of the interface). This decrease in the misfit is not significant. On the other hand, this slight difference in misfit may only indicate the lack of resolution of the local dataset to the deep rupture and cannot disprove the existence of any interface rupture.

Once we have the timing, location and moment of each point source determined from the inversions using the strong motion data, we can use these parameters as constraints to conduct a forward prediction of the teleseismic long-period data (Figure 8). Case 1 and Case 3 tend to slightly over-predict the waveforms, e.g. stations SBA, JOHN and QSPA (Figure 8a and 8b). The difference between these fits is marginal; one can say that Case 3 approximates the waveform peaks slightly better at stations PMG, TATO and QIZ.

Comparing the cumulative moment rate functions for Case 1 and Case 3 (Figure 9a) we can see that these two cases produce similar moment rate patterns: energy is released in three large bursts. Faults 1-6 rupture in the first 20 seconds, are the most southwestern faults in the crustal system, Faults 7-10 have a rupture time of ~20-40 seconds, and help in the transmission of the energy from the earthquake source to the long Kekerengu fault zone to the northeast, where the majority of the energy is released. The peak moment rate occurs at ~70 seconds with the largest slip pulse between 40 and 80 seconds coming predominantly from faults 11-18. This makes up ~84% of the total seismic moment.

Figure 4a shows the multiple double-couple results for the complex fault system of Case 3. On the map, the focal mechanisms for each fault segment are sized relative to their contribution to the overall moment. Note, the focal map for Case 1 is not shown because

it is the same as Case 3 (minus the interface fault segment, fault 21), as the only difference between these two cases is the timing, which is not shown in this plot. The cumulative moment for Case 1 is 6.09×10^{20} Nm (equivalent to M_w 7.79), and for Case 3 is 6.24×10^{20} Nm (M_w 7.8), which are 10% and 7.4% lower than the Global CMT value of 6.7×10^{20} Nm, respectively. This value of the total seismic moment is the tensor summation of all components of all 20 or 21 fault segments, i.e., the total moment is calculated from the piecewise addition of all the moment tensor components for each subevent. This could lead to an underestimation of the total seismic moment because of the cancellation with some of the negative components. On the other hand, the total scalar seismic moment for Case 1 is 7.3×10^{20} Nm (M_w 7.84) and for Case 3 it is 8.01×10^{20} Nm (M_w 7.87) — 8.2% and 16.4% higher than the Global CMT value. The moment of the interface source in Case 3 is 6.69×10^{19} Nm, only 8% of the total cumulative moment.

The cumulative focal mechanism for Case 3 is also plotted in Figure 4a and compared to the Global CMT solution, which has a significant non-double-couple component. Case 1 and Case 3 also exhibit a large non-double component with a value of ε equal to -0.0813 and -0.1423, respectively. Further examining the rupture process, the southwest portion of the MFS is dominated by thrust motion, and releases only a small portion of the total moment. The coastal and offshore faults also are dominated by thrust motion. This then transitions into strong strike-slip motion in the northeast, where the largest amount of moment is released.

Table 2a and 2b lists the values for the fault geometry, centroid location, and inverted rupture timing and seismic moment for Cases 1 and 3, respectively. Figure 5a illustrates

the individual moment rate functions for each subevent for Case 1 and 3. Faults 14-18 exhibit the largest moment rates and rupture between ~55-80 seconds. Fault 12, the offshore Point Kean fault, has a centroid time of ~52 seconds and makes a considerable contribution to the total energy released, ~9%. The interface source provides considerable moment and with a centroid time of 67 seconds ruptures within the same time interval as the faults in the Kekerengu-Needles fault sequence, Faults 14-18, between ~60-80 seconds. The difference in moment rate between Case 1 and Case 3 is marginal for most fault segments except for Faults 11 and 13, which have a minimal contribution to the overall moment. These two faults both rupture ~20 seconds later in Case 3 than in Case 1. This is interesting, as this fault segment is the transition to the initial part of the large Kekerengu-Needles fault line, where the majority of the energy of this event is released. This could suggest that in the case with the subduction interface, this large fault rupture sequence in the northeast has a delayed rupture time, or in the case without the interface it suggests that there is a more rapid energy transfer from the southeastern fault segments to the northeast.

4.4.5 Comparison of Case 2 and Case 4

Next, we consider the same cases as in section 3.4, except with the added variation in the seismic moment. It might allow us to explore whether there is significant postseismic deformation present in the geodetic models and whether the strong motion data requires more slip on the plate interface. Case 2 has 40 unknown parameters and Case 4 has 42. Here the misfit decreases from 0.25889 to 0.25134, a 2.9% decrease. As expected, the cases that inverted for centroid time and M_o generally produced better results than the cases that only inverted for centroid time when comparing Case 1 to 2 and Case 3 to 4.

When the seismic moment can be perturbed, the waveform fits can be significantly improved (Figure 7). For most stations, the synthetics in both cases do a good job of matching the observations; a few exceptions are stations WTMC, CECS, KIKS, and KEKS. The early pulse of station WTMC is not well fit by the synthetics; this could be due to the station's proximity to the hypocenter of the event. Similarly, the large pulse at station KIKS is not re-created by the synthetics, despite the addition of the offshore Point Kean fault. With the additional moment added from the interface source in Case 4, the later peaks of the waveforms are slightly better fit than in Case 2, e.g. stations SCAC and SJFS. Generally, the stations with the largest misfit are located near the surface break of fault segments, where the impact of fault finiteness is more significant.

Now, in all four cases, considerable misfit can be seen. This is largely due to the fact that we are approximating sizeable fault segments as a single point source. Inevitably, this simplification will lead to a lack of higher frequency information in the predictions. Furthermore, there will be additional error introduced in the solution for Case 3 and 4 because we are approximating a large fault segment on the subduction interface by a single point source.

Case 2 and Case 4 produce somewhat different predictions of the far-field data (Figure 8c and Figure 8d, respectively). In general, these two cases tend to under-predict the teleseismic data as compared to Cases 1 and 3. Interestingly, when the moment is allowed to vary, the results with the addition of the interface source, Case 4, tend to under-predict the teleseismic data at stations VNDA, SBA, QSPA as compared to Case 2. Thus, it is

still difficult to confidently say that a significant amount of slip occurred on the Hikurangi thrust as we get under- and over-predictions of the far-field data between all cases studied.

Figure 9b illustrates the cumulative moment rate for Case 2 and Case 4. Similar to the previous 2 cases, there are 3 large bursts of energy, with the predominant moment release between 40 and 80 seconds. The addition of varying the moment, i.e. from Cases 1&3 to Cases 2&4, does not change the pattern of energy release. However, it can be seen that when the moment is allowed to vary, the highest peak at ~70 seconds is less than the previous cases, i.e., Case 3 peaks at ~$7x10^{19}$ Nm/sec and Case 4 at ~$6x10^{19}$ Nm/sec.

This phenomenon can also be seen in Figure 10, which explores the effect of allowing more variation in the seismic moments determined from purely static data. A comparison of the individual moments of each of the 20 subevents is given in Figure 10a, and the 21 subevents in Figure 10b. For almost every single fault segment, when inverting for the seismic moment (Cases 2 & 4) this source parameter decreased from the values that were determined using the static model and left unchanged (Cases 1 & 3). The most drastic changes were found in the faults in the northeastern section: the Kekerengu and Needles faults, or Faults 14-18. The search range for the seismic moment in Cases 2&4 is ±40% from the values in Cases 1&3. And in general, considering the significant changes in subevent moments in Figures 10a and 10b, and the decrease in misfit, it suggests that the seismic moments determined from geodesy are not necessarily the optimal values to fit the strong motion data and forward predict the teleseismic data. When the moment is

allowed to change we see a decent improvement in the misfit between cases, 8.5-9.7% for Case 1 to 2 and Case 3 to 4, respectively.

Figure 4b and 4c show the distribution of the focal mechanisms of the different subevents for Case 2 and Case 4. First the cumulative seismic moments for these two cases are 4.24×10^{20} Nm (M_w 7.68) and 4.49×10^{20} Nm for Case 4 (M_w 7.7), respectively, which are approximately 65% that of the Global CMT solution (6.7×10^{20}). The scalar summation cumulative moments for these two cases are much more similar to the GCMT model at 5.16×10^{20} Nm (M_w 7.74) for Case 2 and for Case 4 it is 6.06×10^{20} Nm (M_w 7.79). Similarly, these two cases have considerable non-double couple components with ε equal to -0.10 and -0.21, respectively. Looking at the maps, we can see that in general, the distribution of focal mechanisms are similar throughout all the cases with thrust motion in the southwest progressing to strike-slip motion in the northeast. However, the differences in the relative sizes of the beach balls between Case 2 and Case 4 are noticeable, especially in Faults 15 and 12. The moment of the interface source in Case 4 is 9.27×10^{20} Nm, 39% larger than in Case 3. But this is still only 15% of the inverted cumulative seismic moment.

The decrease in seismic moment from Case 1 to Case 2 or Case 3 to Case 4 could be interpreted as the presence of significant postseismic deformation included in the geodetic data. However, in view of the large difference in seismic moment between models based on strong motion data and global CMT, we think it is more plausible to explain it as the result of the poor sensitivity of local strong motion data to the total

seismic moment (Shao et al., 2011). It is then important to include the long period teleseismic data into the study of this large event.

Finally, inversion results for the source properties of each subevent for Case 2 and Case 4 are given in Tables 2c and 2d. Examining the individual moment rate functions for these two cases (Figure 5b) we can see that for almost all subevents the rupture initiation time is not significantly different between the two cases. The largest contribution comes from Faults 14-18, along the Kekerengu-Needles fault segment, which is consistent with the size of the beach balls in Figure 4b and 4c, and Fault 12, the Point Kean fault. In this case, the Point Kean fault also has a centroid time of 52 seconds; the interface source in Case 4 ruptures between 60 and 80 seconds.

4.5 Preliminary Results of the Finite Fault Inversion

For the last set of analyses, we explore the complexity of this rupture event in even finer detail with a finite fault inversion strategy to understand the spatiotemporal slip pattern on this complex fault system. We conduct two inversion tests: first, we use strong motion data only (which we call case FF1), and secondly, we jointly invert for strong motion and GPS data (FF2).

4.5.1 Methods

To better understand the complex rupture pattern we implement a finite fault model to describe the coseismic displacement. For this model we use rectangular fault segments of different lengths and widths and various orientations to approximate the ruptured faults.

Each fault segment is then further divided into 3.5 km by 4 km subfaults and we invert for slip amplitude, rake angle, and rise time. Ten fault segments are chosen to approximate this complex earthquake; details of the fault segments are given in Table 3. Note that the fault dimensions of Faults 2 and 6 are different in models FF1 and FF2. Because the results of FF1 showed considerable slip near fault edges, we extend those two fault planes in FF2 accordingly to explore the true edge of the slip asperities. The geometry of the fault segments is designed to represent the main faults shown in Figure 1: the Humps fault at the initiation of the source, then branching into the Hundalee fault, before moving into the large southwest to northeast system of the Kekerengu and Needles faults. In this test, we have not included a fault segment for the Hikurangi subduction interface. Instead we have implemented an offshore shallow dipping, ~35^{o}, relatively long fault (length = 35 km and width = 48 km) to approximate the Point Kean fault (Clark et al., 2017; Holden et al., 2017; Xu et al., 2018). This fault geometry is based on the aftershock distribution (e.g., Cesca et al., 2017), and its relation to the structure of the Papatea fault.

We use four different datasets to constrain the fault model. As the source of this earthquake is now represented with more details compared to the above MDC analysis, i.e. we have more parameters on the fault due to discretization, seismic signals with higher frequency content can be used to constrain the free parameters. Velocity waveforms from the selected sixteen strong motion stations are used after applying a bandpass filter from 0.02 Hz to 0.5 Hz. We also use the GPS coseismic vectors at 20 continuous and 64 campaign sites (Hamling et al., 2017). Finally, we selected the

broadband waveforms of 51 P and SH waves, as well as the transverse and vertical components of 65 long period whole waveforms at teleseismic stations.

We then invert for the slip history on each fault segment using the inversion method described in Ji et al. (2002) by minimizing the difference between the observations and the synthetics in the wavelet domain.

4.5.2 Results

Figures 13 and 16a illustrate the comparison between the observed velocity strong motion waveforms and the synthetic predictions for FF1 and FF2, respectively. Both models fit the strong motion data nearly equally well, though both FF1 and FF2 do not reproduce the early pulse at stations WTMC and CULC, suggesting that the fault geometry near the rupture initiation needs to be further improved. The model cannot explain the high frequency information at station CECS, likely due to the inaccurate velocity structure.

Furthermore, Figure 16b shows the comparison of the synthetic waveforms produced by FF2 and the broadband P and SH waveforms at teleseismic distances. The majority of the P waves are fit quite well, however the later pulse, at ~80-100 s, of the SH waves is generally not as well reproduced. Finally, Figure 16c shows that the transverse component of the teleseismic waves is consistently replicated, except for station JOHN. On the other hand, model FF2 systematically under-predicts the amplitude of the vertical component at stations to the north-northeast, such as MIDW, FUNA, WAKE and TARA.

Now, while including the static offsets in the inversion does not greatly affect the prediction of the strong motion data (Figure 13 versus Figure 16a), it does alter the resulting slip distribution. Figure 11 shows the finite fault slip distribution for case FF1—the inversion done using just strong motion data. Slip originates in the southwest on the Humps fault before progressing northeast towards the Kekerengu and Needles faults. The strongest slip is in the northeast portion of the fault system. The maximum slip, 11.5 m, occurs near station KEKS on the Kekerengu fault, Fault 9.

Figure 12 allows us to examine the slip distribution of FF1 in more detail. We have broken down the rupture sequence into four groups of fault segments. In the first group, near the hypocenter, there is a maximum of ~8 m of slip on Fault 2. The following group has a minor amount of slip in the shallower portions of Faults 4 and 5. The northeastern section, Faults 8-10, shows large slip asperities again in the shallower portion of the faults. The fourth group of fault segments consists of the Point Kean fault and the Papatea fault, Faults 6 and 7 respectively. The largest slip asperity on the Point Kean fault is near the deepest portion of the fault and ruptures from 60-80 seconds (Figure 12b). The Papatea fault has its largest dislocation in the shallower half but also ruptures predominantly between 60-80 seconds. Faults 8 and 10 are the other largest sources of energy for this rupture event and also rupture within the time frame of 60-80 seconds. These results are similar to the MDC inversion results in section 3 where the predominant energy release is in this same time interval.

FF2 is the inversion with both seismic and geodetic data. The slip distribution for FF2 is shown in Figure 14. The slip history is similar to FF1 with slip propagating from

southwest to northeast. However, FF2 has a larger peak slip, 15.1 m, occurring on Fault 8, the Jordan-Kekerengu fault. Both FF1 and FF2 show little slip in the Humps fault zone, or near the hypocenter, with a steady increasing slip towards the Kekerengu and Needles fault zones. The cumulative seismic moment release, scalar summation, for FF1 is 7.06×10^{20} Nm (M_w 7.83), which is similar to Case 4 in the MDC inversion results; FF2 is higher at 1.07×10^{21} Nm (M_w 7.95), and based on a vector summation it is $8.37\text{x}10^{20}$ Nm (M_w 7.88).

The surface trace of the newly mapped Point Kean fault is on the outer shelf in ~50 m water depth. Considerable slip on the offshore Point Kean fault is seen in both finite fault models, with a peak slip for this segment of 11.5 m for FF1 and 9.13 m for FF2, and a seismic moment of $1.4 - 2.3\text{x}10^{20}$ Nm (Mw 7.4). Slip is distributed over two asperities (Figure 15a). The shallow asperity has a peak slip of 6.8 m. It is much larger than the result of Clark et al. (2018) (3 m) but consistent with the Model III of Xu et al. (2018). However, our model has an additional deep asperity at a depth of 24 km, which has a peak slip of 9.13 m (FF2). The shallow rupture of this fault initiated at 30 s, consistent with Holden et al. (2017). They included the Point Kean fault in their models and found that it ruptured 31 seconds after the origin time before continuing onto the northern faults. However, the rupture of the deep asperity occurs much later, from 60 s to 80 s (Figure 15b).

For both FF1 and FF2 rupture on the Papatea fault initiates as early as 22 seconds — the earliest allowable value in our search range and ends at about 80 seconds. This fault also releases a relatively large amount of slip, 6.1 m for FF1 and 13 m for FF2, giving it a

cumulative seismic moment of 0.73-1.1x10^{20} Nm (Mw 7.3-7.4), slightly lower than the results of Xu et al. (2018) who found a seismic moment of 1.23x10^{20} Nm. However, the Papatea fault is invisible in the MDC inversion results. Examining Figures 12b and 15b this release of energy occurs over a long time period. The inverted fault slip is slow and steady for nearly a minute. It explains why it is difficult to resolve using strong ground motion data (Holden et al., 2017). The slip models of Xu et al. (2018) using geodetic data feature a maximum thrust slip of 18 m on the shallow part of the Papatea fault near the intersection with the Kekerengu fault, which is significantly higher than our result. Wang et al. (2018) also determined a very high slip of ~12 m on this fault, similar to FF2, but this large slip asperity occurred at a depth of around 5 km.

Comparing these two slip distributions, we see that, in general, FF2 has higher values of slip than FF1, especially on the Papatea fault, as the result of better spatial coverage and broader frequency content by using both seismic and geodetic data. The large slip asperities on the Kekerengu faults vary between both models, but are slightly lower than other published results such as Holden et al. (2017) who show that the Kekerengu fault has a large slip asperity with peak slip ~20 m.

Figures 15a and 15b illustrate the slip distributions and moment rate functions of each individual fault in FF2, helping to examine the timing and location of the largest slip asperities. The majority of the energy release occurs between 60-80 seconds, and is found primarily on faults 6 (Point Kean fault), 8 (Jordan-Kekerengu fault) and 9 (Kekerengu fault). As the earthquake initiates, the first major pulse of energy release occurs on Fault 2 within the first 20 seconds. This then gets transferred to the next block of faults and

Fault 4 shows a fair amount of slip occurring between 20 and 40 seconds. During this time, slip begins to initiate in the shallow regions on the Point Kean fault at ~30 s. Next, there is very little slip occurring anywhere between 50-60 seconds except on the Point Kean fault, deeper than the first asperity, and ever so slightly on Faults 8 and 9. Thus, this time frame could represent the splitting of energy from the Point Kean fault to the Papatea fault and from the Point Kean fault to the Kekerengu faults section. Subsequently, the largest slip asperities occur in the next 20 seconds (from 60-80 s) on the Kekerengu faults and the deepest part of the Point Kean fault, at ~28 km, which is critical and is discussed in the following section. Finally, in the final 20 seconds slip decreases to a negligible amount on Fault 10, before terminating at ~100 s.

Figure 18 illustrates the comparison of the cumulative moment rate functions between FF1 and FF2. Here we can see that the inversion produces a higher moment release when the GPS data are included, again suggesting that there was some postseismic deformation. Similar to the MDC results, there are multiple episodes of large energy release, with the largest one occurring between 60-80 seconds.

The comparison between observed static offsets and synthetics is shown in Figure 17. Both the horizontal component (Figure 17a) and the vertical component (Figure 17b) match the observed static offsets quite well. In Figure 17b we see that just east of the hypocenter there are negative offsets suggesting potential subsidence in this region. Hamling et al. (2017) had difficulty reproducing the static offsets near the Point Kean fault, probably due to their exclusion of this fault in their model. Now, as discussed here, Clark et al. (2017) did include the Point Kean fault in their refined slip model as a NE-

striking reverse fault with ~3 m of predominantly reverse slip extending to depths of 20 km, although relatively poorly constrained at such depths, and found that the inclusion of this fault provided a significantly better fit to the tide gauge data. Clark et al. (2017) also show that the coastal deformation record in general, including the geodetic data near and offshore the Kaikoura peninsula, is consistent with a shallow source on this offshore reverse fault.

4.5.3 Discussion of the role of the subduction interface

Primary questions about the 2016 Kaikoura earthquake are how the different faults ruptured in this complex earthquake, and whether this was a purely crustal event or if the Hikurangi subduction thrust also slipped. In this study we first applied a MDC approach to analyze the role of this plate interface in this rupture event. Next we investigated the finer details of the rupture history of this earthquake by applying a finite fault inversion to a 10-segment crustal fault model.

One of the benefits of the MDC inversion, section 3, is its efficiency and use of fewer unknown parameters. Despite the simplicity of this method, it can still capably deduce important information about the general rupture characteristics. By setting up multiple cases with and without the interface, and inverting for different source parameters, we consistently saw an improvement to the fit of the strong motion waveforms when the interface source was included. Slip on the interface accounted for only ~8% of the entire seismic moment of the Kaikoura earthquake in Clark et al. (2017). Even when we allowed the moment of subevents to change (Case 4), the inverted fault slip on the interface using just strong motion data is still only 15% of the total cumulative seismic

moment. We cannot expect the addition of this source to lead to a significant change in the inverted fault model of the crustal faults. However, despite its minor contribution to the source, it did lead to slightly better predictions of the observations as expected. Thus, we cannot disregard the idea that the interface was involved.

In section 4 we conducted a finite fault inversion of 10 fault segments using strong motion and geodetic data. In this case, we did not include an interface source. However, in Figures 12 and 15 the depth of the large slip asperity on the Point Kean fault, Fault 6, is 25 km. This could be on the subduction interface. This fault segment has a moment of 1.93×10^{20} Nm, M_w 7.46. If we add the moment of the interface source and shallow depth Point Kean fault subevent in the MDC inversion model we get 1.49×10^{20} Nm, which is consistent with our finite fault inversion result. Also, the rupture time of this large asperity on the Point Kean fault corresponds with the centroid time of the interface source in the MDC models, 67 seconds. Furthermore, the Point Kean fault in the MDC inversion has a shallow depth rupturing at ~52 seconds, which is consistent with the rupture time of the second slip asperity on the Point Kean fault in the finite fault inversion.

Thus, despite our different inversion techniques, all of these preliminary results cannot necessarily confirm that the Hikurangi subduction thrust slipped. So the debate continues. The next logical step would be to test our finite fault model with an additional fault plane representing this interface.

4.6 Conclusion

In Part I of this study, we use a multiple-double couple method and seismic data to evaluate the "crustal" and "crustal+interface" slip models constructed with geodetic data by Clark et al. (2017). We estimate the focal mechanisms and centroid locations of subevents directly from the geodetic models and perturb only the centroid time and M_o of each subevent to fit the strong motion data.

Both slip models can explain most bandlimited (0.02 – 0.1 Hz) strong motion data well except for a few stations right in close proximity of the hypocenter and those right on the fault segments. In the second approach, we invert for the spatio-temporal slip history of a ten-segment finite fault model representing the complexity of the Marlborough Fault System. Instead of considering slip on the subduction interface we include the Point Kean fault— a low-angle (dipping 35^o) thrust fault extending to depths of ~28 km. This improves the fit to the data.

So, based on the multitude of tests we can see that just using the MDC inversion approach, we cannot definitively say whether we favor a model that includes the subduction interface. On one hand it does help to consistently improve the fit to the strong motion waveforms, but also, the interface source only marginally contributes to the overall seismic moment, potentially due to the poor sensitivity of local strong motion data to the total seismic moment. In the application of the finite fault models, we show that a model without including the subduction interface can match multiple datasets simultaneously, though the solution has an important contribution from the offshore low-angle dipping Point Kean fault. The inversion of this model with just the strong motion data reproduces the waveforms well but tends to under-estimate the slip that has been

seen in other models and field data. With the inclusion of the geodetic GPS data, we are able to better resolve the slip values that are seen in other studies. We model the static offsets exceptionally well.

4.7 References

Bai, Y., Lay, T., Cheung, K. F., & Ye. (2017). Two regions of seafloor deformation generatedthe tsunami for the 13 November 2016,Kaikoura, New Zealand earthquake. *Geophysical Research Letters*, *44*, 1–10. http://doi.org/10.1002/2017GL073717

Cesca, S., Zhang, Y., Mouslopoulou, V., Wang, R., Saul, J., Savage, M., … Dahm, T. (2017). Complex rupture process of the Mw 7.8, 2016, Kaikoura earthquake, New Zealand, and its aftershock sequence. *Earth and Planetary Science Letters*, *478*, 110–120. http://doi.org/10.1016/j.epsl.2017.08.024

Clark, K. J., Nissen, E. K., Howarth, J. D., Hamling, I. J., Mountjoy, J. J., Ries, W. F., … Strong, D. T. (2017). Highly variable coastal deformation in the 2016 MW7.8 Kaikōura earthquake reflects rupture complexity along a transpressional plate boundary. *Earth and Planetary Science Letters*, *474*, 334–344. http://doi.org/10.1016/j.epsl.2017.06.048

Duputel, Z., & Rivera, L. (2017). Long-period analysis of the 2016 Kaikoura earthquake. *Physics of the Earth and Planetary Interiors*, *265*, 62–66. http://doi.org/10.1016/j.pepi.2017.02.004

Eberhart-Phillips, D., & Bannister, S. (2010). 3-D imaging of Marlborough, New Zealand, subducted plate and strike-slip fault systems. *Geophysical Journal International*, *182*(1), 73–96. http://doi.org/10.1111/j.1365-246X.2010.04621.x

Ekström, G., Dziewoński, A. M., Maternovskaya, N. N., & Nettles, M. (2005). Global seismicity of 2003: Centroid-moment-tensor solutions for 1087 earthquakes. *Physics of the Earth and Planetary Interiors*, *148*(2–4), 327–351. http://doi.org/10.1016/j.pepi.2004.09.006

Furlong, K. P., & Herman, M. (2017). Reconciling the deformational dichotomy of the 2016Mw7.8 Kaikou ra New Zealand earthquake. *Geophysical Research Letters*, *44*, 1–4. http://doi.org/10.1002/2017GL074365

Hamling, I. J., Hreinsdóttir, S., Clark, K., Elliott, J., Liang, C., Fielding, E., … Stirling, M. (2017). Complex multifault rupture during the 2016 Mw 7.8 Kaikōura earthquake, New Zealand. *Science*, *356*(6334). http://doi.org/10.1126/science.aam7194

Henry, C., Woodhouse, J. H., & Das, S. (2002). Stability of earthquake moment tensor inversions: Effect of the double-couple constraint. *Tectonophysics*, *356*(1–3), 115–124. http://doi.org/10.1016/S0040-1951(02)00379-7

Holden, C., Kaneko, Y., D'Anastasio, E., Benites, R., Fry, B., & Hamling, I. J. (2017). The 2016 Kaikōura Earthquake Revealed by Kinematic Source Inversion and Seismic Wavefield Simulations: Slow Rupture Propagation on a Geometrically Complex Crustal Fault Network. *Geophysical Research Letters*, *44*(22), 11,320-11,328. http://doi.org/10.1002/2017GL075301

Hollingsworth, J., Ye, L., & Avouac, J.-P. (2017). Dynamically triggere d slip on a splay fault in the Mw7.8, 2016 Kaikoura (New Zealand) earthquake. *Geophysical Research Letters*, *44*, 3517–3525. http://doi.org/10.1002/2016GL072228

Ji, C., Wald, D. J., & Helmberger, D. V. (2002). Source Description of the 1999 Hector Mine , California , Earthquake , Part I : Wavelet Domain Inversion Theory and Resolution Analysis, *92*(4), 1192–1207.

Kääb, A., Altena, B., & Mascaro, J. (2017). Coseismic displacements of the 14 November 2016 Mw7.8 Kaikoura, New Zealand, earthquake using the Planet optical cubesat constellation. *Natural Hazards and Earth System Sciences*, *17*(5), 627–639.

http://doi.org/10.5194/nhess-17-627-2017

Li, X. and C. Ji (2010), Investigation of long-period characteristics of great earthquakes through multiple point source analysis, presented at *2010 Fall Meeting, AGU*, edited, pp. Abstract S43A-2045, San Francisco, Calif., 13–17 Dec, 2010.

Shao, G., Li, X., Ji, C., and Maeda, T., (2011). Focal mechanism and slip history of the 2011 M_w 9.1 off the Pacific coast of Tohoku Earthquake, constrained with teleseismic body and surface waves. *Earth Planets Space*, 63, doi.org/10.5047/eps.2011.06.028.

Wang, T., Wei, S., Shi, X., Qiu, Q., Li, L., Peng, D., … Barbot, S. (2018). The 2016 Kaikōura earthquake: Simultaneous rupture of the subduction interface and overlying faults. *Earth and Planetary Science Letters*, *482*, 44–51. http://doi.org/10.1016/j.epsl.2017.10.056

Zhu, L., & Rivera, L. A. (2002). A note on the dynamic and static displacements from a point source in multilayered media. *Geophysical Journal International*, *148*, 619–627.

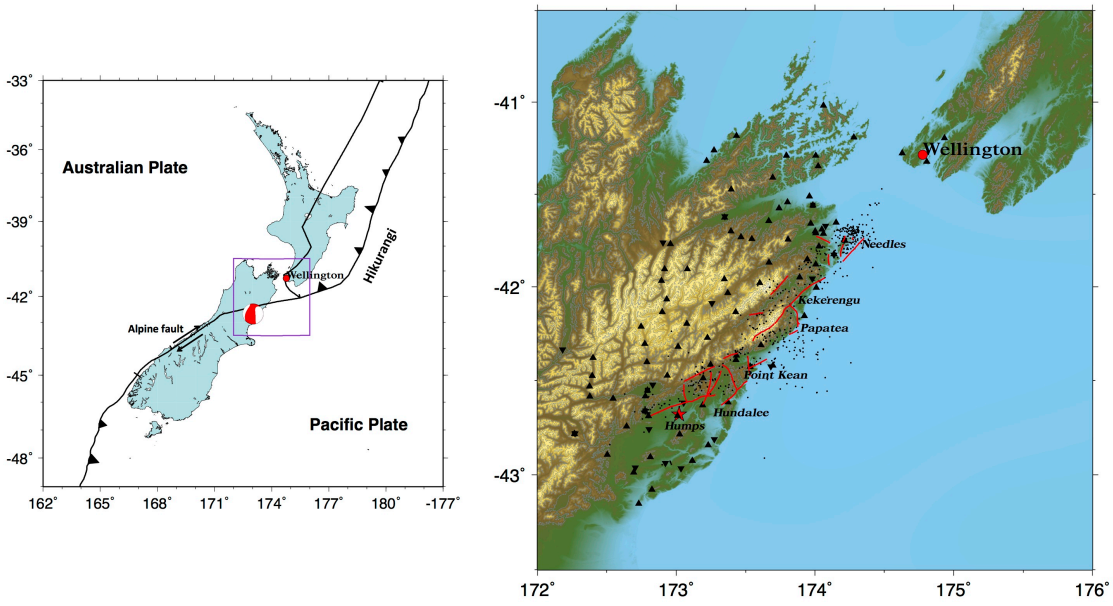

Figure 1: Overview of the tectonic setting of New Zealand (left panel), with the Marlborough Fault System (MFS) outlined in purple. Zoomed in topographic map of the MFS in the northern part of the South Island of New Zealand (right panel). Crustal fault segments are traced in red with the names of the large main faults labeled. The hypocenter of the 2016 Kaikoura earthquake is plotted as a red star and the aftershocks with $M_w > 4$ are plotted as black dots. Strong motion stations are represented by triangles and high-rate GPS stations are plotted as squares.

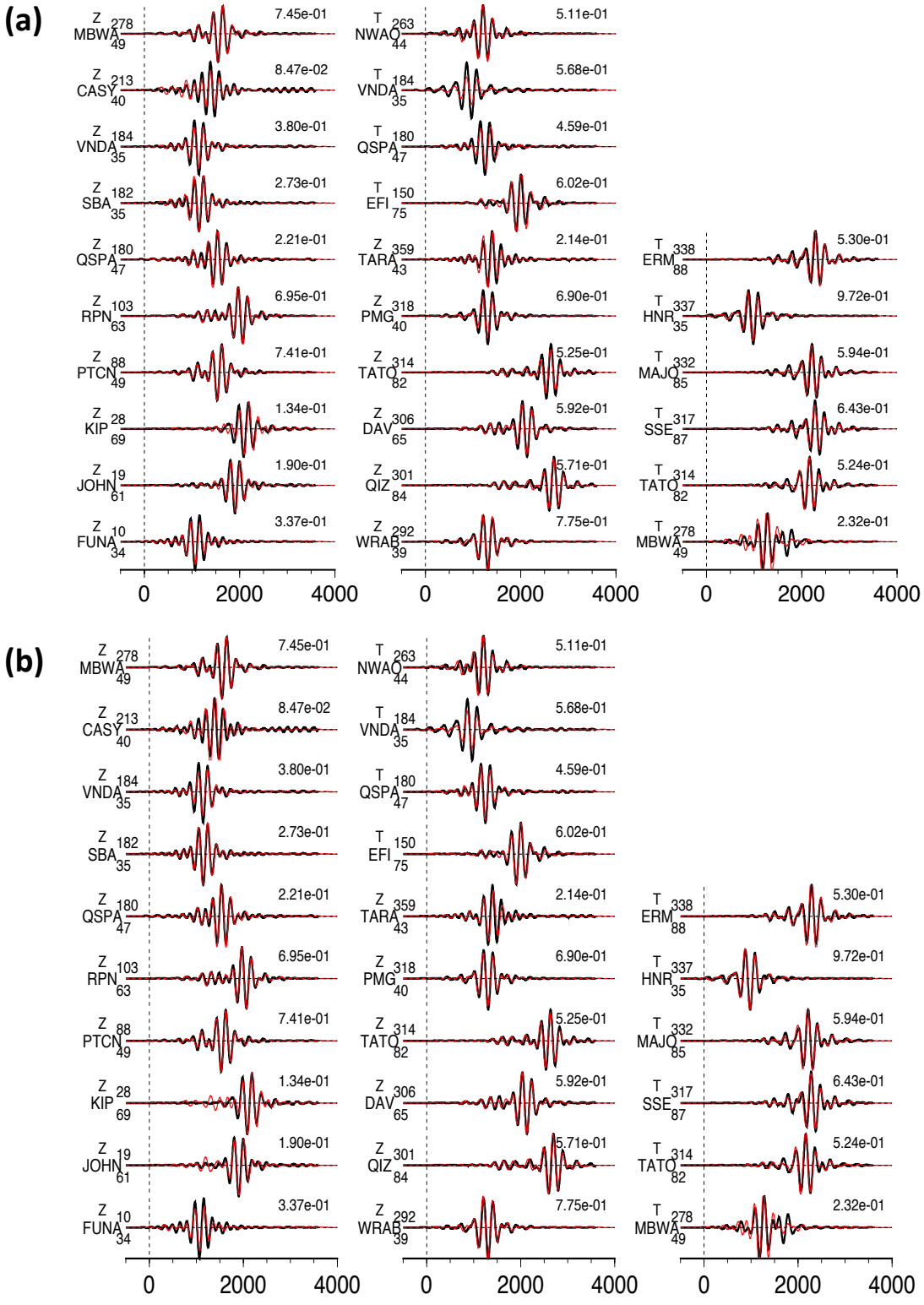
(a)
Z MBWA 278 49 7.45e-01
Z CASY 213 40 8.47e-02
Z VNDA 184 35 3.80e-01
Z SBA 182 35 2.73e-01
Z QSPA 180 47 2.21e-01
Z RPN 103 63 6.95e-01
Z PTCN 88 49 7.41e-01
Z KIP 28 69 1.34e-01
Z JOHN 19 61 1.90e-01
Z FUNA 10 34 3.37e-01
T NWAO 263 44 5.11e-01
T VNDA 184 35 5.68e-01
T QSPA 180 47 4.59e-01
T EFI 150 75 6.02e-01
Z TARA 359 43 2.14e-01
Z PMG 318 40 6.90e-01
Z TATO 314 82 5.25e-01
Z DAV 306 65 5.92e-01
Z QIZ 301 84 5.71e-01
Z WRAB 292 39 7.75e-01
T ERM 338 88 5.30e-01
T HNR 337 35 9.72e-01
T MAJO 332 85 5.94e-01
T SSE 317 87 6.43e-01
T TATO 314 82 5.24e-01
T MBWA 278 49 2.32e-01
0
2000
4000
(b)
Z MBWA 278 49 7.45e-01
Z CASY 213 40 8.47e-02
Z VNDA 184 35 3.80e-01
Z SBA 182 35 2.73e-01
Z QSPA 180 47 2.21e-01
Z RPN 103 63 6.95e-01
Z PTCN 88 49 7.41e-01
Z KIP 28 69 1.34e-01
Z JOHN 19 61 1.90e-01
Z FUNA 10 34 3.37e-01
T NWAO 263 44 5.11e-01
T VNDA 184 35 5.68e-01
T QSPA 180 47 4.59e-01
T EFI 150 75 6.02e-01
Z TARA 359 43 2.14e-01
Z PMG 318 40 6.90e-01
Z TATO 314 82 5.25e-01
Z DAV 306 65 5.92e-01
Z QIZ 301 84 5.71e-01
Z WRAB 292 39 7.75e-01
T ERM 338 88 5.30e-01
T HNR 337 35 9.72e-01
T MAJO 332 85 5.94e-01
T SSE 317 87 6.43e-01
T TATO 314 82 5.24e-01
T MBWA 278 49 2.32e-01
0
2000
4000

Figure 2: Comparison of the vertical and transverse components of 26 teleseismic waveforms (black lines) and synthetic seismograms (red lines) calculated for (a) the 2-point source model, and (b) the 3-point source model. The station names are indicated to the left of the traces, along with the epicenter distances and azimuthal angle in degrees. At the end of the trace, the peak amplitude (mm) of the observation is given.

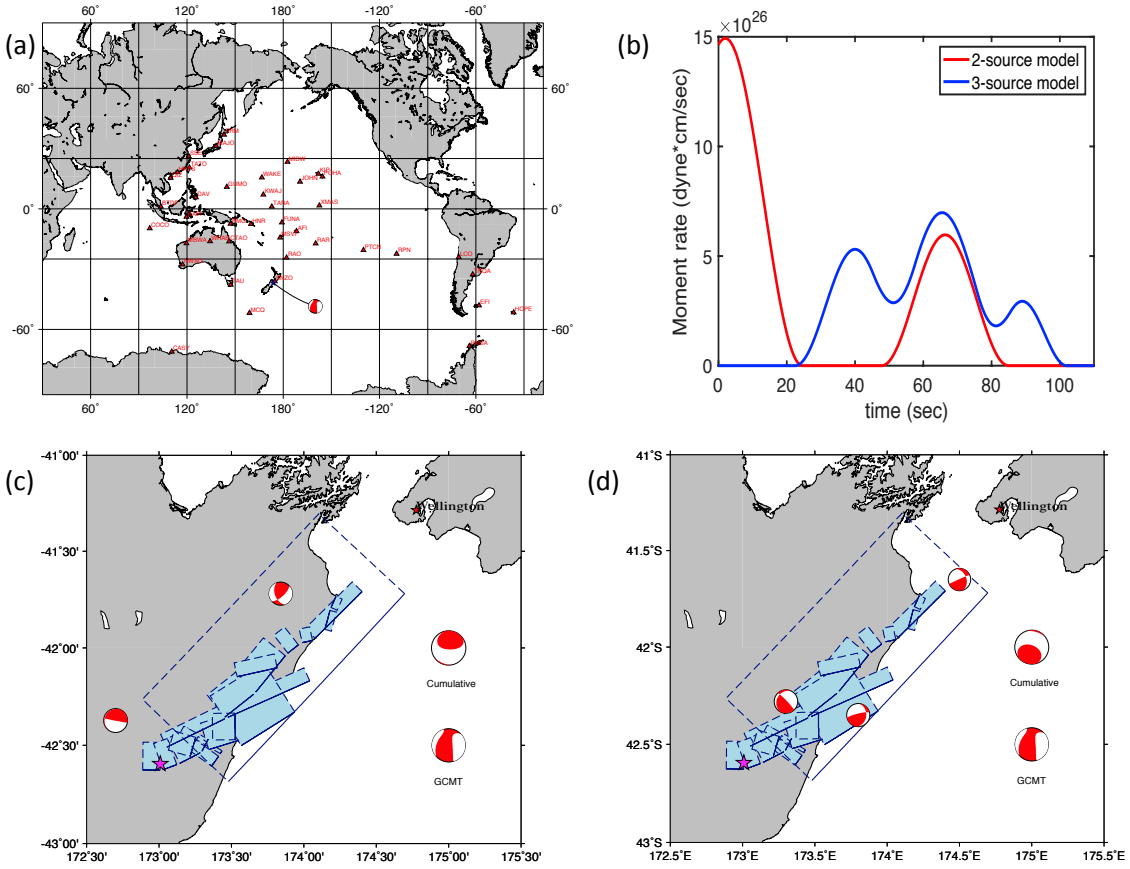

Figure 3: (a) Location and GCMT focal mechanism of the 2016 M_w 7.8 Kaikoura earthquake with positions and names of the global seismic stations used (red triangles). (b) Comparison of the cumulative moment rate functions of the 2-source model (red) versus the 3-source model (blue). (c) & (d) Locations and focal mechanisms of resulting inverted MDC solution for the 2-source model and 3-source model, respectively. Outline of the fault segments used in Clark et al. (2017) are in blue, with the hypocenter in pink. The cumulative focal mechanism for each model is compared to the GCMT solution.

(a)

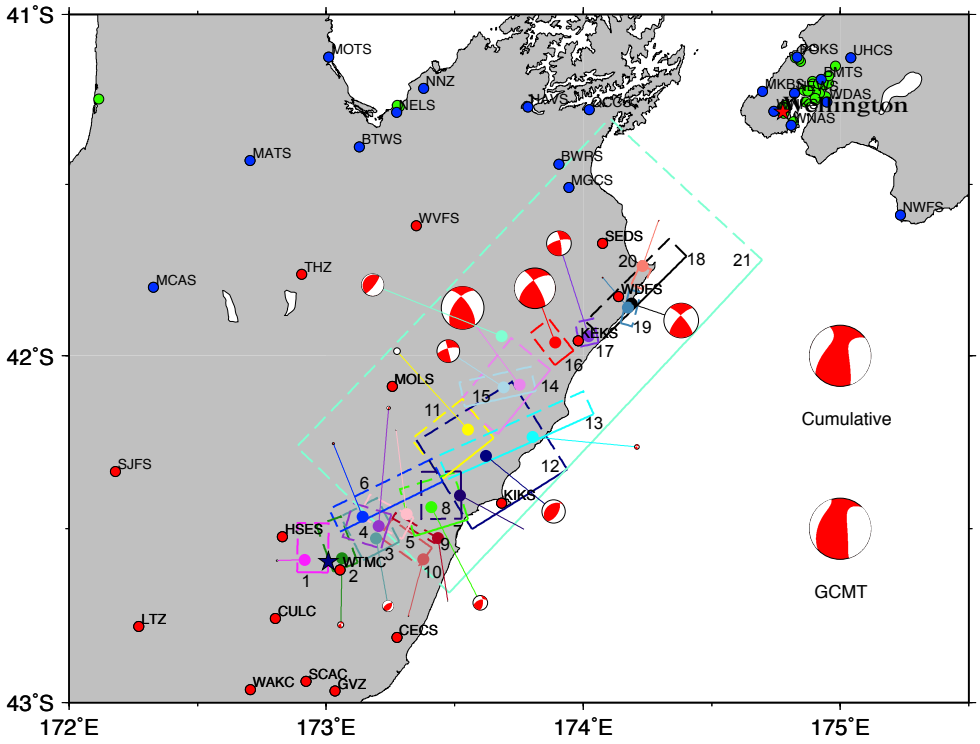
41°S
42°S
43°S
172°E
173°E
174°E
175°E
MOTS
NNZ
NELS
BTWS
MATS
BWRS
MGCS
WVFS
SEDS
THZ
MCAS
WDFS
KEKS
MOLS
SJFS
KIKS
HSES
WTMC
LTZ
CULC
CECS
WAKC
SCAC
GVZ
UHCS
BMTS
NWFS
Cumulative
GCMT

(b)

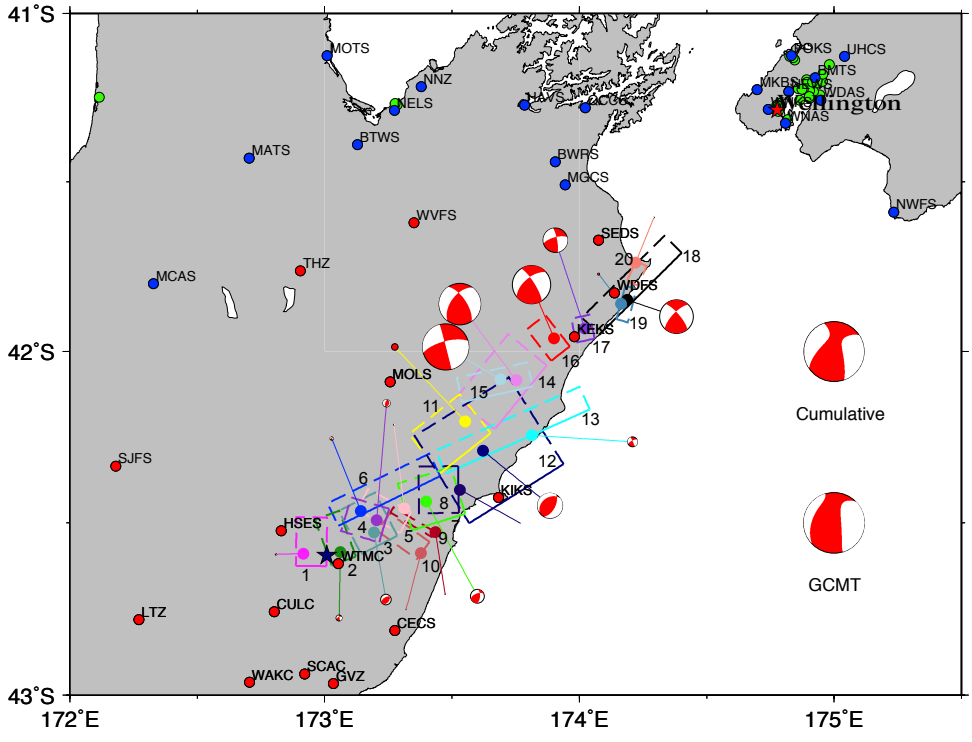
41°S
42°S
43°S
172°E
173°E
174°E
175°E
MOTS
NNZ
NELS
BTWS
MATS
BWRS
MGCS
WVFS
SEDS
THZ
MCAS
WDFS
KEKS
MOLS
SJFS
KIKS
HSES
WTMC
LTZ
CULC
CECS
WAKC
SCAC
GVZ
UHCS
BMTS
NWFS
Cumulative
GCMT

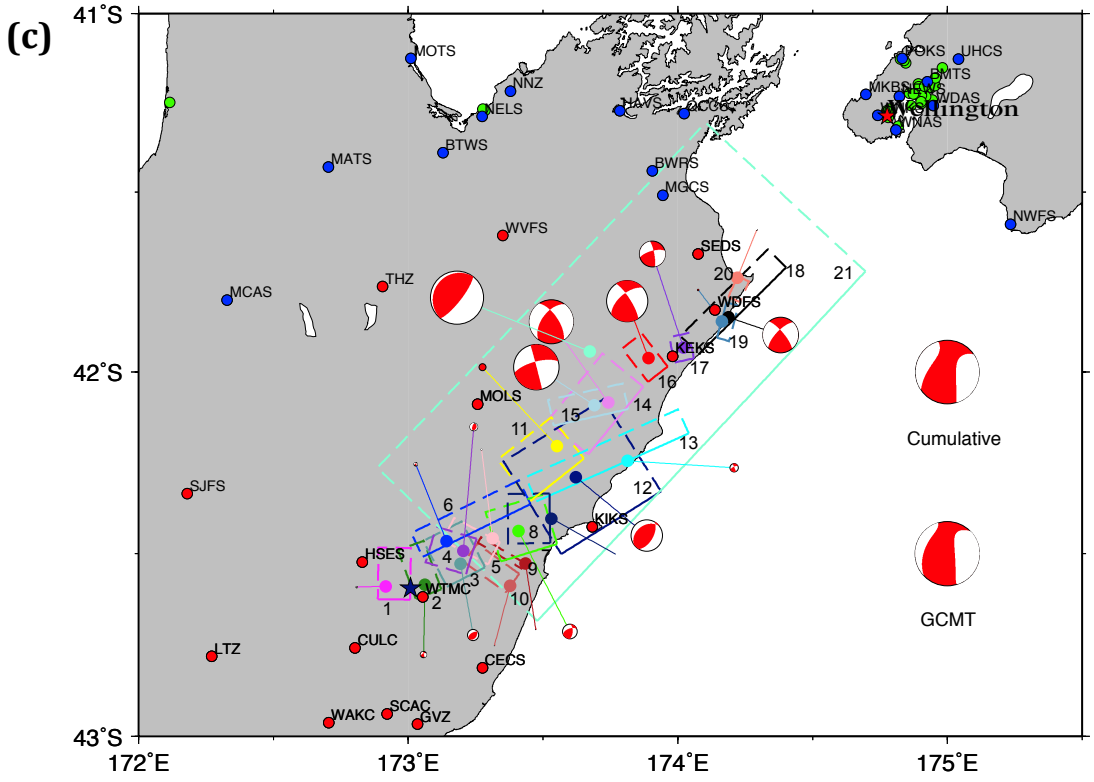

Figure 4: Multiple double-couple inversion results for (a) Case 3, (b) Case 2 and (c) Case 4. Surface projections of each fault segment are plotted with centroid locations and respective focal mechanisms. Solid lines are the surface break of each fault segment, and dashed lines are the down-dip edges of each fault segment. Each fault segment is numbered accordingly. Strong motion stations are plotted and the ones used in the inversions are in red. The inverted cumulative focal mechanism is also plotted in comparison with the Global CMT solution.

(a)

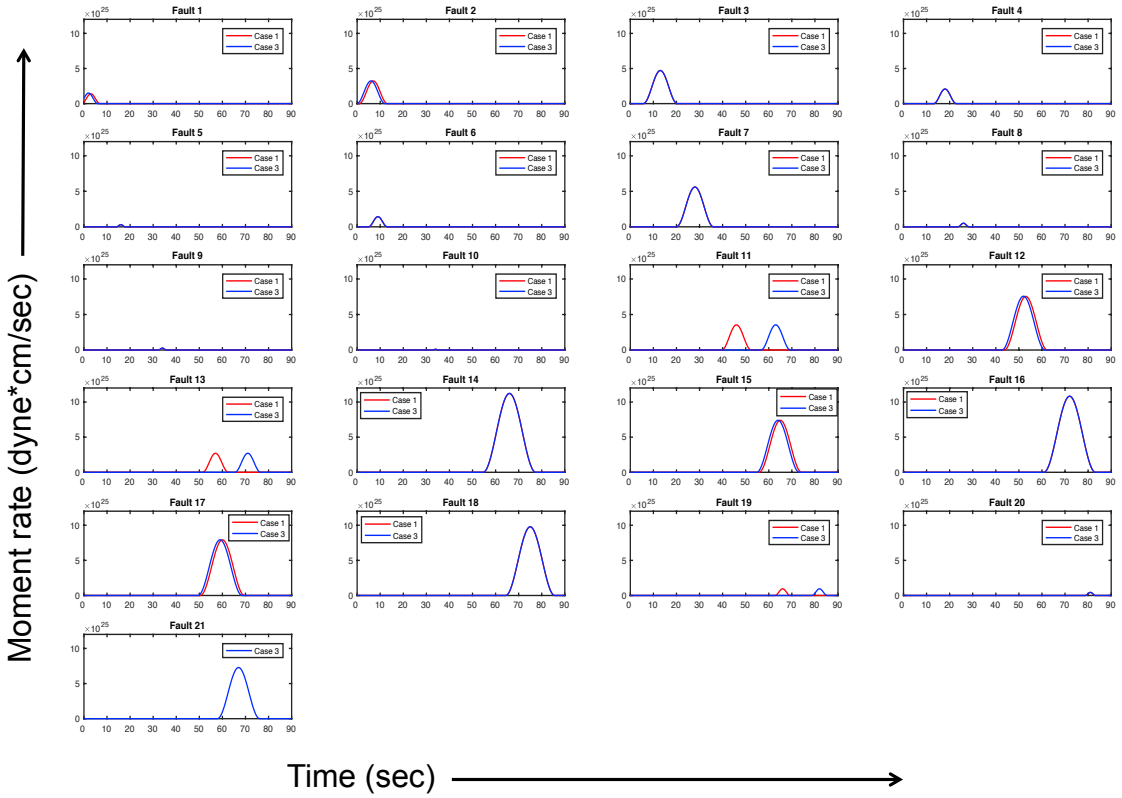
Fault 1
Fault 2
Fault 3
Fault 4
Fault 5
Fault 6
Fault 7
Fault 8
Fault 9
Fault 10
Fault 11
Fault 12
Fault 13
Fault 14
Fault 15
Fault 16
Fault 17
Fault 18
Fault 19
Fault 20
Fault 21
Case 1
Case 3
Moment rate (dyne*cm/sec)
Time (sec)

(b)

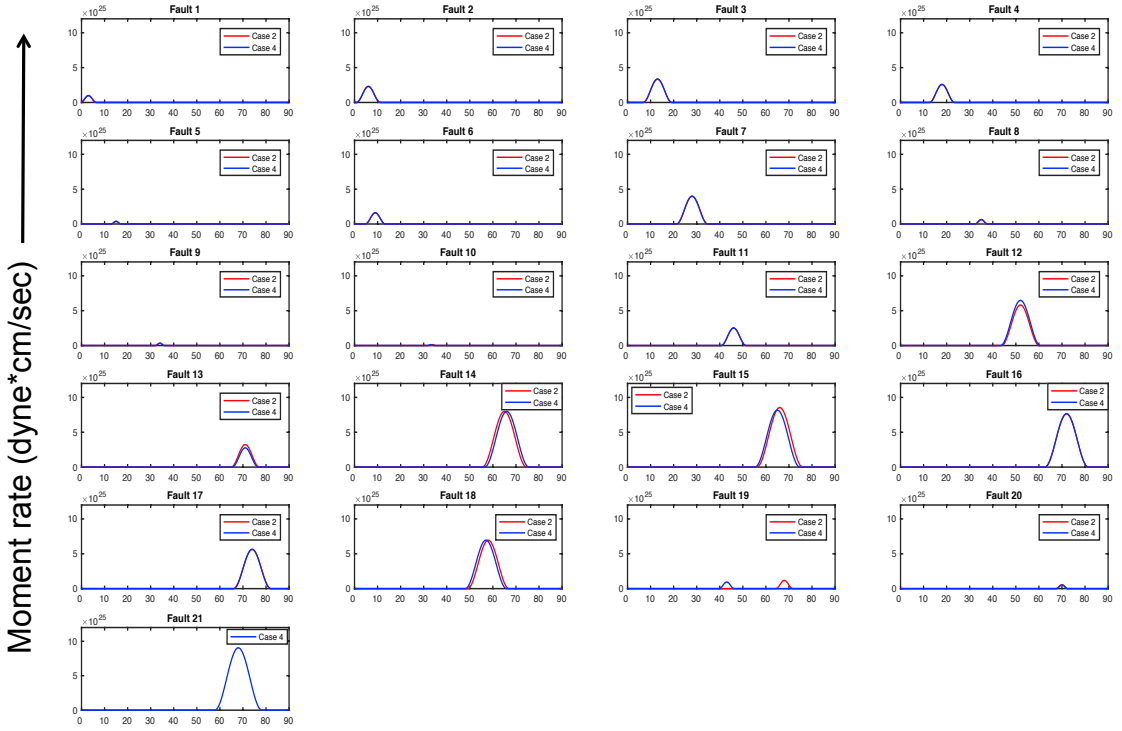
Fault 1
Fault 2
Fault 3
Fault 4
Fault 5
Fault 6
Fault 7
Fault 8
Fault 9
Fault 10
Fault 11
Fault 12
Fault 13
Fault 14
Fault 15
Fault 16
Fault 17
Fault 18
Fault 19
Fault 20
Fault 21
Case 2
Case 4
Moment rate (dyne*cm/sec)
Time (sec)

Figure 5: Individual moment rate functions (dyne*cm/sec) for each fault segment for (a) Case 1 (red) compared to Case 3 (blue), (b) Case 2 (red) versus Case 4 (blue) (on following page). Order of plots corresponds to sequence of faults numbered in Figure 4a.

(a)

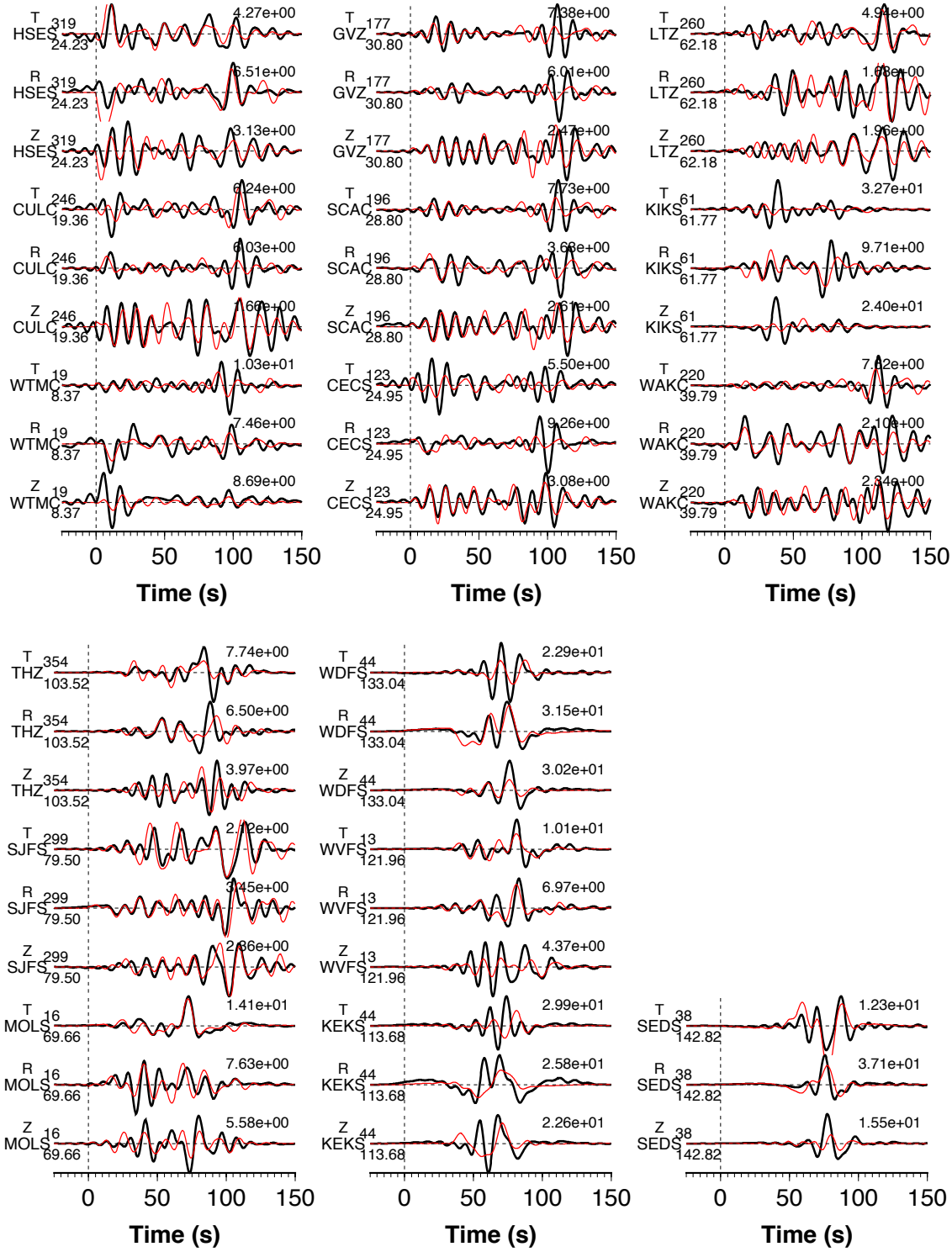
T HSES 319 24.23 4.27e+00
R HSES 319 24.23 6.51e+00
Z HSES 319 24.23 3.13e+00
T CULC 246 19.36 6.24e+00
R CULC 246 19.36 6.03e+00
Z CULC 246 19.36 1.66e+00
T WTMC 19 8.37 1.03e+01
R WTMC 19 8.37 7.46e+00
Z WTMC 19 8.37 8.69e+00
T GVZ 177 30.80 7.38e+00
R GVZ 177 30.80 6.01e+00
Z GVZ 177 30.80 2.47e+00
T SCAC 196 28.80 7.73e+00
R SCAC 196 28.80 3.66e+00
Z SCAC 196 28.80 2.61e+00
T CECS 123 24.95 5.50e+00
R CECS 123 24.95 9.26e+00
Z CECS 123 24.95 3.08e+00
T LTZ 260 62.18 4.94e+00
R LTZ 260 62.18 1.68e+00
Z LTZ 260 62.18 1.96e+00
T KIKS 61 61.77 3.27e+01
R KIKS 61 61.77 9.71e+00
Z KIKS 61 61.77 2.40e+01
T WAKC 220 39.79 7.02e+00
R WAKC 220 39.79 2.10e+00
Z WAKC 220 39.79 2.34e+00
0 50 100 150
Time (s)
T THZ 354 103.52 7.74e+00
R THZ 354 103.52 6.50e+00
Z THZ 354 103.52 3.97e+00
T SJFS 299 79.50 2.12e+00
R SJFS 299 79.50 3.45e+00
Z SJFS 299 79.50 2.66e+00
T MOLS 16 69.66 1.41e+01
R MOLS 16 69.66 7.63e+00
Z MOLS 16 69.66 5.58e+00
T WDFS 44 133.04 2.29e+01
R WDFS 44 133.04 3.15e+01
Z WDFS 44 133.04 3.02e+01
T WVFS 13 121.96 1.01e+01
R WVFS 13 121.96 6.97e+00
Z WVFS 13 121.96 4.37e+00
T KEKS 44 113.68 2.99e+01
R KEKS 44 113.68 2.58e+01
Z KEKS 44 113.68 2.26e+01
T SEDS 38 142.82 1.23e+01
R SEDS 38 142.82 3.71e+01
Z SEDS 38 142.82 1.55e+01
0 50 100 150
Time (s)

(b)

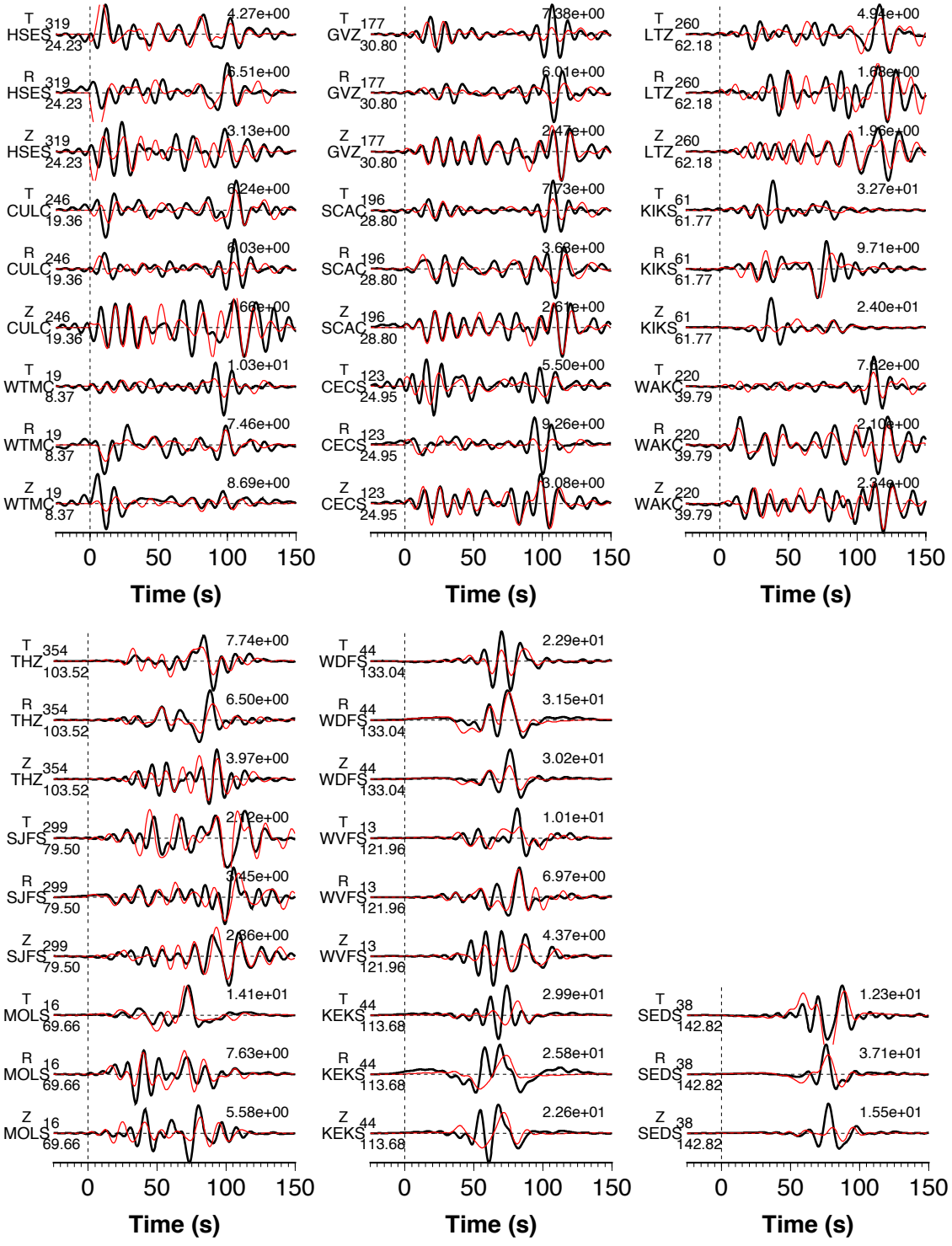
T HSES 319 24.23 4.27e+00
R HSES 319 24.23 6.51e+00
Z HSES 319 24.23 3.13e+00
T CULC 246 19.36 6.24e+00
R CULC 246 19.36 9.03e+00
Z CULC 246 19.36 6.66e+00
T WTMC 19 8.37 1.03e+01
R WTMC 19 8.37 7.46e+00
Z WTMC 19 8.37 8.69e+00
T GVZ 177 30.80 7.38e+00
R GVZ 177 30.80 6.01e+00
Z GVZ 177 30.80 2.47e+00
T SCAC 196 28.80 7.73e+00
R SCAC 196 28.80 3.68e+00
Z SCAC 196 28.80 2.61e+00
T CECS 123 24.95 5.50e+00
R CECS 123 24.95 9.26e+00
Z CECS 123 24.95 3.08e+00
T LTZ 260 62.18 4.94e+00
R LTZ 260 62.18 1.68e+00
Z LTZ 260 62.18 1.96e+00
T KIKS 61 61.77 3.27e+01
R KIKS 61 61.77 9.71e+00
Z KIKS 61 61.77 2.40e+01
T WAKC 220 39.79 7.82e+00
R WAKC 220 39.79 2.10e+00
Z WAKC 220 39.79 2.34e+00
T THZ 354 103.52 7.74e+00
R THZ 354 103.52 6.50e+00
Z THZ 354 103.52 3.97e+00
T SJFS 299 79.50 2.12e+00
R SJFS 299 79.50 3.45e+00
Z SJFS 299 79.50 2.86e+00
T MOLS 16 69.66 1.41e+01
R MOLS 16 69.66 7.63e+00
Z MOLS 16 69.66 5.58e+00
T WDFS 44 133.04 2.29e+01
R WDFS 44 133.04 3.15e+01
Z WDFS 44 133.04 3.02e+01
T WVFS 13 121.96 1.01e+01
R WVFS 13 121.96 6.97e+00
Z WVFS 13 121.96 4.37e+00
T KEKS 44 113.68 2.99e+01
R KEKS 44 113.68 2.58e+01
Z KEKS 44 113.68 2.26e+01
T SEDS 38 142.82 1.23e+01
R SEDS 38 142.82 3.71e+01
Z SEDS 38 142.82 1.55e+01
0 50 100 150
Time (s)

Figure 6: Comparison of 16 three-component (vertical, radial and transverse) strong motion waveforms (black lines) and synthetic seismograms (red lines) calculated for (a) Case 1 and (b) Case 3 (following page). The station names are indicated to the left of the traces, along with the epicenter distances and azimuthal angle in degrees. At the end of the trace, the peak amplitude (cm/sec) of the observation is given.

(a)

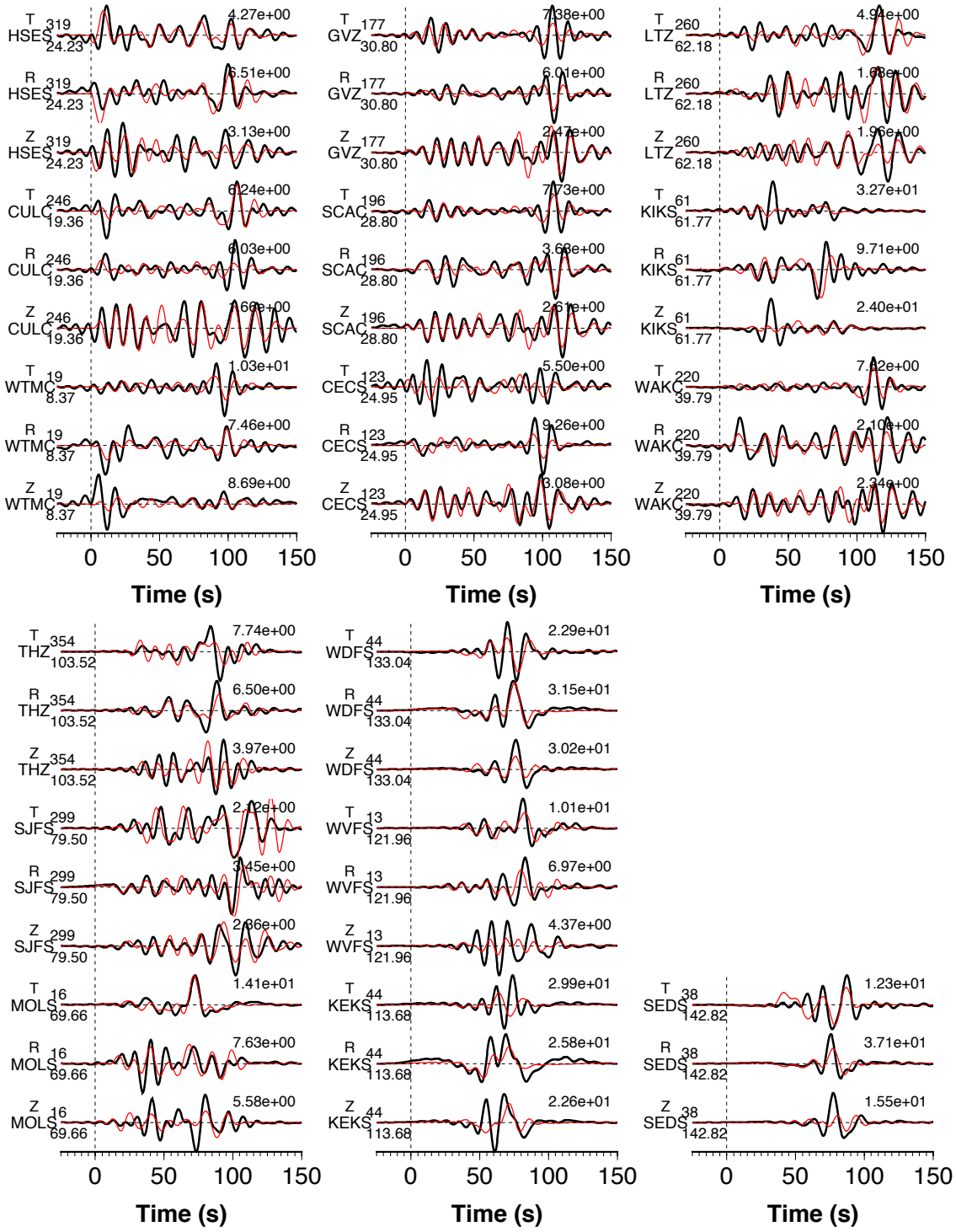
T HSES 319 24.23 4.27e+00
R HSES 319 24.23 6.51e+00
Z HSES 319 24.23 3.13e+00
T CULC 246 19.36 6.24e+00
R CULC 246 19.36 6.03e+00
Z CULC 246 19.36 1.66e+00
T WTMC 19 8.37 1.03e+01
R WTMC 19 8.37 7.46e+00
Z WTMC 19 8.37 8.69e+00
T GVZ 177 30.80 7.38e+00
R GVZ 177 30.80 6.01e+00
Z GVZ 177 30.80 2.47e+00
T SCAC 196 28.80 7.73e+00
R SCAC 196 28.80 3.66e+00
Z SCAC 196 28.80 2.81e+00
T CECS 123 24.95 5.50e+00
R CECS 123 24.95 9.26e+00
Z CECS 123 24.95 3.08e+00
T LTZ 260 62.18 4.94e+00
R LTZ 260 62.18 1.68e+00
Z LTZ 260 62.18 1.96e+00
T KIKS 61 61.77 3.27e+01
R KIKS 61 61.77 9.71e+00
Z KIKS 61 61.77 2.40e+01
T WAKC 220 39.79 7.82e+00
R WAKC 220 39.79 2.10e+00
Z WAKC 220 39.79 2.34e+00
0 50 100 150
Time (s)
T THZ 354 103.52 7.74e+00
R THZ 354 103.52 6.50e+00
Z THZ 354 103.52 3.97e+00
T SJFS 299 79.50 2.02e+00
R SJFS 299 79.50 3.45e+00
Z SJFS 299 79.50 2.86e+00
T MOLS 16 69.66 1.41e+01
R MOLS 16 69.66 7.63e+00
Z MOLS 16 69.66 5.58e+00
T WDFS 44 133.04 2.29e+01
R WDFS 44 133.04 3.15e+01
Z WDFS 44 133.04 3.02e+01
T WVFS 13 121.96 1.01e+01
R WVFS 13 121.96 6.97e+00
Z WVFS 13 121.96 4.37e+00
T KEKS 44 113.68 2.99e+01
R KEKS 44 113.68 2.58e+01
Z KEKS 44 113.68 2.26e+01
T SEDS 38 142.82 1.23e+01
R SEDS 38 142.82 3.71e+01
Z SEDS 38 142.82 1.55e+01
0 50 100 150
Time (s)

(b)

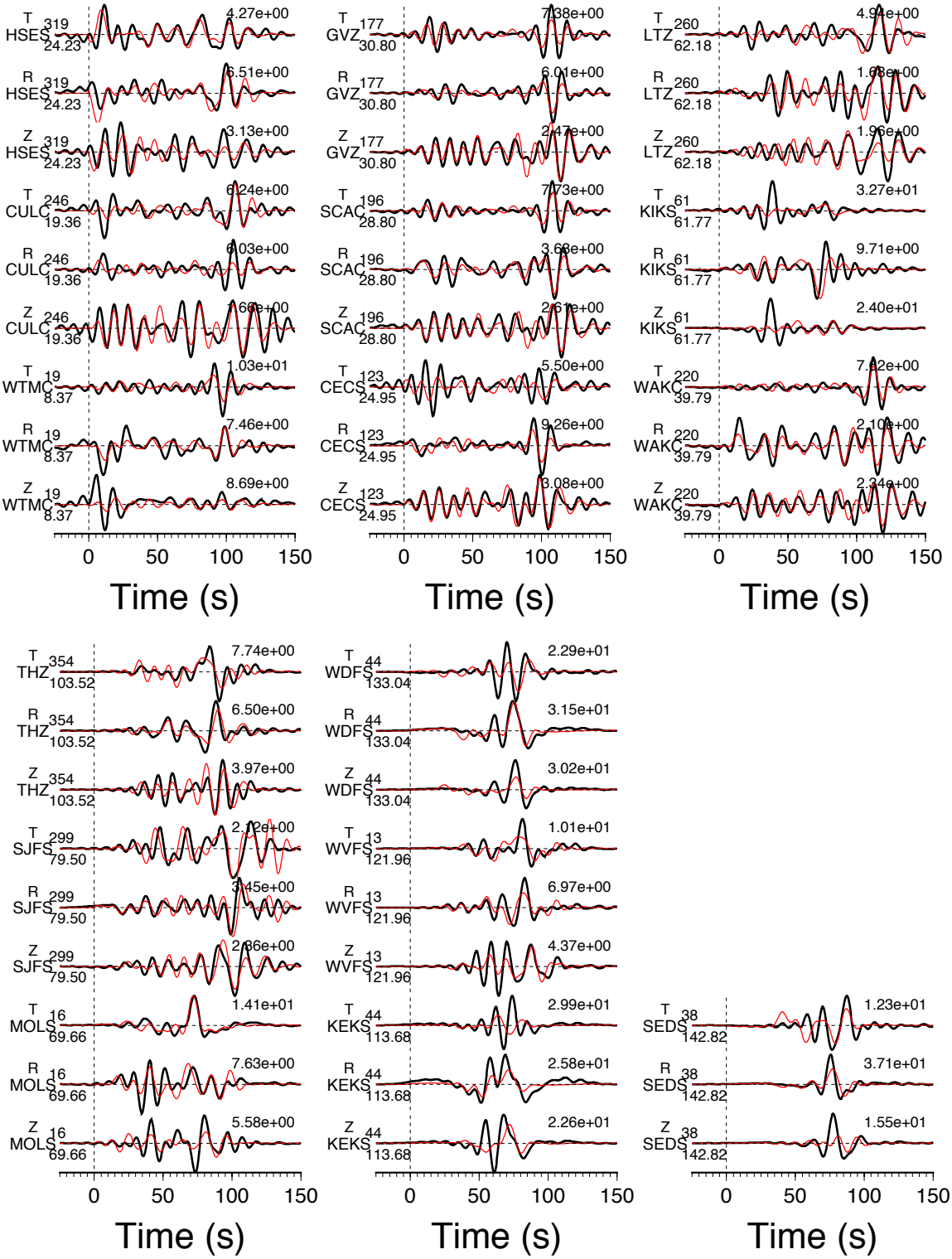
T HSES 319 24.23 4.27e+00
R HSES 319 24.23 6.51e+00
Z HSES 319 24.23 3.13e+00
T CULC 246 19.36 6.24e+00
R CULC 246 19.36 6.03e+00
Z CULC 246 19.36 1.66e+00
T WTMC 19 8.37 1.03e+01
R WTMC 19 8.37 7.46e+00
Z WTMC 19 8.37 8.69e+00
T GVZ 177 30.80 7.38e+00
R GVZ 177 30.80 6.01e+00
Z GVZ 177 30.80 2.47e+00
T SCAC 196 28.80 7.73e+00
R SCAC 196 28.80 3.68e+00
Z SCAC 196 28.80 2.61e+00
T CECS 123 24.95 5.50e+00
R CECS 123 24.95 9.26e+00
Z CECS 123 24.95 3.08e+00
T LTZ 260 62.18 4.94e+00
R LTZ 260 62.18 1.68e+00
Z LTZ 260 62.18 1.96e+00
T KIKS 61 61.77 3.27e+01
R KIKS 61 61.77 9.71e+00
Z KIKS 61 61.77 2.40e+01
T WAKC 220 39.79 7.82e+00
R WAKC 220 39.79 2.10e+00
Z WAKC 220 39.79 2.34e+00
T THZ 354 103.52 7.74e+00
R THZ 354 103.52 6.50e+00
Z THZ 354 103.52 3.97e+00
T SJFS 299 79.50 2.12e+00
R SJFS 299 79.50 3.45e+00
Z SJFS 299 79.50 2.66e+00
T MOLS 16 69.66 1.41e+01
R MOLS 16 69.66 7.63e+00
Z MOLS 16 69.66 5.58e+00
T WDFS 44 133.04 2.29e+01
R WDFS 44 133.04 3.15e+01
Z WDFS 44 133.04 3.02e+01
T WVFS 13 121.96 1.01e+01
R WVFS 13 121.96 6.97e+00
Z WVFS 13 121.96 4.37e+00
T KEKS 44 113.68 2.99e+01
R KEKS 44 113.68 2.58e+01
Z KEKS 44 113.68 2.26e+01
T SEDS 38 142.82 1.23e+01
R SEDS 38 142.82 3.71e+01
Z SEDS 38 142.82 1.55e+01
0 50 100 150
Time (s)

Figure 7: Comparison of 16 three-component (vertical, radial and transverse) strong motion waveforms (black lines) and synthetic seismograms (red lines) calculated for (a) Case 2 and (b) Case 4 (following page). The station names are indicated to the left of the traces, along with the epicenter distances and azimuthal angle in degrees. At the end of the trace, the peak amplitude (cm/sec) of the observation is given.

(a)

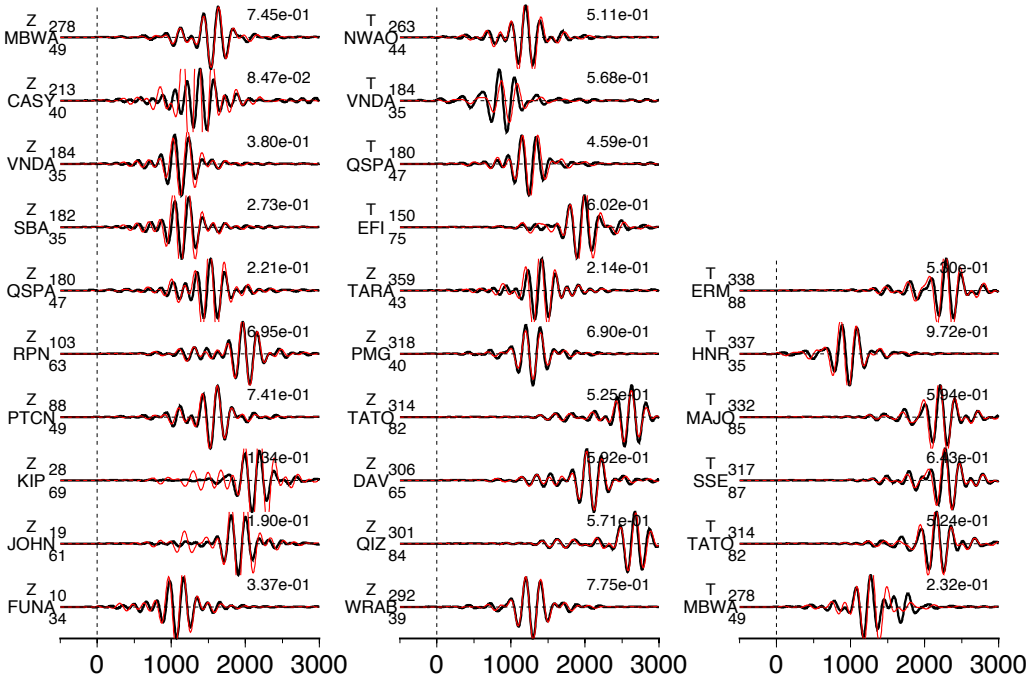
Z MBWA 278 49 7.45e-01
Z CASY 213 40 8.47e-02
Z VNDA 184 35 3.80e-01
Z SBA 182 35 2.73e-01
Z QSPA 180 47 2.21e-01
Z RPN 103 63 6.95e-01
Z PTCN 88 49 7.41e-01
Z KIP 28 69 1.34e-01
Z JOHN 19 61 1.90e-01
Z FUNA 10 34 3.37e-01
T NWAO 263 44 5.11e-01
T VNDA 184 35 5.68e-01
T QSPA 180 47 4.59e-01
T EFI 150 75 6.02e-01
Z TARA 359 43 2.14e-01
Z PMG 318 40 6.90e-01
Z TATO 314 82 5.25e-01
Z DAV 306 65 5.02e-01
Z QIZ 301 84 5.71e-01
Z WRAB 292 39 7.75e-01
T ERM 338 88 5.30e-01
T HNR 337 35 9.72e-01
T MAJO 332 85 5.94e-01
T SSE 317 87 6.43e-01
T TATO 314 82 5.24e-01
T MBWA 278 49 2.32e-01
0 1000 2000 3000
0 1000 2000 3000
0 1000 2000 3000

(b)

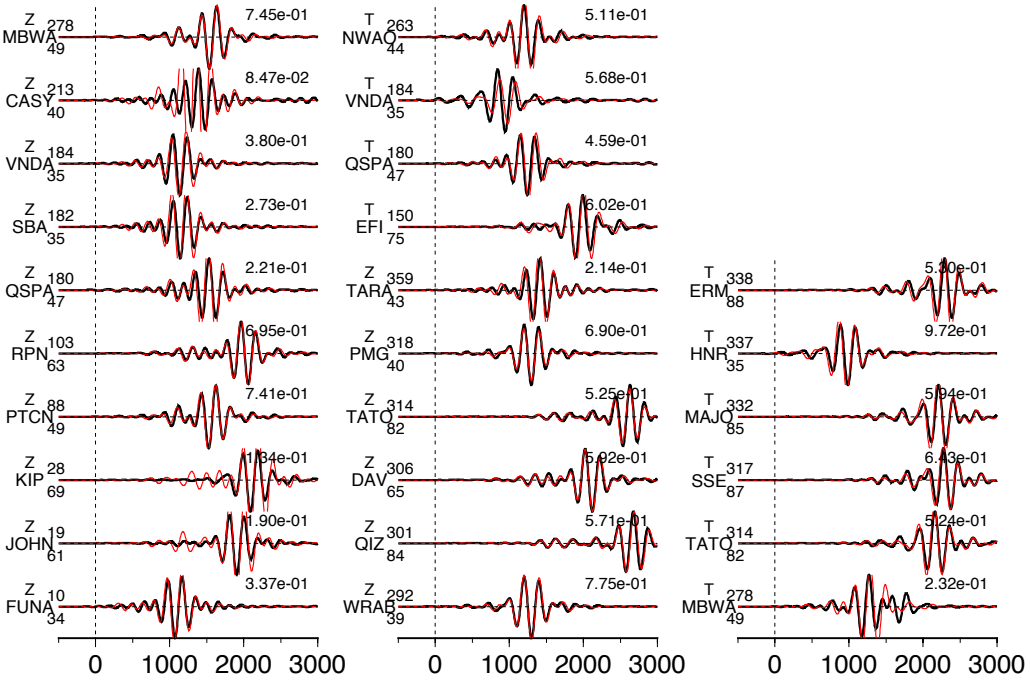
Z MBWA 278 49 7.45e-01
Z CASY 213 40 8.47e-02
Z VNDA 184 35 3.80e-01
Z SBA 182 35 2.73e-01
Z QSPA 180 47 2.21e-01
Z RPN 103 63 6.95e-01
Z PTCN 88 49 7.41e-01
Z KIP 28 69 1.34e-01
Z JOHN 19 61 1.90e-01
Z FUNA 10 34 3.37e-01
T NWAO 263 44 5.11e-01
T VNDA 184 35 5.68e-01
T QSPA 180 47 4.59e-01
T EFI 150 75 6.02e-01
Z TARA 359 43 2.14e-01
Z PMG 318 40 6.90e-01
Z TATO 314 82 5.25e-01
Z DAV 306 65 5.02e-01
Z QIZ 301 84 5.71e-01
Z WRAB 292 39 7.75e-01
T ERM 338 88 5.30e-01
T HNR 337 35 9.72e-01
T MAJO 332 85 5.94e-01
T SSE 317 87 6.43e-01
T TATO 314 82 5.24e-01
T MBWA 278 49 2.32e-01
0 1000 2000 3000
0 1000 2000 3000
0 1000 2000 3000

(c)

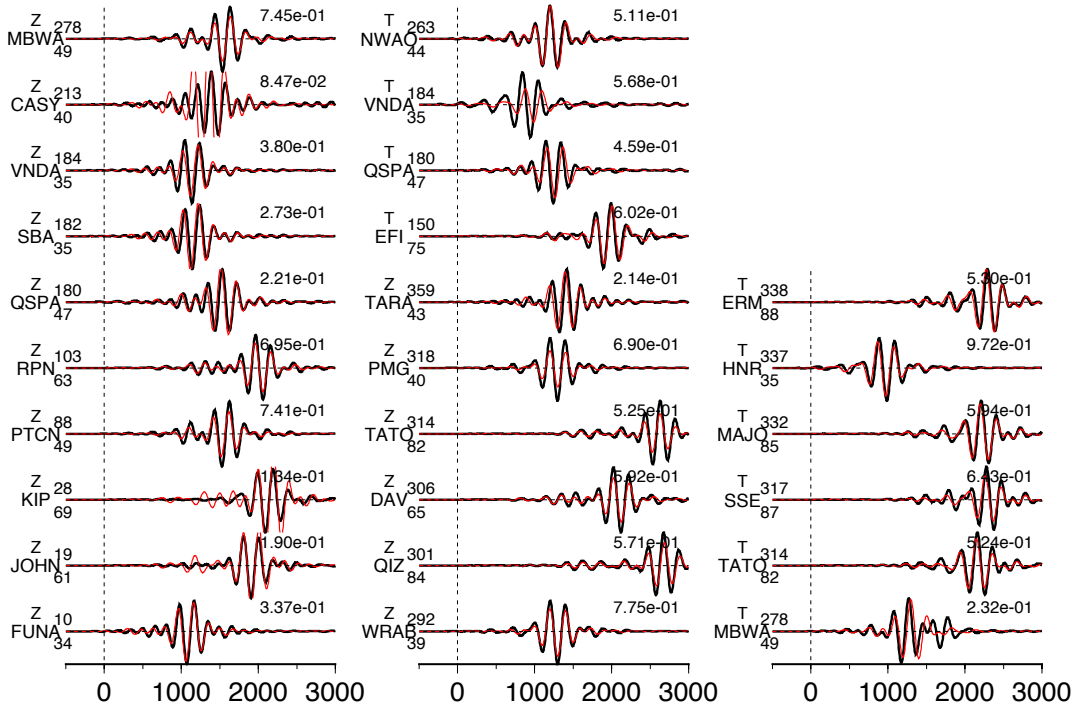
Z MBWA 278 49 7.45e-01
Z CASY 213 40 8.47e-02
Z VNDA 184 35 3.80e-01
Z SBA 182 35 2.73e-01
Z QSPA 180 47 2.21e-01
Z RPN 103 63 6.95e-01
Z PTCN 88 49 7.41e-01
Z KIP 28 69 1.84e-01
Z JOHN 19 61 1.90e-01
Z FUNA 10 34 3.37e-01
T NWAO 263 44 5.11e-01
T VNDA 184 35 5.68e-01
T QSPA 180 47 4.59e-01
T EFI 150 75 6.02e-01
Z TARA 359 43 2.14e-01
Z PMG 318 40 6.90e-01
Z TATO 314 82 5.25e-01
Z DAV 306 65 5.92e-01
Z QIZ 301 84 5.71e-01
Z WRAB 292 39 7.75e-01
T ERM 338 88 5.30e-01
T HNR 337 35 9.72e-01
T MAJO 332 85 5.94e-01
T SSE 317 87 6.43e-01
T TATO 314 82 5.24e-01
T MBWA 278 49 2.32e-01
0 1000 2000 3000
0 1000 2000 3000
0 1000 2000 3000

(d)

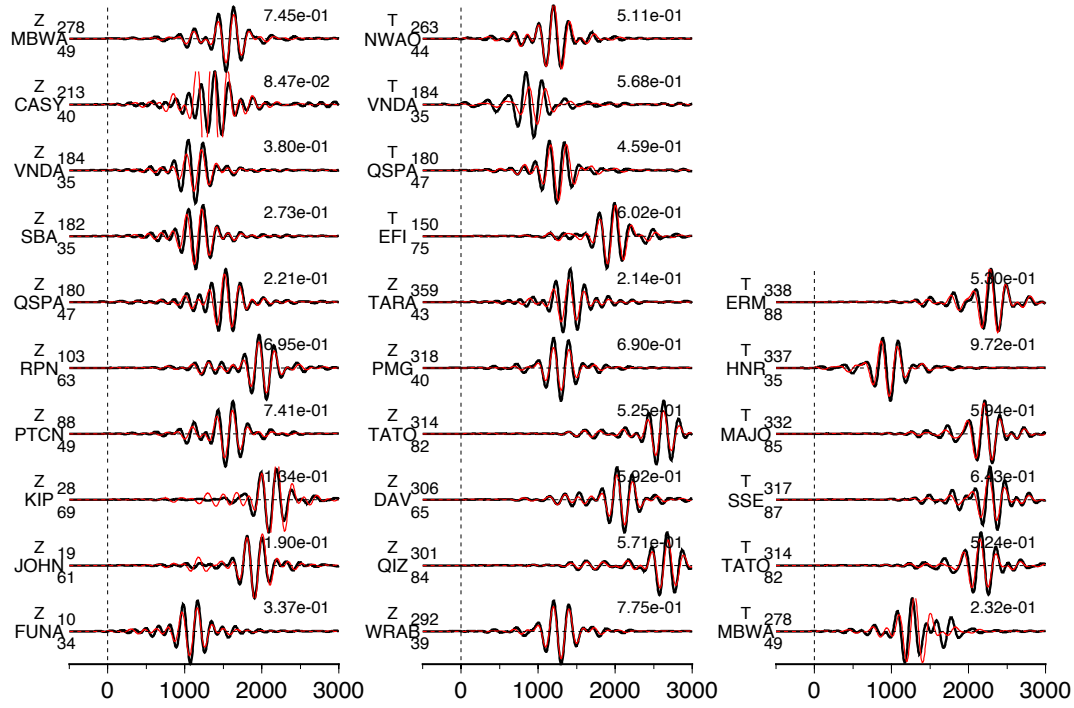
Z MBWA 278 49 7.45e-01
Z CASY 213 40 8.47e-02
Z VNDA 184 35 3.80e-01
Z SBA 182 35 2.73e-01
Z QSPA 180 47 2.21e-01
Z RPN 103 63 6.95e-01
Z PTCN 88 49 7.41e-01
Z KIP 28 69 1.84e-01
Z JOHN 19 61 1.90e-01
Z FUNA 10 34 3.37e-01
T NWAO 263 44 5.11e-01
T VNDA 184 35 5.68e-01
T QSPA 180 47 4.59e-01
T EFI 150 75 6.02e-01
Z TARA 359 43 2.14e-01
Z PMG 318 40 6.90e-01
Z TATO 314 82 5.25e-01
Z DAV 306 65 5.92e-01
Z QIZ 301 84 5.71e-01
Z WRAB 292 39 7.75e-01
T ERM 338 88 5.30e-01
T HNR 337 35 9.72e-01
T MAJO 332 85 5.94e-01
T SSE 317 87 6.43e-01
T TATO 314 82 5.24e-01
T MBWA 278 49 2.32e-01
0 1000 2000 3000
0 1000 2000 3000
0 1000 2000 3000

Figure 8: Comparison of the vertical and transverse components of 26 teleseismic waveforms (black lines) and synthetic seismograms (red lines) that were forward predicted from the MDC inversion results for (a) Case 1, (b) Case 3, (c) Case 2, and (d) Case 4. The station names are indicated to the left of the traces, along with the epicenter distances and azimuthal angle in degrees. At the end of the trace, the peak amplitude (mm) of the observation is given.

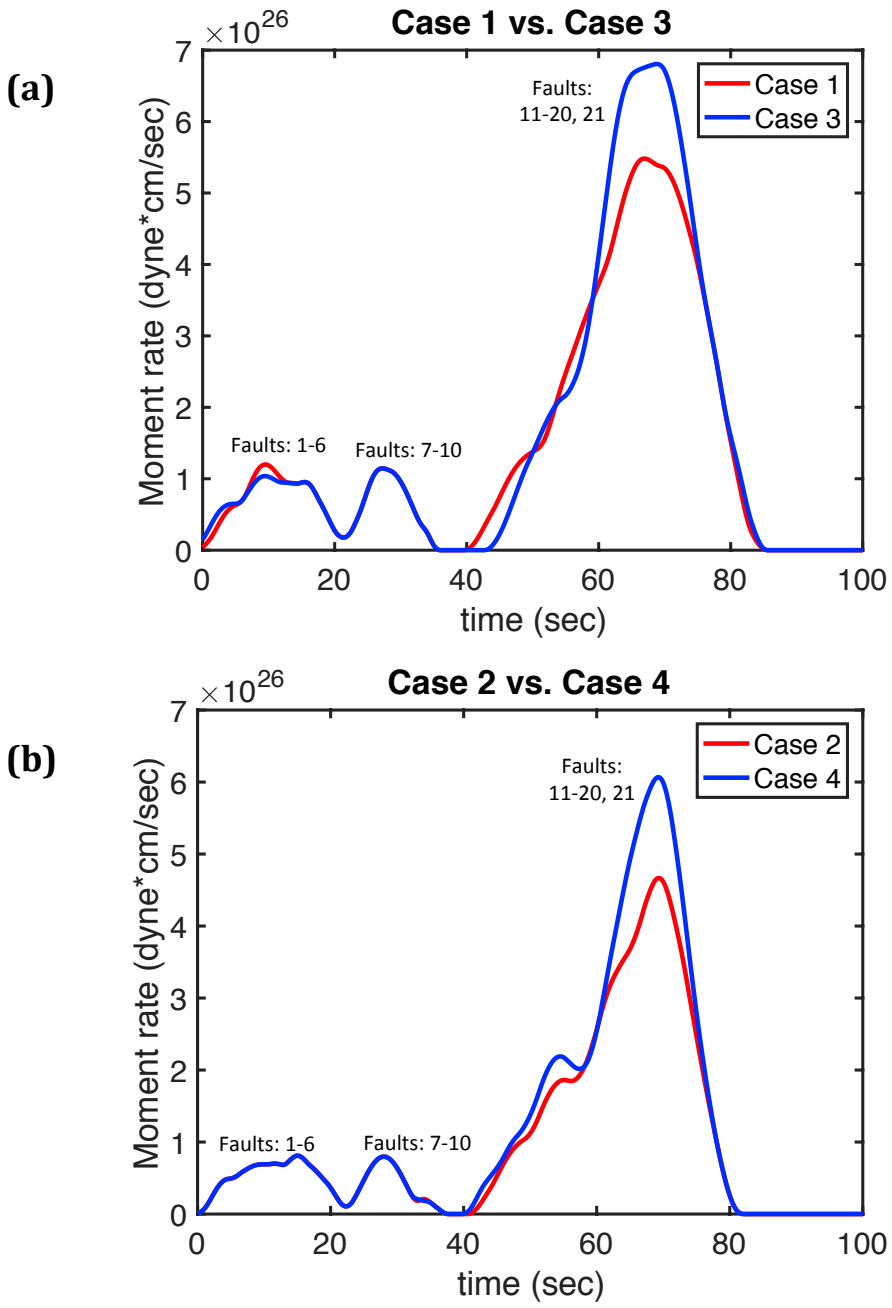

Figure 9: Comparison of the cumulative moment rate function (dyne*cm/sec) for (a) Case 1 versus Case 3, and (b) Case 2 versus Case 4. Fault segment numbers, corresponding to Figure 4, are plotted with respect to their centroid time to illustrate the faults that contribute to certain energy pulses.

	# Fault Segments	Invert for centroid time	Invert for Moment	Misfit	ε
Case 1	20	Yes	No	0.28304	-0.081
Case 2	20	Yes	Yes	0.25889	-0.100
Case 3	21	Yes	No	0.27838	-0.142
Case 4	21	Yes	Yes	0.25134	-0.211

Table 1: Description of case studies for the Multiple Double-Couple inversions using the fault geometry in Clark et al. (2017) and strong motion data.

(a)

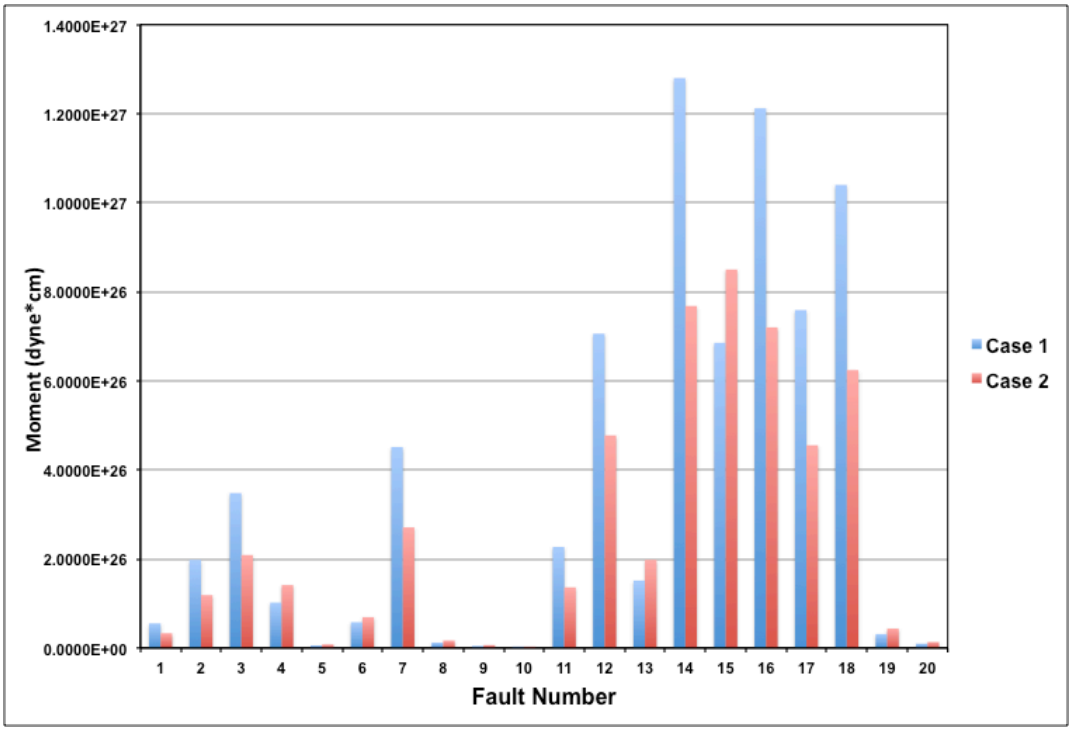

(b)

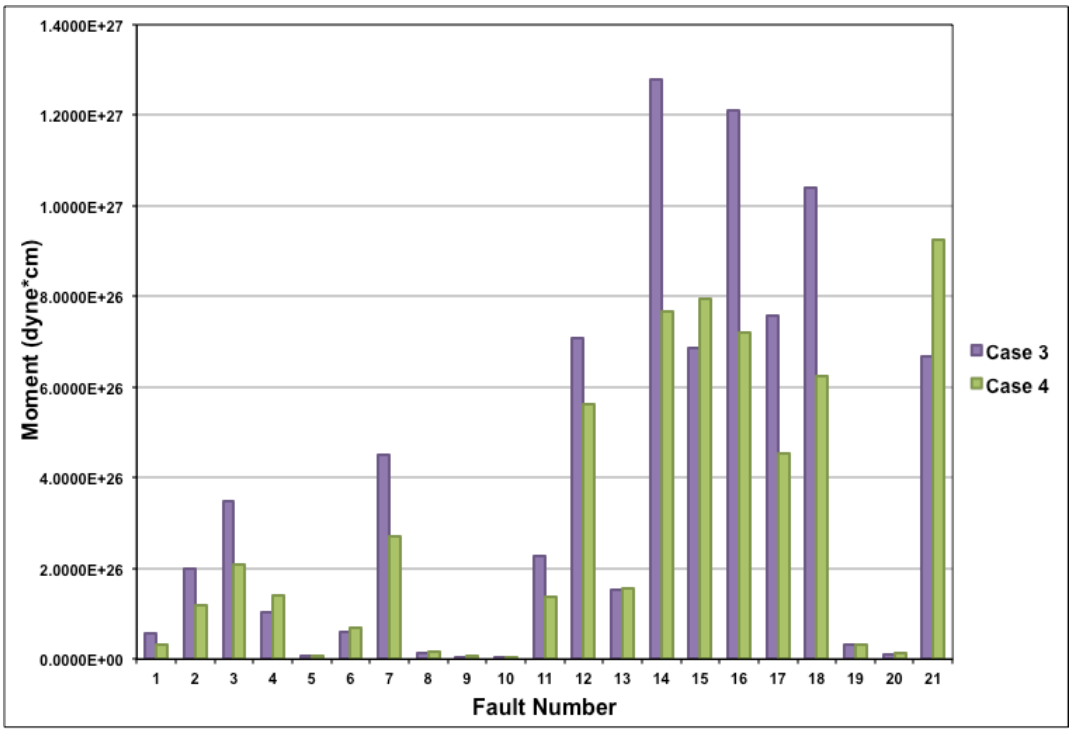

Figure 10: Seismic moment (dyne*cm) for each fault segment in (a) Case 1 versus Case 2; and (b) Case 3 versus Case 4.

(a)

Fault Segment	Rupture time (sec)	Half duration (sec)	Latitude	Longitude	Depth (km)	Moment (dyne*cm)	Strike	Dip	Rake
1	3	4.002058	-42.59	172.916	6	5.5371E+25	267	55	179
2	7	6.1199	-42.586	173.062	5	1.9800E+26	248	56	166
3	13	7.385542	-42.528	173.194	8	3.4800E+26	240	56	107
4	18	4.906106	-42.493	173.204	5	1.0201E+26	195	60	91
5	16	1.891328	-42.458	173.313	5	5.8443E+24	206	56	91
6	9	4.062451	-42.456	173.152	4	5.792E+25	241	70	159
7	28	8.054585	-42.438	173.409	11	4.5140E+26	250	55	143
8	26	2.417769	-42.394	173.521	2	1.2209E+25	177	60	115
9	34	1.770972	-42.589	173.378	1	4.7981E+24	214	56	91
10	34	1.112693	-42.517	173.435	2	1.1900E+24	209	56	91
11	46	6.405178	-42.204	173.552	13	2.270E+26	230	55	180
12	53	9.34925	-42.29	173.622	12	7.0593E+26	235	36	112
13	57	5.596568	-42.235	173.813	3	1.514E+26	243	70	175
14	66	11.40055	-42.094	173.752	8	1.280E+27	216	55	149
15	65	9.257539	-42.091	173.69	12	6.8536E+26	255	70	179
16	72	11.19498	-41.961	173.891	9	1.2120E+27	231	61	165
17	60	9.577512	-41.942	174.021	9	7.5891E+26	255	70	169
18	75	10.63817	-41.848	174.188	6	1.0400E+27	224	71	164
19	66	3.314311	-41.859	174.164	4	3.1449E+25	14	81	123
20	81	2.249928	-41.738	174.231	2	9.8387E+24	23	81	169

(b)

Fault Segment	Rupture time (sec)	Half duration (sec)	Latitude	Longitude	Depth (km)	Moment (dyne*cm)	Strike	Dip	Rake
1	2	4.002058	-42.59	172.916	6	5.5371E+25	267	55	179
2	6	6.1199	-42.586	173.062	5	1.9800E+26	248	56	166
3	13	7.385542	-42.528	173.194	8	3.4800E+26	240	56	107
4	18	4.906106	-42.493	173.204	5	1.0201E+26	195	60	91
5	16	1.89164	-42.458	173.313	5	5.8472E+24	206	55	91
6	9	4.073912	-42.466	173.142	4	5.841E+25	242	70	159
7	28	8.054585	-42.438	173.409	11	4.5140E+26	250	55	143
8	26	2.418567	-42.404	173.521	2	1.2221E+25	177	60	115
9	34	1.771265	-42.589	173.378	1	4.8005E+24	214	56	91
10	34	1.111773	-42.527	173.435	1	1.1871E+24	209	56	91
11	63	6.405178	-42.214	173.552	12	2.270E+26	230	56	180
12	52	9.363176	-42.29	173.622	13	7.0909E+26	236	36	112
13	71	5.597492	-42.235	173.803	3	1.515E+26	243	70	175
14	66	11.40055	-42.084	173.752	8	1.280E+27	216	55	149
15	64	9.257539	-42.091	173.69	12	6.8536E+26	255	70	179
16	72	11.19498	-41.961	173.891	9	1.2120E+27	231	61	165
17	59	9.577512	-41.942	174.021	10	7.5891E+26	255	70	168
18	75	10.63817	-41.848	174.188	6	1.0400E+27	223	71	164
19	82	3.31267	-41.859	174.174	4	3.1403E+25	14	81	123
20	81	2.249928	-41.738	174.231	2	9.8387E+24	23	81	169
21	67	9.181544	-41.942	173.683	29	6.6862E+26	221	13	93

(c)

Fault Segment	Rupture time (sec)	Half duration (sec)	Latitude	Longitude	Depth (km)	Moment (dyne*cm)	Strike	Dip	Rake
1	3	3.375467	-42.59	172.916	6	3.3223E+25	267	55	179
2	6	5.161724	-42.586	173.062	5	1.1880E+26	248	56	166
3	13	6.229207	-42.528	173.194	8	2.0880E+26	240	56	107
4	18	5.470232	-42.493	173.204	5	1.4140E+26	195	60	91
5	15	2.109149	-42.458	173.313	5	8.1050E+24	206	56	91
6	9	4.314842	-42.466	173.142	4	6.939E+25	241	70	159
7	28	6.793499	-42.438	173.399	11	2.7084E+26	250	56	143
8	35	2.696666	-42.404	173.531	2	1.6940E+25	177	60	115
9	34	1.975912	-42.589	173.378	1	6.6640E+24	214	56	91
10	34	1.24125	-42.527	173.435	2	1.6520E+24	209	56	91
11	46	5.402337	-42.204	173.552	13	1.362E+26	230	55	180
12	52	8.206394	-42.29	173.622	13	4.7741E+26	235	36	112
13	71	6.1199	-42.245	173.813	3	1.980E+26	244	70	175
14	65	9.6156	-42.084	173.752	8	7.680E+26	217	55	149
15	66	9.945717	-42.081	173.69	12	8.4985E+26	255	70	179
16	72	9.41095	-41.961	173.901	9	7.2000E+26	230	60	165
17	74	8.077987	-41.932	174.021	10	4.5535E+26	255	70	168
18	58	8.972583	-41.848	174.188	6	6.2400E+26	224	71	164
19	68	3.695406	-41.859	174.164	4	4.3593E+25	14	81	123
20	70	2.508636	-41.738	174.221	2	1.3638E+25	23	81	169

(d)

Fault Segment	Rupture time (sec)	Half duration (sec)	Latitude	Longitude	Depth (km)	Moment (dyne*cm)	Strike	Dip	Rake
1	3	3.375467	-42.59	172.916	6	3.3223E+25	267	55	179
2	6	5.161724	-42.586	173.062	5	1.1880E+26	248	56	166
3	13	6.229207	-42.528	173.194	8	2.0880E+26	240	56	107
4	18	5.470232	-42.493	173.204	5	1.4140E+26	195	60	91
5	15	2.109149	-42.458	173.313	5	8.1050E+24	206	56	91
6	9	4.314842	-42.466	173.142	4	6.939E+25	241	70	159
7	28	6.793499	-42.438	173.409	11	2.7084E+26	250	56	143
8	35	2.696666	-42.404	173.531	2	1.6940E+25	177	60	115
9	34	1.975912	-42.589	173.378	1	6.6640E+24	214	56	91
10	33	1.24125	-42.527	173.435	1	1.6520E+24	209	56	91
11	46	5.402337	-42.204	173.552	13	1.362E+26	230	55	180
12	52	8.663221	-42.29	173.622	13	5.6166E+26	236	36	112
13	71	5.652373	-42.245	173.813	3	1.560E+26	244	70	175
14	66	9.6156	-42.084	173.742	8	7.680E+26	217	55	149
15	65	9.727058	-42.091	173.69	12	7.9502E+26	255	70	179
16	72	9.41095	-41.961	173.891	9	7.2000E+26	230	60	165
17	74	8.077987	-41.932	174.021	10	4.5535E+26	255	70	168
18	57	8.972583	-41.848	174.188	6	6.2400E+26	224	70	164
19	43	3.303337	-41.859	174.164	4	3.1138E+25	14	81	123
20	70	2.508636	-41.738	174.221	2	1.3638E+25	23	81	169
21	68	10.23728	-41.942	173.673	29	9.2680E+26	221	13	93

Table 2: Inverted parameter values for all fault segments for (a) Case 1, (b) Case 3, (c) Case 2, and (d) Case 4.

(a)

Fault #	Fault Name	Strike	Dip	Length (km)	Width (km)
1	Humps West	77	65	21.0	20
2	Humps East	255	70	21.0	20
3	Leader	195	50	21.0	24
4	Hundalee West	230	45	28.0	32
5	Whites	172	45	24.5	32
6	Point Kean	243	35	28.0	40
7	Papatea	172	50	21.0	32
8	Jordan - Kekerengu	223	50	59.5	32
9	Kekerengu	242	50	21.0	32
10	Needles	222	50	35.0	32

(b)

Fault #	Fault Name	Strike	Dip	Length (km)	Width (km)
1	Humps West	77	65	21.0	20
2	Humps East	255	70	38.5	20
3	Leader	195	50	21.0	24
4	Hundalee West	230	45	28.0	32
5	Whites	172	45	24.5	32
6	Point Kean	243	35	35.0	48
7	Papatea	172	50	21.0	32
8	Jordan - Kekerengu	223	50	59.5	32
9	Kekerengu	242	50	21.0	32
10	Needles	222	50	35.0	32

Table 3: Fault geometry details of each of the fault segments used in (a) FF1 and (b) FF2.

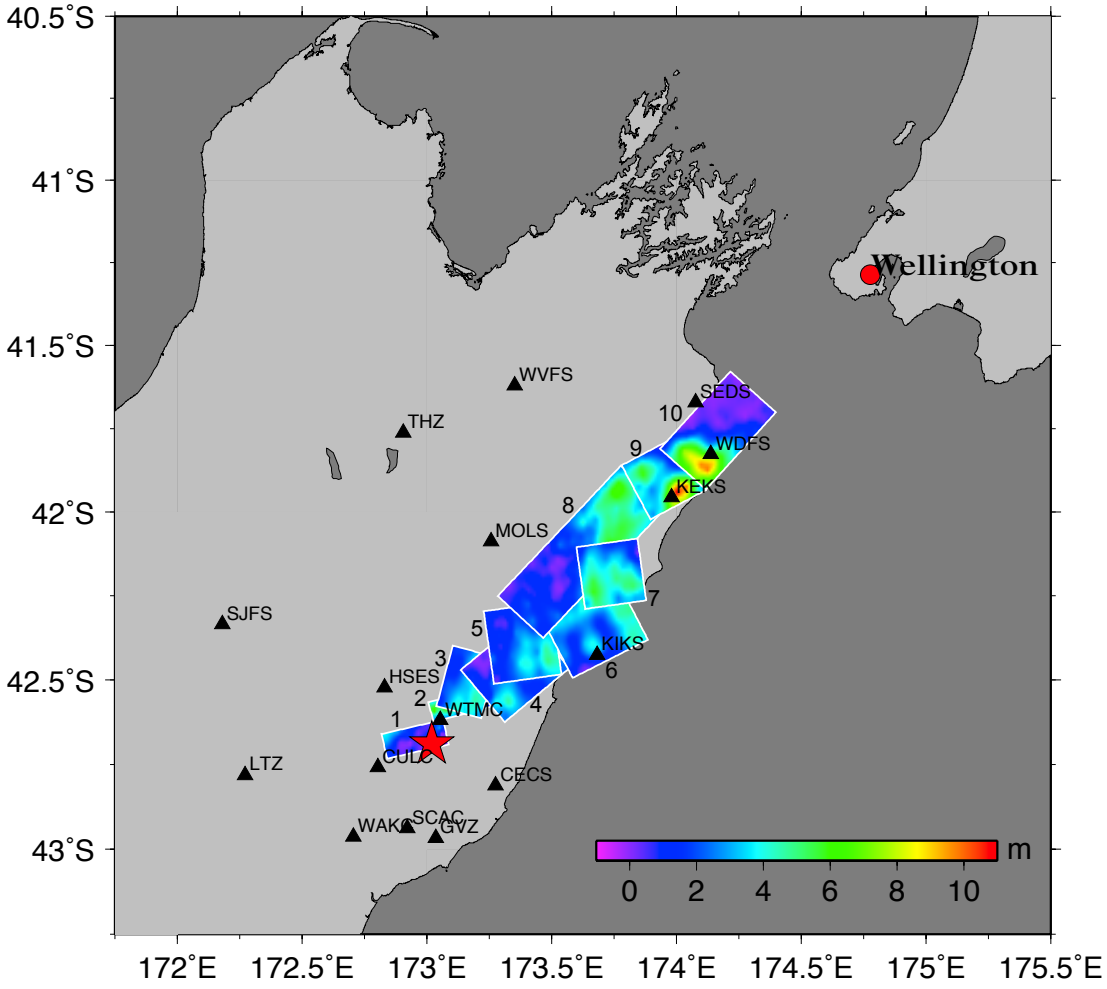

Figure 11: Finite fault slip distribution of the 10-fault segment model described in section 4.2 using strong motion data only. Strong motion stations are shown as black triangles.

(a)

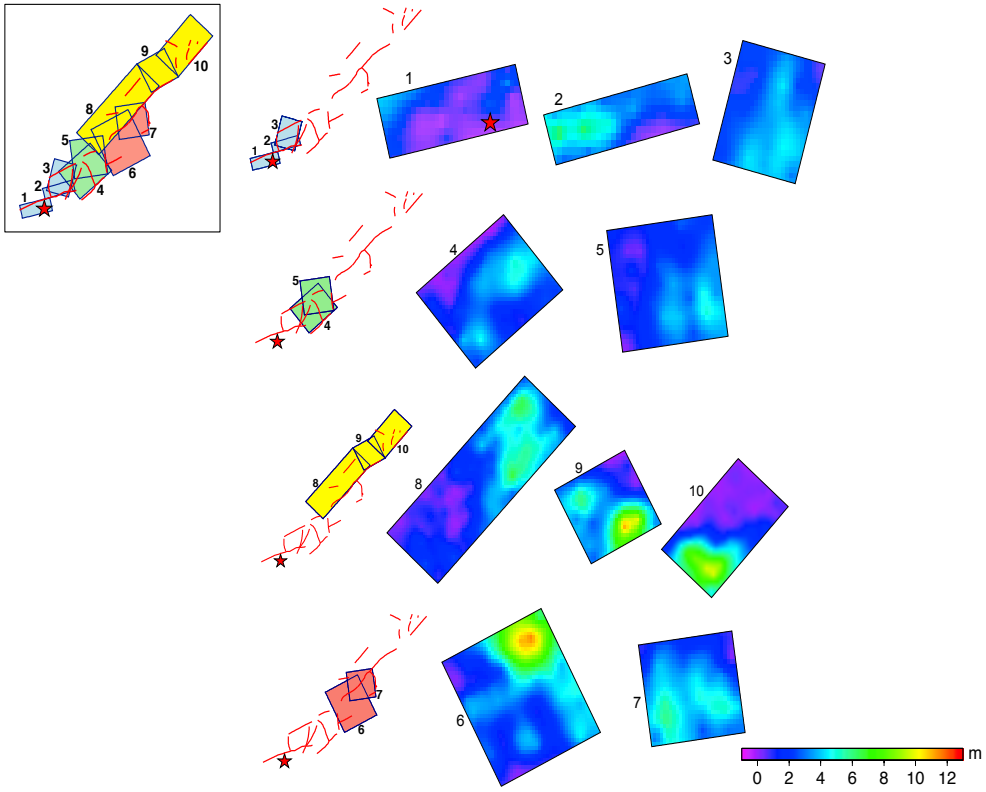
1
2
3
4
5
6
7
8
9
10
m
0 2 4 6 8 10 12

(b)

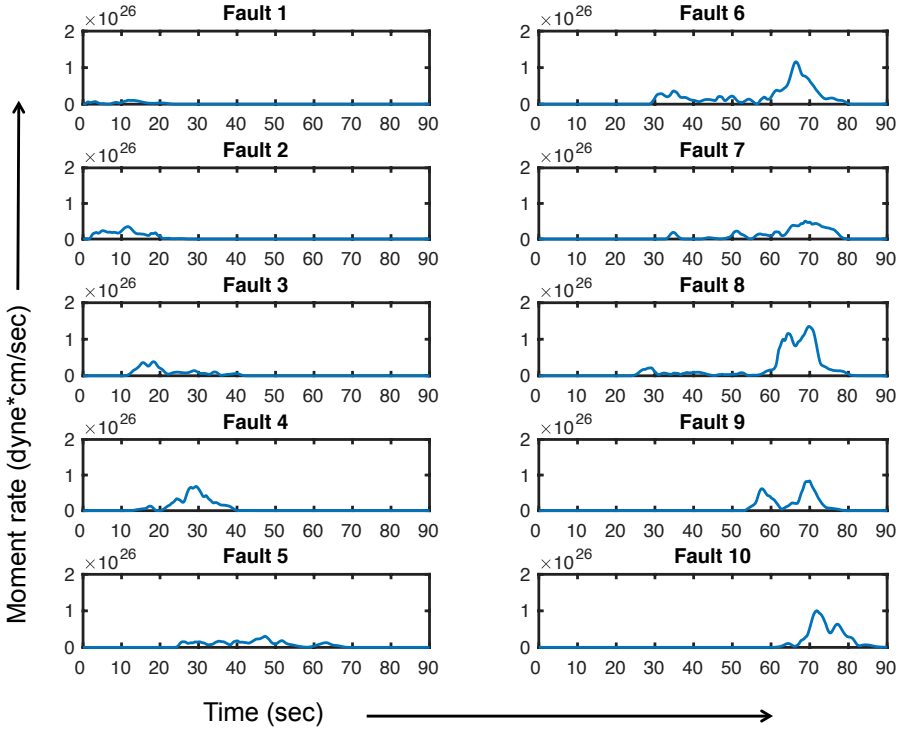
Fault 1
Fault 2
Fault 3
Fault 4
Fault 5
Fault 6
Fault 7
Fault 8
Fault 9
Fault 10
×10^26
0 10 20 30 40 50 60 70 80 90
Moment rate (dyne*cm/sec)
Time (sec)

Figure 12: (a) Detailed slip history of all ten fault segments used in the finite fault inversion of strong motion data only, FF1. Faults are numbered according to the sequence seen in Figure 11, and the thick red lines are the mapped surface fault traces. (b) Moment rate functions (dyne*cm/sec) for each individual fault segment in (a).

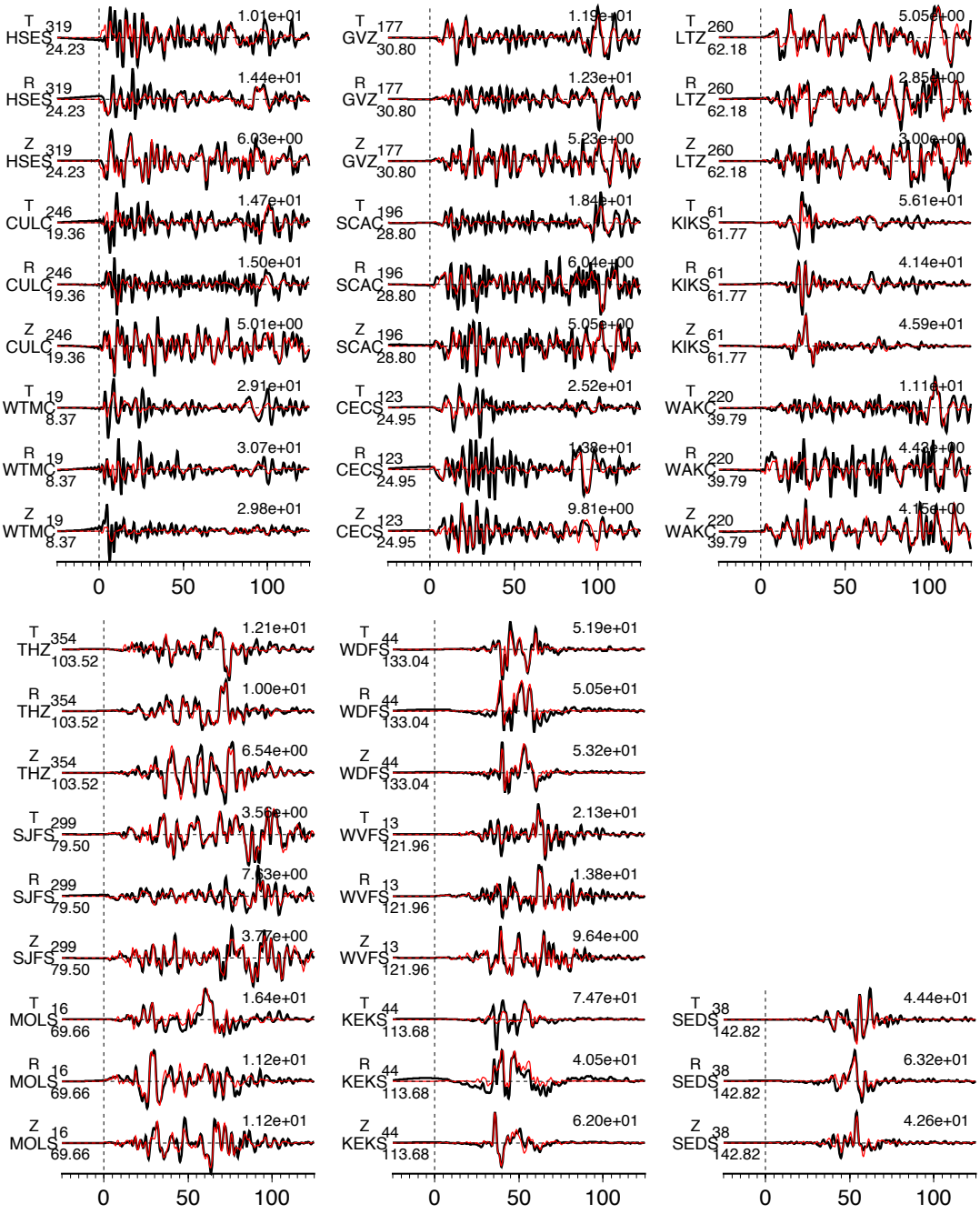

Figure 13: Comparison of 16 three-component velocity strong motion waveforms (black lines) and synthetic seismograms (red lines) for FF1. The station names are indicated to the left of the traces, along with the epicenter distances and azimuthal angle in degrees. At the end of the trace, the peak amplitude (cm/s) of the observation is given.

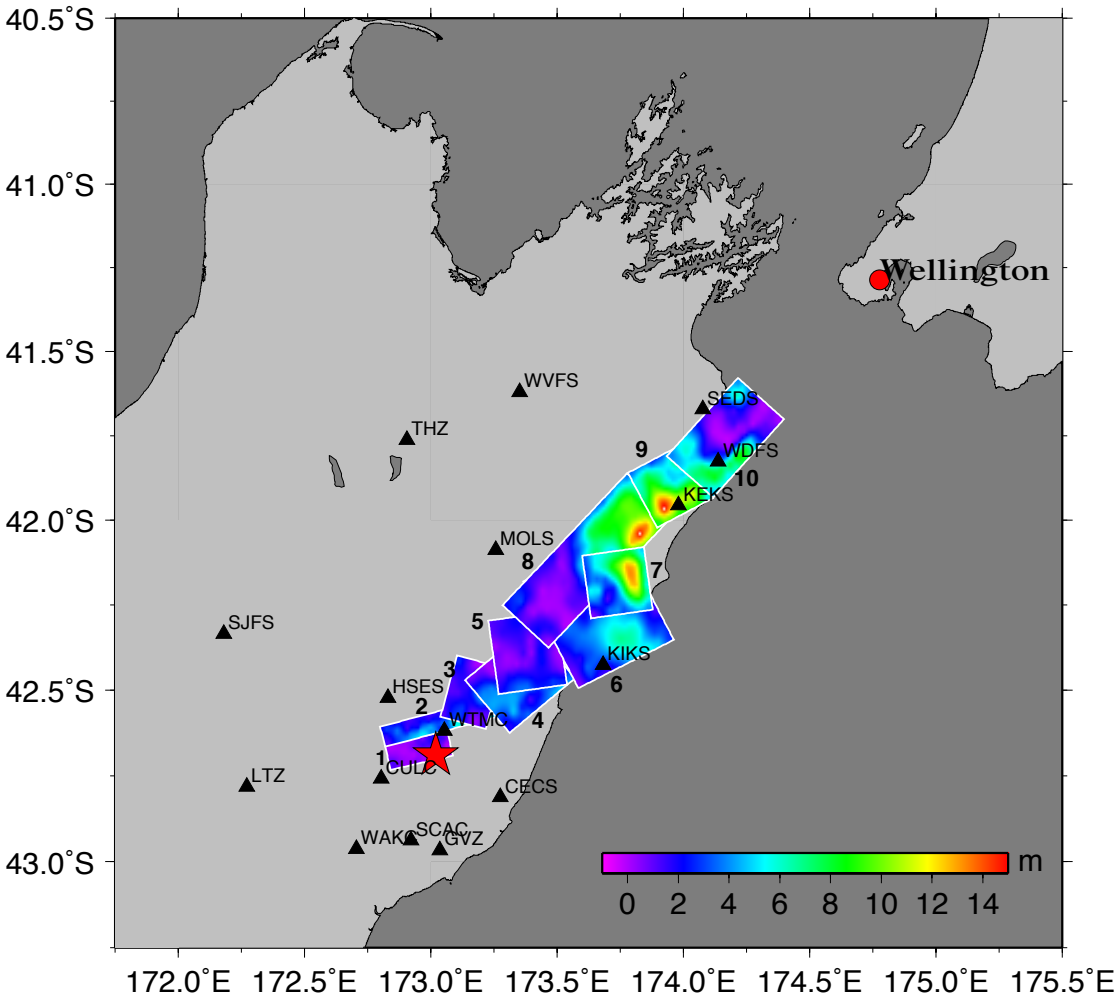

Figure 14: Finite fault slip distribution of the 10-fault segment model using strong motion and GPS data. Strong motion stations are shown as black triangles, and faults are numbered in sequence from southwest to northeast.

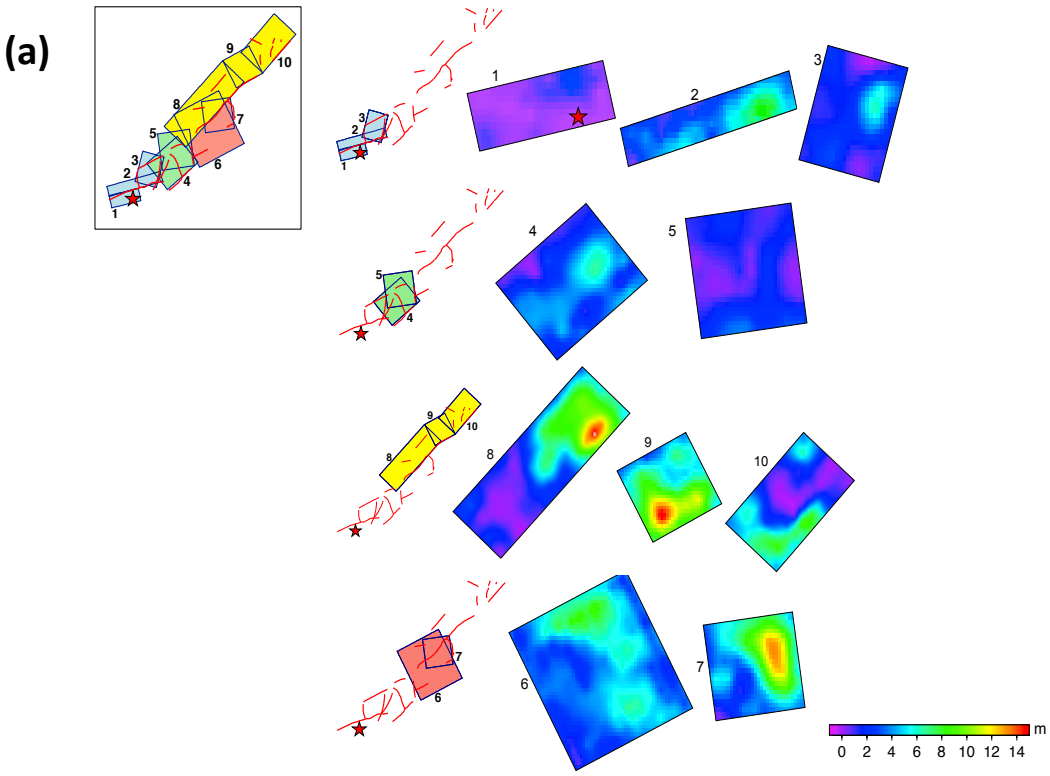
(a)
1
2
3
4
5
6
7
8
9
10
0 2 4 6 8 10 12 14
m
(b)
Fault 1
Fault 2
Fault 3
Fault 4
Fault 5
Fault 6
Fault 7
Fault 8
Fault 9
Fault 10
×10^19
0 10 20 30 40 50 60 70 80 90 100
Moment rate (Nm)
Time (sec)

Figure 15: (a) Detailed slip history of all ten fault segments used in the finite fault inversion of strong motion and GPS data, FF2. Faults are numbered according to the sequence seen in Figure 12, and the thick red lines are the mapped surface fault traces. (b) Moment rate functions (Nm/sec) for each individual fault segment in (a).

(a)

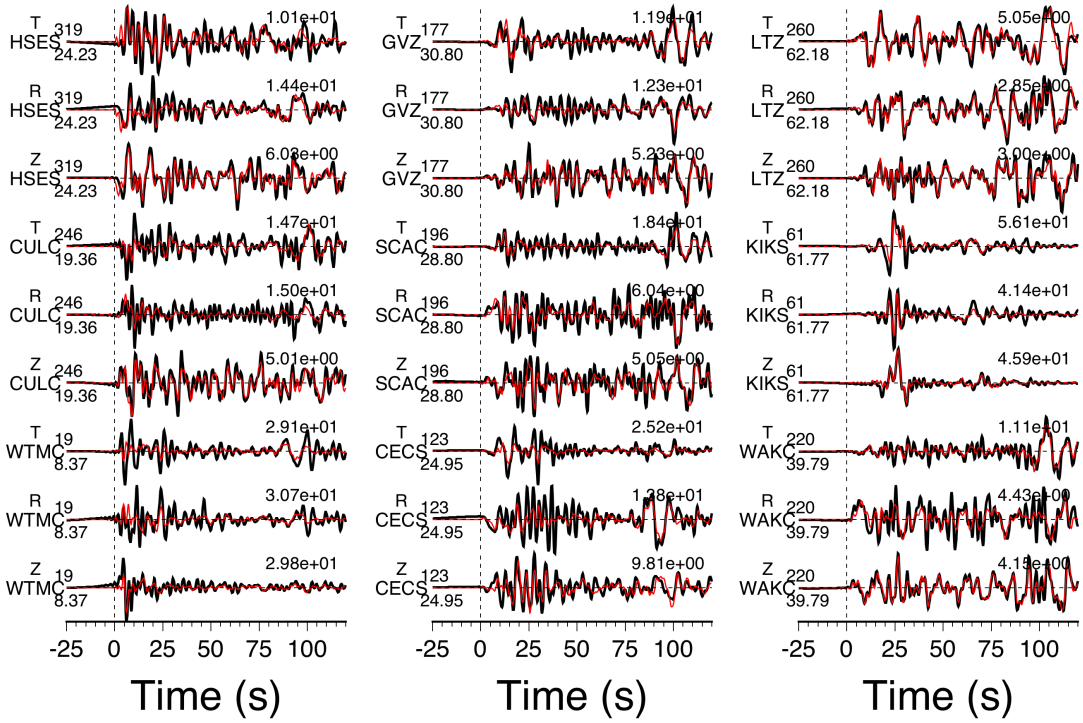
T HSES 319 24.23 1.01e+01
R HSES 319 24.23 1.44e+01
Z HSES 319 24.23 6.03e+00
T CULC 246 19.36 1.47e+01
R CULC 246 19.36 1.50e+01
Z CULC 246 19.36 5.01e+00
T WTMC 19 8.37 2.91e+01
R WTMC 19 8.37 3.07e+01
Z WTMC 19 8.37 2.98e+01
T GVZ 177 30.80 1.19e+01
R GVZ 177 30.80 1.23e+01
Z GVZ 177 30.80 5.23e+00
T SCAC 196 28.80 1.84e+01
R SCAC 196 28.80 6.04e+00
Z SCAC 196 28.80 5.05e+00
T CECS 123 24.95 2.52e+01
R CECS 123 24.95 1.28e+01
Z CECS 123 24.95 9.81e+00
T LTZ 260 62.18 5.05e+00
R LTZ 260 62.18 2.85e+00
Z LTZ 260 62.18 3.00e+00
T KIKS 61 61.77 5.61e+01
R KIKS 61 61.77 4.14e+01
Z KIKS 61 61.77 4.59e+01
T WAKC 220 39.79 1.11e+01
R WAKC 220 39.79 4.43e+00
Z WAKC 220 39.79 4.19e+00
-25 0 25 50 75 100
Time (s)
Time (s)
Time (s)

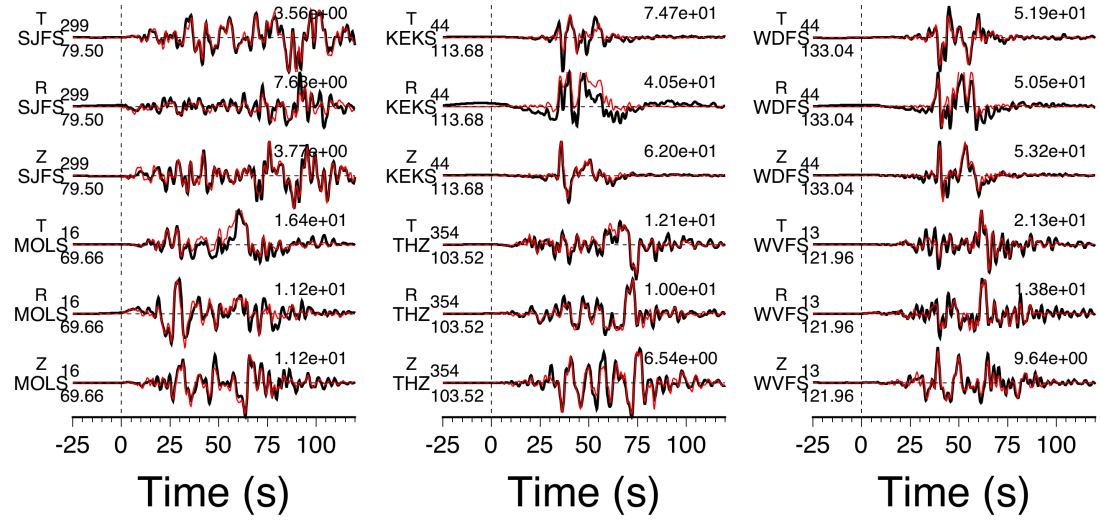
T SJFS 299 79.50 3.56e+00
R SJFS 299 79.50 7.68e+00
Z SJFS 299 79.50 3.77e+00
T MOLS 16 69.66 1.64e+01
R MOLS 16 69.66 1.12e+01
Z MOLS 16 69.66 1.12e+01
T KEKS 44 113.68 7.47e+01
R KEKS 44 113.68 4.05e+01
Z KEKS 44 113.68 6.20e+01
T THZ 354 103.52 1.21e+01
R THZ 354 103.52 1.00e+01
Z THZ 354 103.52 6.54e+00
T WDFS 44 133.04 5.19e+01
R WDFS 44 133.04 5.05e+01
Z WDFS 44 133.04 5.32e+01
T WVFS 13 121.96 2.13e+01
R WVFS 13 121.96 1.38e+01
Z WVFS 13 121.96 9.64e+00
-25 0 25 50 75 100
Time (s)
Time (s)
Time (s)

(b)

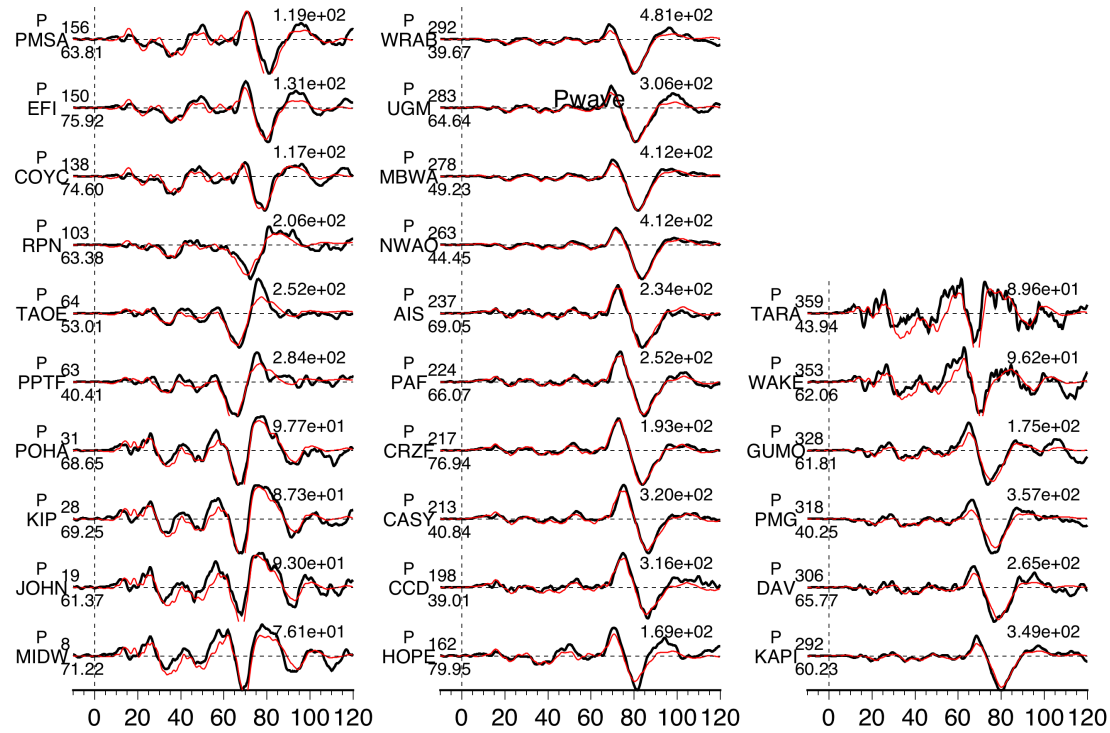
P PMSA 156 63.81 1.19e+02
P EFI 150 75.92 1.31e+02
P COYC 138 74.60 1.17e+02
P RPN 103 63.38 2.06e+02
P TAOE 64 53.01 2.52e+02
P PPTF 63 40.41 2.84e+02
P POHA 31 68.65 9.77e+01
P KIP 28 69.25 8.73e+01
P JOHN 19 61.37 9.30e+01
P MIDW 8 71.22 7.61e+01
P WRAB 292 39.67 4.81e+02
P UGM 283 64.64 3.06e+02
Pwave
P MBWA 278 49.23 4.12e+02
P NWAO 263 44.45 4.12e+02
P AIS 237 69.05 2.34e+02
P PAF 224 66.07 2.52e+02
P CRZF 217 76.94 1.93e+02
P CASY 213 40.84 3.20e+02
P CCD 198 39.01 3.16e+02
P HOPE 162 79.95 1.69e+02
P TARA 359 43.94 8.96e+01
P WAKE 353 62.06 9.62e+01
P GUMO 328 61.81 1.75e+02
P PMG 318 40.25 3.57e+02
P DAV 306 65.77 2.65e+02
P KAPI 292 60.23 3.49e+02
0 20 40 60 80 100 120

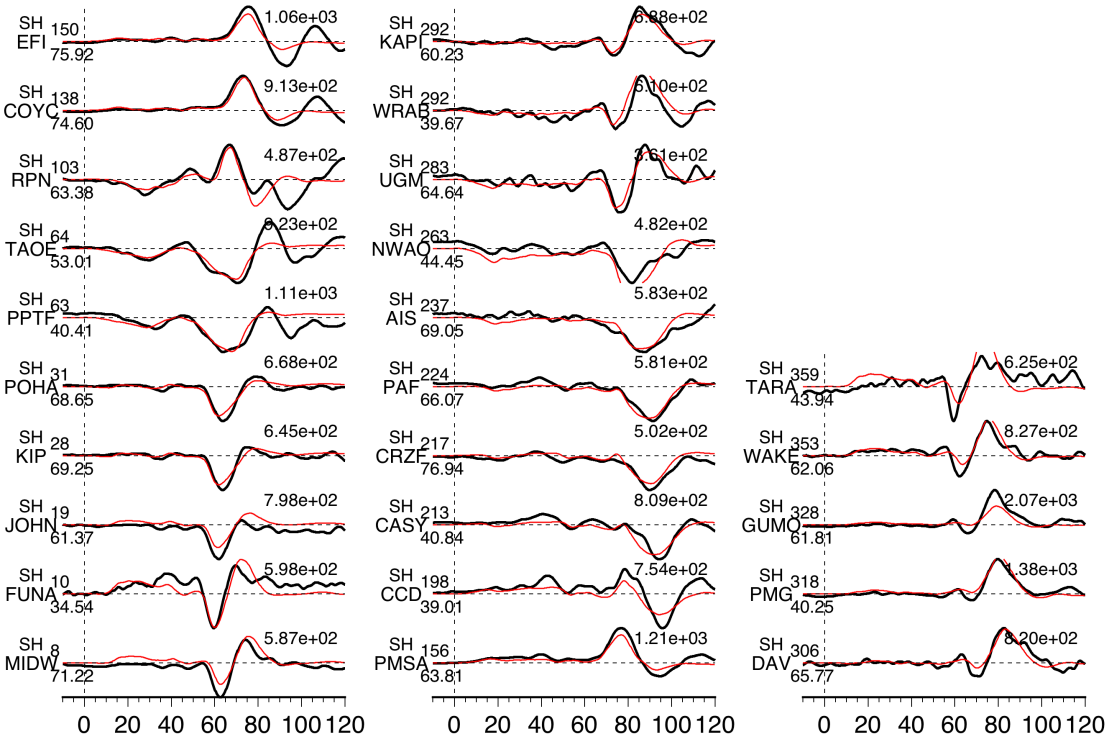
SH EFI 150 75.92 1.06e+03
SH COYC 138 74.60 9.13e+02
SH RPN 103 63.38 4.87e+02
SH TAOE 64 53.01 9.23e+02
SH PPTF 63 40.41 1.11e+03
SH POHA 31 68.65 6.68e+02
SH KIP 28 69.25 6.45e+02
SH JOHN 19 61.37 7.98e+02
SH FUNA 10 34.54 5.98e+02
SH MIDW 8 71.22 5.87e+02
SH KAPI 292 60.23 6.88e+02
SH WRAB 292 39.67 6.10e+02
SH UGM 283 64.64 8.61e+02
SH NWAO 263 44.45 4.82e+02
SH AIS 237 69.05 5.83e+02
SH PAF 224 66.07 5.81e+02
SH CRZF 217 76.94 5.02e+02
SH CASY 213 40.84 8.09e+02
SH CCD 198 39.01 7.54e+02
SH PMSA 156 63.81 1.21e+03
SH TARA 359 43.94 6.25e+02
SH WAKE 353 62.06 8.27e+02
SH GUMO 328 61.81 2.07e+03
SH PMG 318 40.25 1.38e+03
SH DAV 306 65.77 8.20e+02
0 20 40 60 80 100 120

(c)

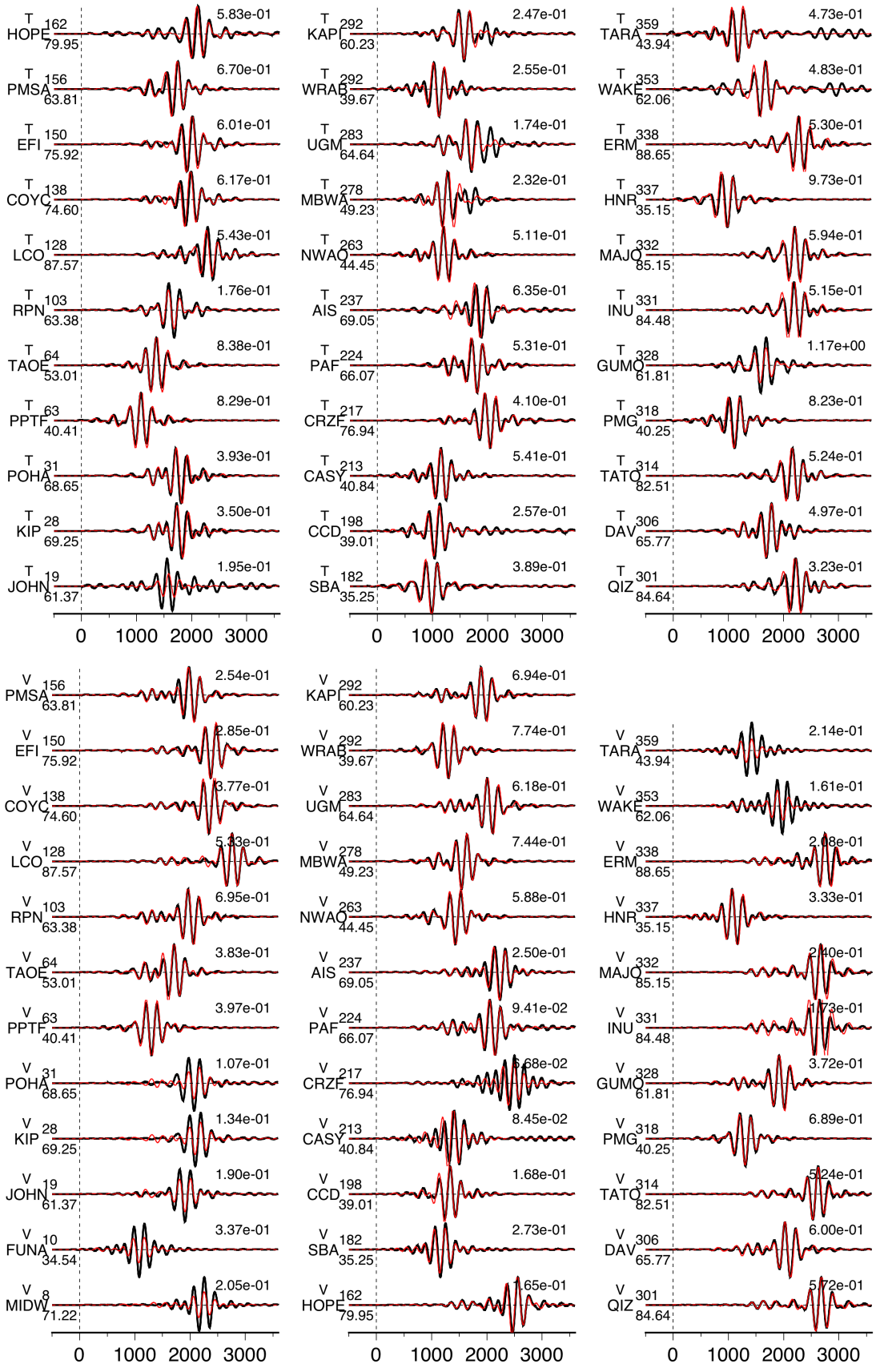
T HOPE 162 79.95 5.83e-01
T PMSA 156 63.81 6.70e-01
T EFI 150 75.92 6.01e-01
T COYC 138 74.60 6.17e-01
T LCO 128 87.57 5.43e-01
T RPN 103 63.38 1.76e-01
T TAOE 64 53.01 8.38e-01
T PPTF 63 40.41 8.29e-01
T POHA 31 68.65 3.93e-01
T KIP 28 69.25 3.50e-01
T JOHN 19 61.37 1.95e-01
T KAPI 292 60.23 2.47e-01
T WRAB 292 39.67 2.55e-01
T UGM 283 64.64 1.74e-01
T MBWA 278 49.23 2.32e-01
T NWAO 263 44.45 5.11e-01
T AIS 237 69.05 6.35e-01
T PAF 224 66.07 5.31e-01
T CRZF 217 76.94 4.10e-01
T CASY 213 40.84 5.41e-01
T CCD 198 39.01 2.57e-01
T SBA 182 35.25 3.89e-01
T TARA 359 43.94 4.73e-01
T WAKE 353 62.06 4.83e-01
T ERM 338 88.65 5.30e-01
T HNR 337 35.15 9.73e-01
T MAJO 332 85.15 5.94e-01
T INU 331 84.48 5.15e-01
T GUMO 328 61.81 1.17e+00
T PMG 318 40.25 8.23e-01
T TATO 314 82.51 5.24e-01
T DAV 306 65.77 4.97e-01
T QIZ 301 84.64 3.23e-01
0 1000 2000 3000
V PMSA 156 63.81 2.54e-01
V EFI 150 75.92 2.85e-01
V COYC 138 74.60 3.77e-01
V LCO 128 87.57 5.33e-01
V RPN 103 63.38 6.95e-01
V TAOE 64 53.01 3.83e-01
V PPTF 63 40.41 3.97e-01
V POHA 31 68.65 1.07e-01
V KIP 28 69.25 1.34e-01
V JOHN 19 61.37 1.90e-01
V FUNA 10 34.54 3.37e-01
V MIDW 8 71.22 2.05e-01
V KAPI 292 60.23 6.94e-01
V WRAB 292 39.67 7.74e-01
V UGM 283 64.64 6.18e-01
V MBWA 278 49.23 7.44e-01
V NWAO 263 44.45 5.88e-01
V AIS 237 69.05 2.50e-01
V PAF 224 66.07 9.41e-02
V CRZF 217 76.94 6.68e-02
V CASY 213 40.84 8.45e-02
V CCD 198 39.01 1.68e-01
V SBA 182 35.25 2.73e-01
V HOPE 162 79.95 1.65e-01
V TARA 359 43.94 2.14e-01
V WAKE 353 62.06 1.61e-01
V ERM 338 88.65 2.08e-01
V HNR 337 35.15 3.33e-01
V MAJO 332 85.15 2.40e-01
V INU 331 84.48 1.73e-01
V GUMO 328 61.81 3.72e-01
V PMG 318 40.25 6.89e-01
V TATO 314 82.51 5.24e-01
V DAV 306 65.77 6.00e-01
V QIZ 301 84.64 5.72e-01
0 1000 2000 3000

Figure 16: (a) Comparison of 16 three-component velocity strong motion waveforms (black lines) and synthetic seismograms (red lines) resulting from the joint inversion of strong motion and GPS data. (b) Comparison of 51 P and SH broadband waveforms; and (c) comparison of the transverse and vertical components of 65 long period whole waveforms at teleseismic stations. The station names are indicated to the left of the traces, along with the epicenter distances and azimuthal angle in degrees. At the end of the trace, the peak amplitude (cm/s for strong motion, μm for teleseismic body waves, and mm for long period whole waveforms) of the observation is given.

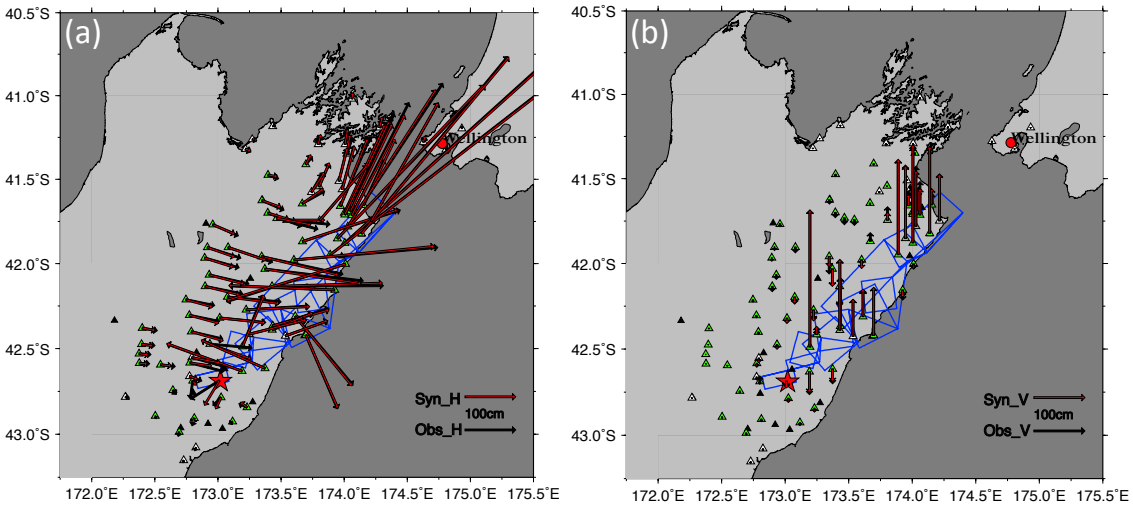

Figure 17: Observed and modeled displacements at continuous and campaign GPS stations resulting from the joint inversion of strong motion and geodetic data. (a) Observed horizontal component (black arrow) compared with synthetic displacement (red arrow); (b) vertical component.

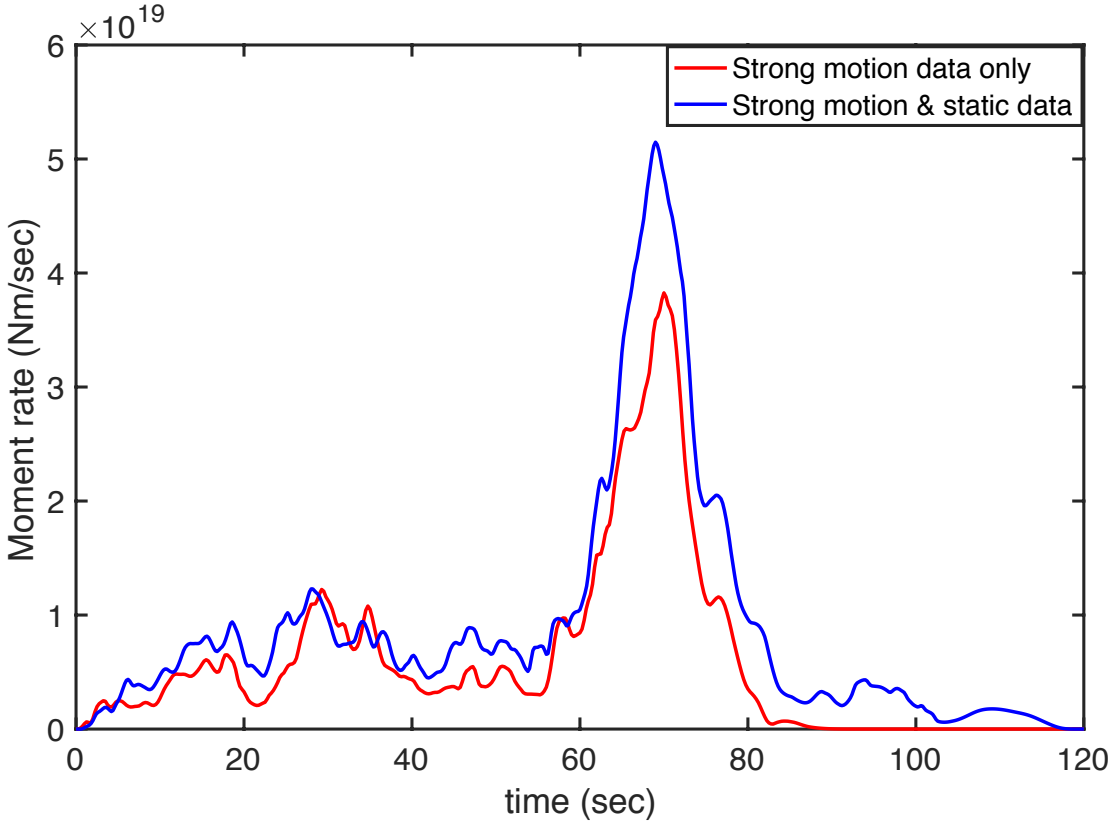

Figure 18: Comparison of the cumulative moment rate function (Nm/sec) for FF1 in red, the inversion done with strong motion data only, and for FF2 in blue, the joint inversion.

(a)

	Mo (Nm)	Average slip (m)	Average slip rate (m/s)	Average rise time (s)
1	1.00E+19	2.194	0.629	4.662
2	3.49E+19	3.978	1.585	3.402
3	3.72E+19	3.168	0.798	4.525
4	6.04E+19	3.176	1.178	3.619
5	5.02E+19	2.921	0.728	4.941
6	1.35E+20	5.458	1.414	4.823
7	7.24E+19	5.431	1.448	4.531
8	8.16E+19	5.780	1.183	5.383
9	7.28E+19	3.541	1.022	5.038
10	1.51E+20	3.768	1.256	4.067

(b)

	Mo (Nm)	Average slip (m)	Average slip rate (m/s)	Average rise time (s)
1	5.60E+18	1.250	0.401	5.142
2	7.69E+19	4.853	1.163	4.986
3	2.84E+19	3.060	0.794	4.414
4	7.97E+19	3.835	1.118	4.021
5	3.28E+19	1.914	0.828	2.926
6	2.31E+20	4.993	1.622	4.767
7	1.15E+20	7.760	1.408	5.976
8	2.50E+20	7.435	1.851	4.944
9	1.48E+20	8.734	1.828	6.582
10	1.08E+20	5.418	1.291	4.980

Table 4: Seismic moment (Nm), average slip (m), average slip rate (m/s) and average rise time (s) calculated according to formula (1) – (4) for (a) FF1 and (b) FF2.